DEVELOPMENT OF GENERAL UNSTRUCTURED RESERVOIR UTILITY AND FRACTURED RESERVOIR MODELING

A Dissertation

by

BICHENG YAN

Submitted to the Office of Graduate and Professional Studies of
Texas A&M University
in partial fulfillment of the requirements for the degree of

DOCTOR OF PHILOSOPHY

Chair of Committee,	John E. Killough
Committee Members,	Maria A. Barrufet
	I. Yucel Akkutlu
	Hadi Nasrabadi
Head of Department,	Dan Hill

May 2017

Major Subject: Petroleum Engineering

ABSTRACT

New complexities have been identified in fractured shale reservoirs, such as multi-porosity types and non-Darcian transport and storage mechanisms in the shale nano-pores. Reservoir simulation serves as a convenient approach for reservoir management. However, commercial reservoir simulators remain as black boxes for reservoir engineers. Currently none of these simulators offer a full-featured tool to solve those problems.

In this work, a general Multi-Porosity Model is developed to handle the reservoir heterogeneity in the fractured reservoirs. This model allows the simulation of any number of porosity systems, and thus it resolves the limited number of porosity types in the Dual-Porosity Models. Moreover, this model allows arbitrary inter-porosity and intra-porosity connections, so it breaks the limitation of fixed connections in the Dual-Porosity Models. In addition, a novel porosity subdivision algorithm has been designed, and a new shape factor is correspondingly derived to consider the porosity subdivision. Therefore, the transient flow can be accurately approximated by the high resolution from the subdivision. Finally, the Multi-Porosity Model is implemented as a standalone unstructured tool, and thus it is able to be flexibly interfaced with unstructured reservoir simulators. This approach is successfully applied to model fluid transport in the fractured reservoirs and shale gas reservoirs.

The second thrust area is the development of a fully compositional simulator, **G**eneral **U**nstructured **R**eservoir **U**tility (GURU). GURU is based on Control-Volume Finite-Difference method, so it can conveniently handle different grid discretization

methods, such as Cartesian grids, discrete fracture models and Multi-Porosity Models etc. Besides, a novel class of compositional space preconditioned VLE methods has been proposed for efficient compositional simulation, and it speeds up the flash calculation by a more reliable initial estimate. In addition, mechanisms are flexibly considered in GURU. Darcy flow is the basic flow mechanism, and multi-component adsorption is optionally considered for fluid storage. Gas slippage and Knudsen diffusion are also incorporated for the shale gas transport. Furthermore, a unique shale reservoir modeling workflow is established for mechanistic investigation. Heterogeneity of the fractures is upscaled by sector models, and multi-porosity types are honored by the Triple-Porosity Model, and fluid storage and transport physics are implemented in GURU.

DEDICATION

To my family

ACKNOWLEDGEMENTS

The process to accomplish this work was a long journey to go beyond myself, and it would not have been possible without the help in one way or another from many people. I would like to thank all of them with my great appreciation.

My deepest gratitude goes to my advisor, Dr. John Killough, for his sincerity, inspiration and encouragement. I have been the most fortunate to be his student. During my five years at Texas A&M University, Dr. Killough selflessly guided me not only on my research but also on many other aspects of life, which will be greatly beneficial for my whole life.

I also thank Dr. Maria Barrufet, for her valuable suggestions at different stages of my research. I would also thank her for being my committee member.

I am very grateful to Dr. Yucel Akkutlu, for being my committee member, and he also provided me with valuable comments about fluid transport in shale.

I am very thankful to Dr. Hadi Nasrabadi, for his great help on compositional simulation, and for being my committee member.

I also would like to thank Dr. Ernesto Valbuena Olivares from Chevron for sharing his simulator and valuable discussions, which are greatly helpful to open my mind about reservoir simulation.

My sincere thanks also goes to my friends Dr. Yuhe Wang, Masoud Alfi, Zhi Chai, Cheng An, Lidong Mi, Yang Cao and Hewei Tang for our great cooperation, and I also thank other group members for their help during my graduate study.

I acknowledge Crisman Institute for the financial support to this research work. I would like to thank all those friends, professors and staff in the Department of Petroleum Engineering at Texas A&M University for the enjoyable time and help.

I would like to thank my colleagues from ConocoPhillips for their help during my internships, especially Drs. Torres Jose, Shiralkar Gautam, Monteagudo Jorge, Hector Klie and Yong Zhao.

Finally, I would like to thank my father Zaiqiang, my mother Chunhui, my grandma Zhongyu, and my wife Limin for their endless love and support.

NOMENCLATURE

Acronyms

BHP	Bottom Hole Pressure
CRS	Compressed Row Storage
CSIG	Compositional Space based Initial Guess
DFM	Discrete Fracture Model
DFN	Discrete Fracture Network Model
DP	Dual-Porosity Model
DPSP	Dual-Porosity Single-Permeability Model
EDFN	Enhanced Discrete Fracture Network Model
EOS	Equation of State
FIM	Fully Implicit Method
FS	Fracture System
FX	x-axis oriented fractures
FY	y-axis oriented fractures
GURU	General Unstructured Reservoir Utility
HF	Hydraulic Fractures
IM	Inorganic Matrix
IMPES	IMplicit Pressure Explicit Saturation
IMPEM	IMplicit Pressure Explicit Mass
LGR	Local Grid Refinement

NC	Neighbor Connection
NF	Natural Fractures
NNC	Non-Neighbor Connection
NR	Newton Raphson method
MCRS	Modified Compressed Row Storage
MINC	Multiple INteracting Continua
MPM	Multi-Porosity Model
OGIP	Original Gas In Place
OM	Organic Matrix
PIC	Pseudo Idle Component
PKC	Pseudo Key Component
PR-EOS	Peng-Robinson Equation of State
QPQK	Quad-Porosity Quad-Permeability Model
RR	Rachford-Rice Equation
RRP	Rachford-Rice Equation Preconditioning
SRV	Stimulated Reservoir Volume
SSI	Successive Substitution Iteration method
TPDK	Triple-Porosity Dual-Permeability Model
TPSP	Triple-Porosity Single-Permeability Model
TPTP	Triple-Porosity Triple-Permeability Model
VLE	Vapor Liquid Equilibrium
WCIG	Wilson’s Correlation based Initial Guess

Greeks

β	Coefficient in shape factor formulation, dimensionless
η	Gas apparent permeability multiplier, dimensionless
ξ_α	Viscosity parameter of phase α
ξ_i	Viscosity parameter for component i
ϵ	Perturbation
ε	Tolerance
ω_i	Acentric factor of component i
$\mathcal{S}_i$	Component shift factor of component i for volume translation
κ_{ij}	Binary interaction coefficient between component i and j
Δt	Time step size, $days$
Δx	Grid size in x direction, ft
Δy	Grid size in y direction, ft
Δz	Grid size in z direction, ft
ϕ	Porosity, fraction
Φ	Potential, $psia$
Φ_α	Phase potential, $psia$
φ_i^α	Fugacity coefficient of component i in phase α
λ_α	Mobility of phase α, cP^{-1}
$\lambda_{\alpha,p}$	Mobility of phase α for well perforation p, cP^{-1}
λ_i	Mean free path for component i, μm
μ	Fluid viscosity, cP

μ_α	Viscosity of phase α, cP
μ_α^*	Phase viscosity at atmospheric pressure, cP
μ_{mf}	Average fluid viscosity between matrix and fracture, cP
ρ	Fluid mass density, lb/ft^3
ρ_α	Fluid mass density of phase α, lb/ft^3
$\rho_{\alpha,s}$	Average mass density phase α in connection s
ρ_{mf}	Average fluid density between matrix and fracture, lb/ft^3
ρ_s	Rock bulk mass density, lb/ft^3
$\tilde{\rho}_\alpha$	Molar density of phase α, $lbmol/ft^3$
$\tilde{\rho}_\alpha^{sc}$	Molar density of phase α at standard condition, $lbmol/ft^3$
$\tilde{\rho}_{r_\alpha}$	Reduced phase molar density for phase α, $lbmol/ft^3$
$\tilde{\rho}_{pc_\alpha}$	Pseudocritical phase molar density, $lbmol/ft^3$
σ	Shape factor, ft^{-2}
σ_{mfi}	Shape factor between fracture and matrix sub-blocks in i direction ($i = x, y, z$), ft^{-2}
$\tau_{\alpha(j,i)}$	Mass transfer rate of phase α between j^{th} and i^{th} porosity, lb/day
τ_{mf}	Transfer flow rate between matrix and fracture, lb/day
τ_{mfi}	τ_{mf} in $i = x, y, z$ direction, lb/day

Subscripts and superscripts

α	Phase index, including oil (o), gas (g), and water (w)
avg	Average
f	Fracture
i	Fluid component index in compositional space
j	Cell index or porosity index in material balance equation
l	Liquid phase
n	Previous timestep or iteration
$n+1$	Current timestep or iteration
$nwet$	Non-wetting phase
m	Matrix
p	Perforation index
ref	Reference pressure condition
res	Reservoir
s	Connection or connected cell surface index
sc	Surface condition
$shift$	Volume shift
T	Matrix transpose operation
v	Vapor phase
$well$	Well
wet	Wetting phase

Variables

a	PR-EOS mixture parameter
a_i	PR-EOS parameter for component i
A	PR-EOS coefficient
A_j	Contact area for the surface of connection s or matrix block and fracture in x, y, z directions, ft^2
b	PR-EOS mixture parameter
b_i	PR-EOS parameter for component i
B	PR-EOS coefficient
B_w	Water formation volume factor, RB/STB
c	Overall correction factor for volume translation
c_α	Phase correction factor for volume translation
c_i	Volume translation correction factor for component i
C_{μ_w}	Water viscosibility, $psia^{-1}$
C_r	Rock compressibility, $psia^{-1}$
C_w	Water compressibility, $psia^{-1}$
d_f	Half of fracture aperture, ft
d_i	Distance between matrix block and fracture surface, ft
$d_{m,j}$	Collison diameter of component j, μm
D	Depth of grid, ft
f_i	Number of surfaces of matrix sub-block connected to fracture in i direction ($i = x, y, z$), dimensionless

f_l	Liquid mole fraction, fraction
f_l^{sc}	Liquid mole fraction at surface condition, fraction
f_v	Vapor mole fraction, fraction
f_v^{sc}	Vapor mole fraction at surface condition, fraction
$\hat{f}_i^{\alpha}$	Fugacity of component i in phase α
g_c	Gravity constant
g_j	Function defining compositional spaces, $j = 1, 2, 3, 4$
J	Jacobian matrix for Newton-Raphson Method
k	Rock permeability, mD
k_{app}	Matrix apparent permeability, mD
k_0	Rock intrinsic permeability, mD
k_{ij}	Average permeability between i^{th} porosity and j^{th} porosity, mD
k_m	Matrix permeability, mD
k_{mf}	Average permeability between matrix and fracture, mD
$k_{r\alpha}$	Relative permeability, dimensionless
k_{rocw}	Oil relative permeability at connate water saturation
k_{rog}	Oil relative permeability at connate water and actual gas saturation
k_{row}	Oil relative permeability at actual water saturation
k_x	Rock permeability in x direction, mD
k_y	Rock permeability in y direction, mD

k_z	Rock permeability in z direction, mD
K_i	Equilibrium ratio of component i, dimensionless
$K_{n,i}$	Knudsen number of component i, dimensionless
L	Size of cubic matrix block, ft
L_i	Size of matrix block or sub-block in $i = x, y, z$ direction, ft
L_j	Nodal distance from grid block center to interface, ft^2
$nCells$	Total number of active cells in a reservoir model
n_h	Total number of component in oil and gas phases
N	Number of orthogonal fracture sets, $N = 1, 2, 3$
N_A	Avogadro's constant, $6.022 \times 10^{26}\ kmol^{-1}$
N_i	Moles of component i stored in compressed state in unit cell volume, $lbmol/ft^3$
N_w	Moles of water in unit cell volume, $lbmol/ft^3$
$nWells$	Total number of wells in a reservoir model
M_i	Moles of component i stored by gas adsorption in unit cell volume, $lbmol/ft^3$
MW_i	Molecular weight of component i, $lb/lbmol$
MW_α	Molecular weight of phase α, $lb/lbmol$
p	Pressure, $psia$
p_α	Pressure of phase α, $psia$
p_b	Bubble point pressure, $psia$
p_c	Capillary pressure between nonwetting and wetting phases, $psia$

p_{ci}	Critical pressure of component i, $psia$
p_p	Pressure at well perforation p, $psia$
p_{ri}	Reduced pressure of component i
p_{wf}	Bottom-hole pressure, $psia$
p_{wf}^*	Bottom-hole pressure specified by user, $pisa$
$p_{L,i}$	Langmuir pressure of component i, $psia$
PV_j	Pore volume in cell j, ft^3
Q	Well production or injection mass rate, lb/day
$\tilde{Q}_\alpha$	Phase molar rate for well, $lbmol/day$
q_α^p	Molar rate of phase α in perforation p, $lbmol/day$
$Q_{V,\alpha}^*$	Phase volume rate at surface condition for phase α, STB/day or $MSCF/day$
r	Pore radii, μm
r_o	Effective wellbore radius, ft
r_w	Wellbore radius, ft
R	Gas constant, 10.7316 $ft^3 psia/R/lbmol$
$\vec{R}$	Residual vector
$R_{f,i}$	Fugacity equilibrium residual for component i
$R_{i,j}$	Mass balance residual of hydrocarbon component i in cell j
R_r	Rachford-Rice Equation residual
$R_{w,j}$	Mass balance residual of water component in cell j

$R_{vol,j}$	Volume balance in cell j
$R_{w,j}$	Mass balance residual of water in cell j
$\vec{R}_{res}$	Reservoir residual
$\vec{R}_{well}$	Well residual
S_α	Saturation of phase α, volume fraction
S	Well skin, dimensionless
t	Time, days
T	Temperature, °F
T_{ci}	Critical temperature of component i, °F
$T_{F,F}$	Intra-porosity transmissibility submatrix in fracture porosity
$T_{F,I}$	Inter-porosity transmissibility submatrix between fracture and inorganic porosity
$T_{F,O}$	Inter-porosity transmissibility submatrix between fracture and organic porosity
$T_{I,I}$	Intra-porosity transmissibility submatrix within inorganic porosity
$T_{I,O}$	Inter-porosity transmissibility submatrix between inorganic and organic porosity
$T_{O,O}$	Intra-porosity transmissibility submatrix within organic porosity
T_s	Transmissibility between two connected cells, $mD \cdot ft$
T_{ri}	Reduced temperature of component i, dimensionless
υ_α	Molar volume of phase α, $ft^3/lbmol$

υ_{c_i}	Critical molar volume of component i, $ft^3/lbmol$
V_j	Grid volume of cell j, ft^3
$V_{\alpha,j}$	Fluid volume of phase α in grid j, ft^3
$V_{L,i}$	Langmuir volume of component i, scf/lb
V_m	Volume of matrix block, ft^3
WI_p	Well geometric index of perforation p, $mD \cdot ft$
x_i	Liquid phase mole fraction of component i , fraction
x_i^α	Mole fraction of component i in phase α, fraction
$\vec{X}$	Primary variable vector
y_i	Vapor phase mole fraction of component i , fraction
z_i	Bulk fluid composition, fraction
Z	Compressibility factor, dimensionless

TABLE OF CONTENTS

Page

LIST OF FIGURES

Page

LIST OF TABLES

Page

CHAPTER I

INTRODUCTION

1.1 Background

1.1.1 Fractured Reservoir Modeling

There are many hydrocarbon resources stored in fractured reservoirs, including carbonate reservoirs, coal bed methane and shale gas/oil reservoirs. Such reservoirs are usually partitioned into two different flow units, including matrix and fracture, because there is significant difference in fluid storage and flow conductivity between the two units. Several approaches have been proposed to simulate fluid flow in fractured reservoirs. They are basically categorized into three types, Discrete Fracture Model (DFM), Dual-Porosity Model, and their combinations. DFM, based on unstructured grid discretization, can explicitly describe the effect of fracture geometric details (Mi et al. 2014; Sun et al. 2012; Sun et al. 2014a; Sun and Schechter 2014b; Yu et al. 2011; Yu et al. 2016), and can naturally capture the complex flow phenomena occurring in the vicinities of those sparse fractures. However, such simulators are still not practical for field-scale studies, since unstructured gridding becomes challenging and computationally expensive when a large number of fractures in a complex distribution is present (Li et al. 2015). To overcome these deficiencies, a simplified model for Discrete Fracture Network (DFN) Modeling was developed. This model can decrease the number of grid blocks (Mi, L. et al. 2016) and computational time (Basquet et al. 2005; Sarda et al. 2001), while it still conserves the advantages of the DFM.

On the other hand, the Dual-Porosity Model is the most commonly used fractured reservoir modeling approach, and it was originally proposed by Barenblatt and Zheltov (1960) and introduced to petroleum industry by Warren and Root (1962), as shown in **Fig. 1.1**. This approach assumes that fracture is a continuous flow system with low pore volume. The matrix with low permeability provides the main fluid storage space and transfers fluid to fracture system as sources. This approach is appropriate and efficient for the modeling of reservoirs with densely distributed fracture networks. However, a Dual-Porosity Model can only simulate two continua, which makes it insufficient to model fractured reservoirs with more than two porosity systems. Multi-Porosity Models are developed to simulate reservoirs with more than two porosity systems. Extended from Dual-Porosity Model, Hinkley et al. (2013) presented a Multi-Porosity simulation model and applied it in unconventional reservoir modeling, but it is still based on traditional transfer functions and local grid refinement (LGR) to capture the transient flow effect. Jiang and Younis (2015) coupled MINC (Pruess 1982) with unstructured DFN (Karimi-Fard et al. 2004) or EDFM (Moinfar et al. 2013) to honor transient flow in the matrix and to model the fracture sparsity. In this model the intrinsic characteristics of MINC allow only serial flow mode in the sequence of organics-inorganics-fracture. More recently, EDFM has been coupled with a Multi-Porosity Model such that different porosity systems and hydraulic fracture sparsity can be characterized (Chai et al. 2016a, 2016b). It works as a grid preprocessor for simulation, and leverages the advantages of EDFM and the Multi-Porosity Model such that it is flexible to describe different porosity systems and fracture geometries.

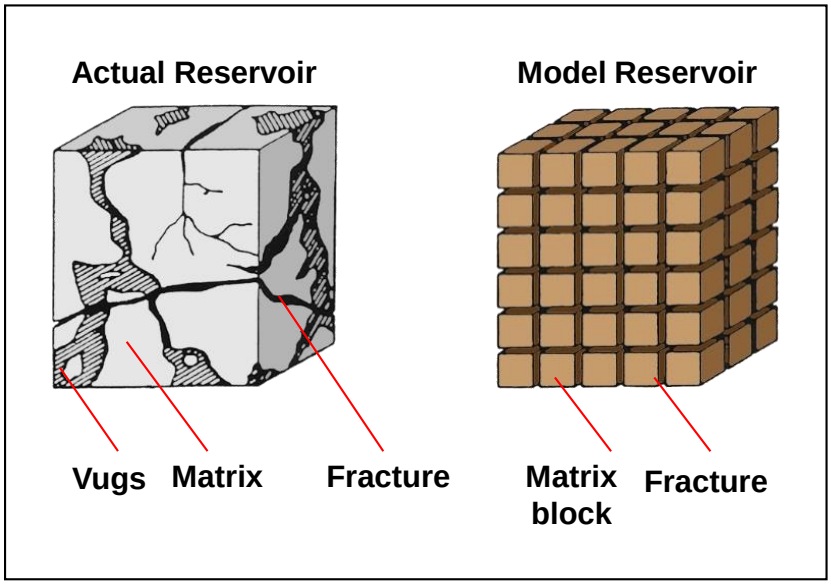

Fig. 1.1—Dual-Porosity Model

1.1.2 Shale Reservoir Features

Shale reservoirs belong to fractured reservoirs, and one of the major problems for shale reservoir simulation is the characterization of complex porosity systems. Those porosity types are hydraulic fractures, natural fractures, inorganic matrix and organic matrix (Wang and Reed 2009). Among them, the whole fracture network covering multiple scales provides the pathway to produce fluid from tight matrix. The matrix is partitioned into inorganic and organic matrix with different attributes, such as wettability (Odusina et al. 2011) and pore structure (Passey et al. 2010). Therefore, a reservoir characterization approach becomes powerful, if it can honor those different porosity types and conserve the geometric details of the fracture system in an economical way.

Another issue related to shale reservoirs is the characterization of fluid transport and storage mechanisms and fluid properties. In the shale matrix, the pore size is in nano-scale and the permeability is in nano-Darcy magnitude. In this scenario the interaction between hydrocarbon molecules and the pore-wall becomes significant and fluid adsorption/desorption is considered to be remarkable as well. Thus, many investigators consider that Darcian flow is quite limited or even breaks down here. Different non-Darcy gas flow models have been proposed to consider the coupling effect of slippage flow, viscous flow and Knudsen diffusion (Civan 2010; Fathi and Akkutlu 2012; Javadpour 2009). In liquid-rich shale, multi-component Fickian diffusion and multi-component adsorption/desorption is necessary to be considered (Cao et al. 2015), since Darcy flow in tight shale matrix is extremely weak there. Besides, the impact of capillary pressure on the vapor-liquid equilibrium (VLE) in matrix nano-pores is also remarkable. Wang et al. (2013f) showed that for oil-wet reservoirs the confinement effect favors single-phase oil flow by suppressing bubble point pressure.

1.2 Study Scopes

The purpose of this study is to investigate both reservoir heterogeneity and fluid physics in reservoir simulation. Therefore, the scope of this study covers two aspects related to reservoir simulation, including, (1) general Multi-Porosity Model for fractured reservoir modeling; (2) general unstructured reservoir simulator development.

A generalized Multi-Porosity Model for fractured reservoir characterization is proposed based on the extension of Dual-Porosity Model. The newly developed model

flexibly honors any number of porosity types in complex fractured reservoirs. As a continuous approach, it can consider different properties in different porous media, including permeability, porosity and wettability etc., and thus remarkable improvements over conventional Dual-Porosity Model are achieved. Besides, the approach is generalized to include Multi-Porosity and Multi-Permeability formulations, because it allows arbitrary connectivity for intra-porosity flow and inter-porosity flow. Moreover, a porosity subdivision function and corresponding new transfer function is developed to honor transient flow for inter-porosity fluid transport. The generalized Multi-Porosity Model can be a grid discretization tool and thus be coupled with flow reservoir simulation.

On the other hand, an unstructured compositional reservoir simulator is developed as a flow solver. The simulator is called **G**eneral **U**nstructured **R**eservoir **U**tility (GURU). The new simulator GURU is an unstructured reservoir simulator with a flexible and user-extensible architecture. GURU is based on Control-Volume Finite-Volume method. The simulator solves reservoir equations using a fully implicit approach for three-phase flow (oil, gas, and water), and hydrocarbon properties are calculated by vapor-liquid equilibrium based on cubic equation of state (EOS). Basically GURU is allowed to simulate conventional compositional flow problems. Besides, the design of GURU makes it naturally compatible with different grid discretization, including structured grids, Dual/Multi-Porosity Models, and unstructured grids. Since different fluid transport mechanisms are likely to occur in different porosity types in shale reservoirs, GURU is designed as a general framework to systematically incorporate multiple mechanisms, such as Darcy flow, slippage flow, and multi-component adsorption/desorption. The developed

simulator becomes a tool for seamlessly modeling multiple scale levels from the pore-level to large-scale fractures and finally to the well and field levels. Ultimately, GURU allows us to better understand the static and dynamic complexities in shale reservoirs and, in turn, serves reservoir engineers as a useful tool to better predict ultimate recovery from shale reservoirs.

1.3 Development Milestones

11 research tasks are defined in this section and they are performed to accomplish those above goals in this study.

1. Formulate and validate transfer function derivation for Multi-Porosity Model with porosity subdivision.
2. Develop a standalone package of Multi-Porosity Model with or without porosity subdivision based on the extension of Dual-Porosity Model.
3. Validate the Multi-Porosity Model with cases of different level of complexities, including Dual-Porosity Models, Triple-Porosity Models and Quad-Porosity Models.
4. Develop a standalone unstructured three-phase compositional reservoir simulator based on Control-Volume Finite-Difference method and modified Young and Stephenson (1983) formulation.
5. Develop a standalone VLE calculation package based on both successive substitution iteration (SSI) method and Newton-Raphson Iteration, and implement a global compositional-space preconditioner for VLE.

6. Evaluate the performance and accuracy of the VLE package with different fluid samples and couple it with GURU.
7. Interface GURU with different linear solver libraries.
8. Validate GURU with mature commercial reservoir simulator for 3D 3-phase heterogeneous reservoir case.
9. Couple the reservoir simulator with complex unstructured grid discretization approaches and validate the simulator for multiphase fluid flow through non-orthogonally fractured reservoirs.
10. Extend GURU's functionality for modeling non-Darcy flow mechanisms in shale gas reservoirs, including multi-component adsorption/desorption and gas slippage and Knudsen diffusion.
11. Bridge GURU with a Multi-Porosity Model for simulating multi-continuum multi-physics in shale gas reservoirs, and evaluate the impact of fracture system, connectivity and non-Darcy flow mechanisms on shale gas production.

CHAPTER II

GENERAL MULTI-POROSITY MODEL*

Conventional Dual Porosity Model is challenged to flexibly simulate reservoirs with more than two porosity systems and it is also difficult to capture the transient fluid transfer between matrix and fracture. This chapter aims to solve those problems in complex fractured reservoir simulation.

2.1 Previous Work in Literature

In fractured reservoirs, the matrix contributes most of the fluid storage but very little on fluid transport; on the contrary, the fracture system provides high flow capacity but low pore volume. The concept of Dual-Porosity Model was derived by Barenblatt and Zheltov (1960) and introduced to petroleum industry by Warren and Root (1962) to study the flow behavior in fractured reservoirs. The actual fracture network is homogenized and the matrix domain is idealized using sugar cube geometries. The Dual-Porosity Single-Permeability Model only permits fracture contributing to global flow, but the matrix works as sources/sinks for the fracture domain. When the matrix can also contribute global fluid transport in a reservoir, the Dual-Porosity Dual-Permeability Model was designed to allow both matrix-to-matrix and fracture-to-fracture flow (Gilman 1986; Gilman and Kazemi 1988). To characterize the transient flow in individual matrix blocks, the method of

"Multiple INteracting Continua" (MINC) was proposed by Pruess (1985) to discretize the matrix into a couple of nested volumes to resolve the dynamics in the matrix block. For gravity segregation in individual matrix blocks, a "Subdomain" method was used to vertically discretize matrix block into vertically stacked sub-blocks to allow gravity drainage between them (Fung 1991; Gilman 1986).

In the Dual-Porosity Model, the matrix is considered as discontinuous sources/sinks to feed the continuous fracture system. Assuming that Darcy's law applies for flow in matrix and fracture, mathematically Dual-Porosity Model involves mass balance equations for both matrix and fracture systems, shown as Equations (2.1) and (2.2) (taking single phase black-oil model as an example). In addition, an extra matrix-fracture transfer term, namely "transfer function", is used to evaluate the interaction between matrix and fracture, shown in Equation (2.3),

$$\nabla \cdot [\frac{\rho k_f}{\mu}(\nabla \Phi_f)] - \tau_{mf} = \frac{\partial(\phi\rho)_f}{\partial t} + Q \tag{2.1}$$

$$\tau_{mf} = \frac{\partial(\phi\rho)_m}{\partial t} \tag{2.2}$$

$$\tau_{mf} = \sigma \frac{\rho k_{mf} V_m}{\mu}(\Phi_m - \Phi_f) \tag{2.3}$$

where σ is named as shape factor, a geometric parameter considering the surface area of the matrix blocks per unit volume and a characteristic length of matrix-fracture transfer flow (Thomas et al. 1983). There exist a lot of different methods to derive the shape factor σ for Dual-Porosity Model, and it may or may not be derived based on the assumption pseudo-steady state conditions. Assuming single-phase quasi-steady-state flow, Warren

and Root (1962) derived the first formula for shape factor for a cubic matrix block of size L with N sets of orthogonal fractures, shown as Equation (2.4),

$$\sigma = \frac{4N(N+2)}{L^2} \tag{2.4}$$

After then a lot of researchers derived different shape factor formulae based on different assumptions, and basically they followed the format of Equation (2.5) but with different value of β. If permeability anisotropy is considered, the product of σ and permeability k can be evaluated together, shown as Equation (2.6),

$$\sigma = \beta\left(\frac{1}{L_x^2} + \frac{1}{L_y^2} + \frac{1}{L_z^2}\right) \tag{2.5}$$

$$\sigma k = \beta\left(\frac{k_x}{L_x^2} + \frac{k_y}{L_y^2} + \frac{k_z}{L_z^2}\right) \tag{2.6}$$

Different values of β in Equation (2.6) are summarized in **Table 2.1**. In finite difference formulation, assuming a linear potential gradient between the center of a matrix block and the fracture surface (Ueda et al. 1989), Kazemi et al. (1976) proposed the solution of shape factor, with β for Equations (2.5) and (2.6) equal to 4.0; through a pseudo-steady-state single phase flow (constant rate), Coats (1989) derived the shape factor σ through solving the diffusivity equation, with β for Equations (2.5) and (2.6) equal to 8; without assumption of pseudo-steady-state flow, Lim and Aziz (1995) presented the approximate solution of diffusivity equation with constant pressure boundary condition, and their β for Equations (2.5) and (2.6) is π^2. Besides, Lim and Aziz's shape factor value is consistent with the result of Zimmerman et al. (1993).

Considering the non-orthogonality of fracture systems, Sarma and Aziz (2006) proposed a method to calculate the shape factor for arbitrary shape of matrix block, and distinguished fluid expansion and imbibition terms in the two phase transfer function.

Table 2.1—Different β values in Equation (2.6)

Model	β in Equation (2.6)
Kazemi	4.0
Lim&Aziz or Zimmerman	π^2
Coats	8

In many fractured reservoirs, there might exist more than two porosity systems. For example, those different porosity systems are complex and different from matrix and fracture porosity types, and they can be multiple fracture sets with different geometries (hydraulic and natural fractures), multiple matrix porosity types with different wettabilities or fluid flow and storage mechanisms in shales (Wang and Reed 2009), or even free flow domains (vugs and caves in carbonate reservoirs) (He et al. 2015). The traditional Dual-Porosity Models cannot comprehensively characterize the complexities in those reservoirs. Meanwhile, when there exists an extremely high contrast of permeability and pore volume between different porosity types, fluid flow usually covers multiple time-scales in different porosity types and transient flow is very important to be considered, and people has applied local grid refinement (LGR) into Dual-Porosity Models (Rubin 2010) and still use the previous calculation approach for shape factor and transfer function (Kazemi et al. 1976). Also people used different approaches to increase

the number of simulated porosity types. Wu et al. (2014) proposed a generalized model to simulate three different porosity types in shale reservoirs: discrete-fracture for hydraulic fracture system, and continuum approach (MINC) for natural fracture system and tight matrix blocks. A discrete-matrix in Micro-Scale Model was applied to represent different matrix types in fractured shale reservoirs (Alfi et al. 2014a), and for single phase scenario the Micro-Scale Model was further upscaled to reservoir scale through a concept of matrix apparent permeability for Dual-Porosity Modeling (Yan et al. 2015). After all those approaches are still based on the design of the Dual-Porosity Model, and the number of simulated porosity systems is increased but still limited. On the other hand, HinkleyWang et al. (2013) recently extended the traditional Dual-Porosity Model and designed a Multi-Porosity Model to honor the multiple porosity types. Theoretically the method was able to simulate any number of porosity systems and different physics among them, and it shows great application potential in carbonate reservoirs and fractured shale reservoirs. Yet in this model the traditional transfer function is applied and it cannot provide a better solution to capture the transient flow in multiple porosity systems.

Based on the unique in-house black-oil reservoir simulator (details referred to (Yan et al. 2013b)), this chapter develops a general Multi-Porosity Model to simulate fractured reservoirs with more than two porosity systems. Similar to HinkleyWang et al. (2013), this model honors any number of porosity systems with different properties. In addition, the high contrast of fluid conductivity in different porosity systems results in a multi-scale fluid transfer in different porosity systems, so a hierarchical porosity subdivision discretization scheme is proposed to solve the problem. Different from conventional LGR

application in Dual-Porosity Model, a new formulation of shape factor for porosity subdivision is derived to accurately consider the impact of the transient flow on mass transfer between matrix and fracture. The new model is generalized such that users can specify arbitrary inter-porosity and intra-porosity connections, and make a convenient transformation between Multi-Porosity Model (without intra-porosity flow) and Multi-Permeability Model (with intra-porosity flow). The following section presents the derivation and numerical validation of the new shape factor for porosity subdivision, and it shows that it is more general than previous formulae.

2.2 Shape Factor Derivation and Validation

In fractured reservoirs, it is reasonable to assume that the local changes of thermodynamic conditions, such as pressure, temperature etc., in matrix blocks depend primarily on the distance from the fracture surface, and this is a basic assumption to discretize matrix blocks through "MINC" (Pruess 1985). Therefore, bounded by fractures, radial flow usually occurs in a matrix block (Yan et al. 2013a). Intrinsically this makes shape factors of Kazemi et al. (1976) not preferable to those of Coats (1989) and Lim and Aziz (1995), since Kazemi et al. (1976) assumes a linear pressure gradient within the matrix block, but the latter two are based on analytic solution of the pressure diffusivity equation with boundary constrains.

In the case of matrix subdivision, none of the above shape factor calculation is directly applicable. Since the matrix blocks are partitioned into sub-blocks in each direction, the radial flow in the matrix block is eventually decomposed into local linear

flow in matrix sub-blocks. Moreover, the shape factor of Kazemi et al. (1976) is similarly based on linear flow transfer between matrix and fracture. Therefore, to derive a shape factor formulation for subdivided matrix block, it is expected to be good to use similar derivations of the shape factor of Kazemi et al. (1976), and then validate it through numerical results. Let's briefly go through their derivation of shape factor.

2.2.1 Previous Model for Bulk Matrix

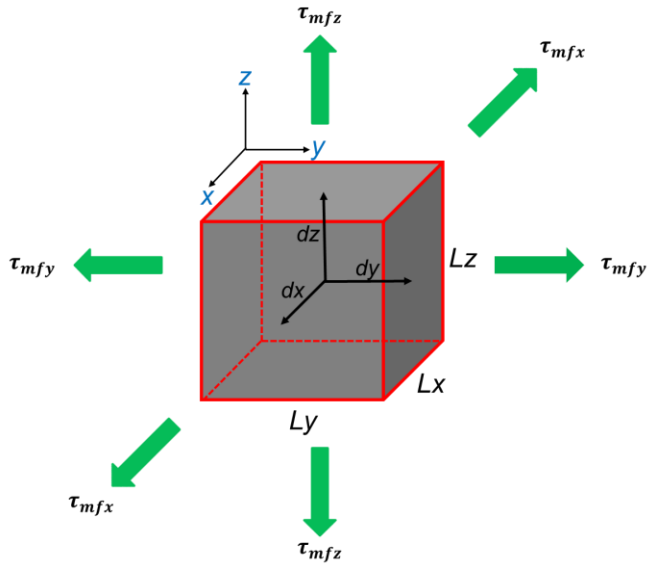

Fig. 2.1—Schematic of fluid flowing from a bulk matrix block (gray) to outer surrounding fractures (transparent)

Fig. 2.1 shows the schematic of transfer flux between a matrix block and its outer fractures, which are transparent for better visualization. Matrix block sizes a L_x, L_y, and L_z in x, y and z directions respectively. Define the mass transfer flow rate in each

direction as $\tau_{mfi}, i = x, y, z$; define the distance from the matrix block center to the matrix-fracture interface in i direction as $d_i = \frac{1}{2} L_i, i = x, y, z$; define the contact area of matrix block and fracture in x, y and z directions as $A_x = L_y L_z$, $A_y = L_x L_z$, $A_z = L_x L_y$ respectively; define matrix block volume is $V_m = L_x L_y L_z$. Assuming linear potential gradient inside bulk matrix block, the potential within the single matrix block is averaged as a single value Φ_m, and potential in fracture is a constant boundary condition Φ_f. Thus the flow through both matrix outer surfaces in each direction is symmetric, shown as Equation (2.7),

$$\tau_{mf} = 2(\tau_{mfx} + \tau_{mfy} + \tau_{mfz}) \tag{2.7}$$

Based on Darcy's law, τ_{mfi} can be written as Equation (2.8),

$$\tau_{mfi} = \rho \frac{k_{mfi} A_i}{\mu} \frac{\Phi_m - \Phi_f}{d_i + d_f}, \qquad (i = x, y, z) \tag{2.8}$$

Substitute Equation (2.8) into Equation (2.7), it becomes Equation (2.9),

$$\tau_{mf} = 2\left(\frac{k_{mfx} A_x}{d_x + d_f} + \frac{k_{mfy} A_y}{d_y + d_f} + \frac{k_{mfz} A_z}{d_z + d_f}\right)\frac{\rho}{\mu}(\Phi_m - \Phi_f) \tag{2.9}$$

Considering that usually fracture aperture is far smaller than the matrix block size ($d_f \ll L_i$ or $d_f \ll d_i$). Equation (2.9) is further reduced to Equation (2.10),

$$\tau_{mf} \approx \frac{\rho V_m}{\mu}\{4(\frac{k_{mfx}}{L_x^2} + \frac{k_{mfy}}{L_y^2} + \frac{k_{mfz}}{L_z^2})\}(\Phi_m - \Phi_f) \tag{2.10}$$

Therefore, compared to the Equation (2.3), the product of shape factor σ and permeability k in Kazemi et al. (1976) is accordingly,

$$(\sigma k)_{mf} = 4\left(\frac{k_{mfx}}{L_x^2} + \frac{k_{mfy}}{L_y^2} + \frac{k_{mfz}}{L_z^2}\right) \tag{2.11}$$

2.2.2 New Model Considering Matrix Subdivision

Based on the derivation in Section 2.2.1, this section focuses on how to derive the shape factor for a subdivided matrix block.

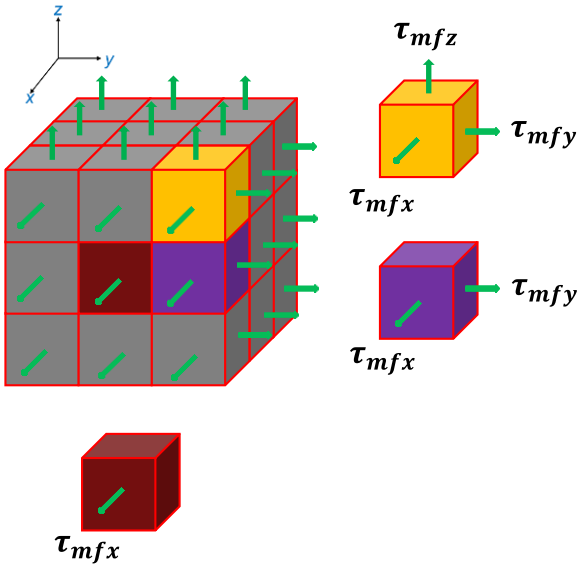

Fig. 2.2—Schematic of matrix-fracture transfer for subdivided matrix: different matrix sub-blocks have different number of surfaces connected to fracture system

In **Fig. 2.2**, it shows that a matrix block separated into 3 by 3 by 3 sub-blocks. In total there are 26 connection pairs of matrix sub-block and fracture in x, y, z directions,

except that the center matrix sub-block has no connection to the fracture system. Analog to the derivation of the model of Kazemi et al. (1976), the shape factor of matrix subdivision is derived in the following, but here all the matrix geometric properties are for each individual matrix sub-block instead of the bulk matrix block in Section 2.2.1. Here we start the derivation from Darcy's law and decompose the transfer rate of matrix sub-block into three directional components $\tau_{mfi}, i = x, y, z$. The following Equation (2.12) shows the transfer rate component through a single sub-block surface normal to x direction.

$$\tau_{mfx} = \frac{\rho}{\mu} \frac{k_{mfx} A_x}{d_x + d_f} \left(\Phi_m - \Phi_f\right) \tag{2.12}$$

Based on the assumption $d_f \ll d_i$, Equation (2.9) is transformed to Equation (2.10). Here similarly Equation (2.12) is written in the form of Equation (2.13),

$$\tau_{mfx} = \frac{\rho V_m}{\mu} \left\{2 \frac{k_{mfx}}{L_x^2}\right\} \left(\Phi_m - \Phi_f\right) \tag{2.13}$$

Therefore, a shape factor for a matrix sub-block connected with fracture in x direction is defined as Equation (2.14),

$$(\sigma k)_{mfx} = 2 \frac{k_{mfx}}{L_x^2} \tag{2.14}$$

This can be easily extended to the case that matrix sub-blocks are connected to fractures in any direction of i $(i = x, y, z)$, shown as Equation (2.15),

$$\tau_{mfi} = \frac{\rho V_m}{\mu} (\sigma k)_{mfi} \left(\Phi_m - \Phi_f\right) \tag{2.15}$$

where $(\sigma k)_{mfi} = 2\frac{k_{mfi}}{L_i^2}, i = x, y, z$. The shape factor here is for one contacting surface between the fracture and matrix sub-blocks. Let f_i represent the number of surfaces of a matrix sub-block connected to fracture system. For an arbitrary matrix sub-block with arbitrary division in the directions of $i = x, y, z$, f_i is possibly equal to 0, 1 or 2. Based on the symmetry of mass transfer in each direction, a general shape factor considering all possible fracture connected surfaces is proposed to be written as Equation (2.16).

$$(\sigma k)_{mf} = f_x\,(\sigma k)_{mfx} + f_y\,(\sigma k)_{mfy} + f_z\,(\sigma k)_{mfz} \tag{2.16}$$

For example, if a rectangular matrix block is not subdivided and connected to fractures in its 6 surfaces normal to x, y, z directions, it is valid that $f_i = 2, i = x, y, z$. Thus the model of Kazemi et al. (1976) can be derived as Equation (2.17),

$$(\sigma k)_{mf} = 2(\sigma k)_{mfx} + 2(\sigma k)_{mfy} + 2(\sigma k)_{mfz} = 4(\frac{k_{mfx}}{L_x^2} + \frac{k_{mfy}}{L_y^2} + \frac{k_{mfz}}{L_z^2}) \tag{2.17}$$

Therefore, $(\tau k)_{mf}$ from Kazemi et al. (1976) is a special case of the new shape factor model. Besides, the model of "Subdomain" (Fung 1991; Gilman and Kazemi 1988) is also a special case o1f this model, since it subdivides matrix block only in z direction to improve calculation of gravity displacement and here subdivision in all directions is allowed. As a result, the new model naturally improves the characterization of gravity effect and fluid phase segregation. The new model is more general and suitable for matrix block allowing arbitrary subdivision in any directions. Because of the decomposition of

the original transfer flow in bulk matrix block, theoretically it is a perfect approach to characterize non-linear fluid transfer between matrix and fracture.

2.2.3 Numerical Results

In this section, numerical solution of shape factor are calculated based on our in-house simulator (Yan et al. 2013b). This is a Single-Porosity Model, and fracture and matrix media are represented by different cells. Fracture serves as constant pressure boundary condition. Methane (compressible gas) is used as fluid flowing in the model, and real gas properties are calculated through cubic Peng-Robinson EOS. Basically we are solving the diffusivity equation for the system, shown as Equation (2.18), and the initial condition and boundary condition are shown as Equations (2.19) and (2.20) respectively. The whole nonlinear system is solved by fully implicit approach (Newton-Raphson method). After solving the system, to calculate shape factors some extra parameters are necessarily calculated, including the flux for those connections between matrix and fracture grids, and average fluid properties and permeability between matrix and fracture.

$$\nabla \cdot \left[\frac{\rho k}{\mu}(\nabla \Phi)\right] = \frac{\partial(\phi \rho)}{\partial t} \tag{2.18}$$

$$\Phi_m = \Phi_0 \ \ (when\ t = 0) \tag{2.19}$$

$$\Phi_f = constant\ (when\ t > 0) \tag{2.20}$$

To consider shape factors of all the directions and permeability anisotropy, a case with a matrix block subdivided into 6 by 6 by 6 matrix sub-blocks (grids) with fracture

grids surrounding the matrix bulk in three directions, and detailed parameters are shown in **Table 2.2**. The shape factors of bulk matrix block (treating 6 by 6 by 6 matrix sub-blocks as a grouped block) and each single matrix sub-block are calculated based on numerical models and then compared with analytical solutions. The results show great consistency between them. Note that the fracture permeability is not directly calculated based on fracture aperture. Instead, the fracture conductivity is fixed at 3,280.84 $mD \cdot ft$ to make the fracture infinitely conductive, and scale up the fracture grid size (fracture aperture) to avoid extremely small cell volume during simulation. This approach has been used by Rubin (2010) in his CMG simulation workflow to model hydraulic fractures in unconventional reservoirs, and the accuracy of the results is conserved during this grid scale-up process.

Table 2.2—Basic parameters to calculate shape factors

Matrix Sub-Block L_x (ft)	3.28084
Matrix Sub-Block L_y (ft)	6.56168
Matrix Sub-Block L_z (ft)	9.84252
Matrix Block L_x (ft)	19.6850
Matrix Block L_y (ft)	39.3701
Matrix Block L_z (ft)	59.0551
Fracture Aperture (ft)	0.328084
Fracture Permeability k_f $(Darcy)$	10
Matrix Permeability in x Direction k_{mx} (mD)	50
Matrix Permeability in y Direction k_{my} (mD)	10
Matrix Permeability in z Direction k_{mz} (mD)	5
Initial pressure $(psia)$	2900
Fracture pressure $(psia)$	1450 for $t > 0$
Temperature (°F)	212 for $t > 0$

For shape factor of bulk matrix block, most of the formulae follow the form of Equation (2.5) or (2.6) with different β values. Considering permeability anisotropy in this case, $(\sigma k)_{mf}$ from Equation (2.6) is used here, since it is directly involved in the transmissibility of matrix-fracture flux in Dual-Porosity Models. Based on Equation (2.3), $(\sigma k)_{mf}$ is calculated through Equation (2.21) directly from numerical results, where μ, ρ are averaged between matrix and fracture. Based on Equation (2.6), the value of β is calculated through Equation (2.22).

$$(\sigma k)_{mf} = \frac{\mu_{mf}\tau_{mf}}{\rho_{mf}(\Phi_m - \Phi_f)V_m} \tag{2.21}$$

$$\beta = \frac{(\sigma k)_{mf}}{\left(\frac{k_{mfx}}{L_x^2} + \frac{k_{mfy}}{L_y^2} + \frac{k_{mfz}}{L_z^2}\right)} \tag{2.22}$$

The numerical result of β is plotted as the red marker curve in **Fig. 2.3**, and two constant solutions for β from traditional models are also presented for comparison. In **Fig. 2.3**, it shows that β from numerical result declines with time, and ultimately converges to π^2, which is the result of β from Lim and Aziz (1995) but not that from Kazemi et al. (1976). This can be explained by that Lim and Aziz's model can better characterize the nonlinear pressure gradient in the matrix, but the model of Kazemi et al is based on a linear pressure gradient in the matrix. Here Equation (2.21) is similar to the apparent permeability defined by Yan et al. (2015), so consistently in **Fig. 2.3** it shows that the numerical result of β declines with time and finally converges to the stable value.

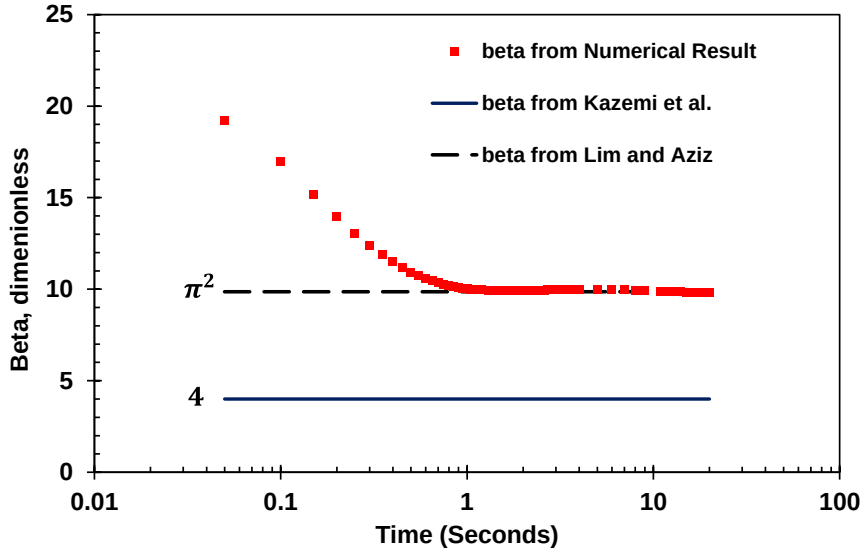

Fig. 2.3—Comparison of numerical and analytical results of β in Equation (2.6)

Further, the shape factors of each matrix sub-block connected to fractures are analyzed. In this model, there are in total 216 connections between matrix sub-blocks and fractures. In **Table 2.2**, it shows that the matrix sub-blocks have different sizes in different directions, and anisotropy of matrix permeability is considered as well. As a result, it is appropriate to analyze the numerical result of β for each connection between individual matrix sub-block and fracture grid block. Based on previous analysis, Equation (2.6) is a special case of Equation (2.16), with $f_x = f_y = f_z = 2$. Therefore, the value of σ_{mfi} can be expressed as,

$$\sigma_{mfi} = \frac{\beta}{2}\frac{1}{L_i^2}, i = x, y, z \tag{2.23}$$

Similar to the scenario of bulk matrix block, Equation (2.21) is still valid here for each individual connection of matrix sub-block and fracture, but the properties of matrix are from individual matrix sub-block instead of the bulk matrix block, and thus the numerical value of σ_{mfi} is,

$$\sigma_{mfi} = \frac{\mu_{mf}\,\tau_{mfi}}{\rho_{mf}\,k_{mfi}\,(\Phi_m - \Phi_f)V_m} \tag{2.24}$$

Based on Equation (2.23) and (2.24), β is,

$$\beta = 2L_i^2 \frac{\mu_{mf}\tau_{mfi}}{\rho_{mf}k_{mfi}(\Phi_m - \Phi_f)V_m} \tag{2.25}$$

Here values of β are calculated for all 216 connection pairs of matrix sub-block and fracture, and all of them ultimately converge to a single value. For a better visualization, here only the converged values of β for all connections are plotted, as shown in **Fig. 2.4**. In **Fig. 2.4**, it shows that for each individual connection of matrix sub-block and fracture, β values are fairly close to that of Kazemi et al. (1976). This can be explained by the fact that the local matrix sub-block is evaluated here, and the original radial flow in the bulk matrix block is decomposed to linear flow because of the matrix subdivision. To this point, the results are very consistent with our previous derivation of shape factor considering matrix subdivision in Section 2.2.2. On the other hand, for cases without matrix subdivision, the model of Lim and Aziz (1995) or Zimmerman et al. (1993) is preferable to that of Kazemi et al. (1976) for constant fracture pressure condition.

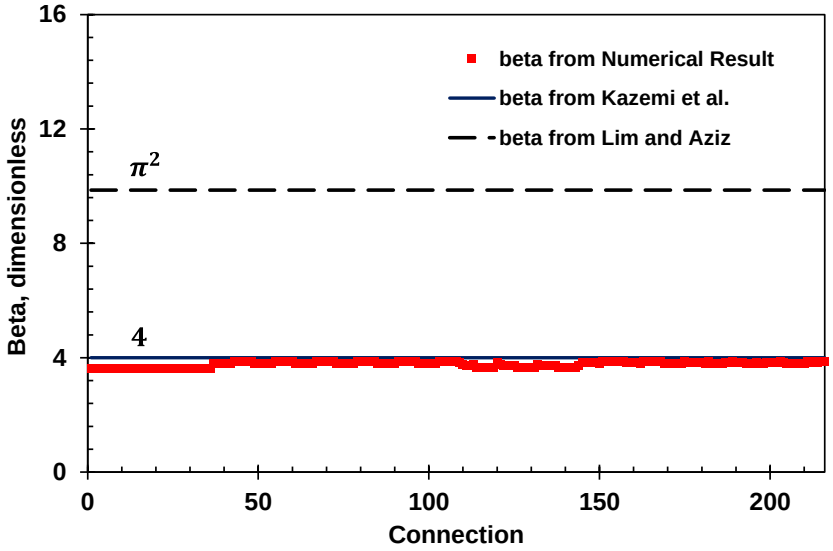

Fig. 2.4—Comparison of numerical and analytical results of β in Equation (2.23)

2.3 Multi-Porosity Model

Assume that Darcy's law applies to a Multi-Porosity Model with N number of porosity types, the mass balance equation for a multi-phase black-oil fluid system is shown as Equation (2.26).

$$\nabla \cdot \left\{ \rho_\alpha \frac{k_i k_{r\alpha}}{\mu_\alpha} \left(\nabla \Phi_{\alpha,i} \right) \right\} - \sum_{j \neq i} \tau_{\alpha(j,i)} = \frac{\partial (\rho_\alpha \phi S_\alpha)}{\partial t} + Q_\alpha, (i = 1, \dots, N; j = 1, \dots, N) \quad (2.26)$$

$$\tau_{\alpha(j,i)} = \sigma \rho_\alpha V_i \frac{k_{ij} kr}{\mu_\alpha} \left\{ \Phi_{\alpha,j} - \Phi_{\alpha,i} \right\}, (i = 1, \dots, N; j = 1, \dots, N; i \neq j) \quad (2.27)$$

In Equation (2.26), the first term is a conventional convection flux term, the second term is a summation of all fluid transfer flux rate between i^{th} porosity system and other connected porosity systems, the third term is accumulation term, and the fourth term is source/sink term. If there is no conventional convection flux term in i^{th} porosity system,

this porosity system will only consider inter-porosity flux from/to other porosity systems (such as the matrix porosity in Dual-Porosity Single-Permeability Model). Meanwhile, if there is no transfer flux between i^{th} and j^{th} porosity, direct flow interaction between them will not be considered. In Equation (2.27) the transfer term between different porosity systems is calculated. If there is no porosity subdivision, the shape factor can be calculated either by different models or user-specified. If any porosity domain is subdivided, the shape factor is calculated based on Equation (2.16).

There are two different configurations in the Multi-Porosity Model. The first configuration is conventional Multi-Porosity Model, which is similar to the model from HinkleyWang et al. (2013). This configuration is naturally compatible with the formulation above. A Quad-Porosity Model with four porosity systems is shown in **Fig. 2.5**, which includes P1, P2, P3, and P4. Here all porosity systems are discretized in the same fashion. Therefore, the non-neighbor connection between different porosity systems is always a one-to-one mapping process.

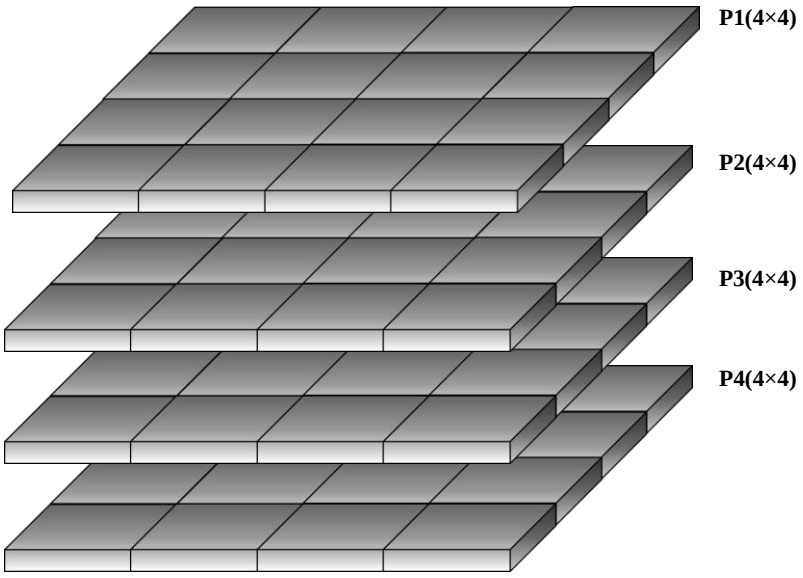

Fig. 2.5—Conventional Multi-Porosity Model

The second configuration is Multi-Porosity Model with Subdivision (**Fig. 2.6**). This model is designed to capture the transient flow in some porosity systems if necessary. For example, a shale reservoir can be treated as a Quad-Porosity Model, since it is widely accepted that there exist four porosity systems (Wang and Reed 2009), including hydraulic fractures, natural fractures, inorganic matrix and organic matrix. Among them hydraulic fractures have higher conductivity than natural fractures; on the other hand, those two tight matrix systems have different wettabilities and fluid transport mechanisms (Alfi et al. 2015). Since the inorganic and organic matrix permeability is much lower than that in the hydraulic and natural fractures, transient fluid transfer occurs between matrix and fracture. To accurately capture this phenomenon, a hierarchical porosity subdivision scheme is used to discretize different porosity systems, shown in **Fig. 2.6**. In **Fig. 2.6**, the non-neighbor connection in the discretization scheme is no longer a one-to-one mapping process.

Specifically, 1 grid in hydraulic fracture system is corresponding to 4 grids in natural fracture system, such that those two fracture sets with different conductivity can be distinguished. Further, 1 grid in natural fracture system is corresponding to 16 grids in inorganic matrix and organic matrix, which depicts the transient flow more accurately.

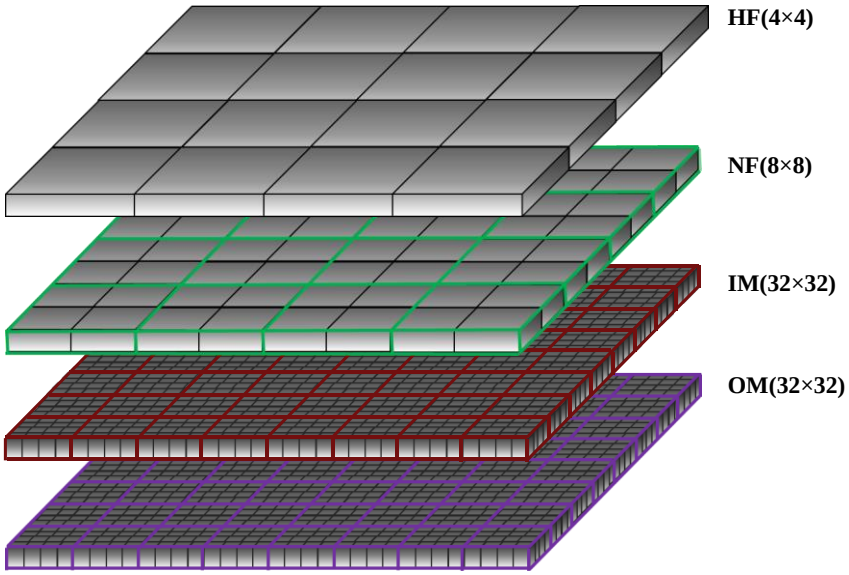

Fig. 2.6—Multi-Porosity with Subdivision: "HF" – hydraulic fractures; "NF" – natural fractures; "IM" – inorganic matrix; "OM" – organic matrix.

In a Multi-Porosity Model with flexible subdivision, the grid number in each porosity domain can be either equal (**Fig. 2.5**) or different (**Fig. 2.6**), and thus the design becomes difficult. Therefore, the grid information and connection information would be better stored in an unstructured format (Lim et al. 1995), and this is consistent with the configuration of our in-house black-oil simulator (Yan et al. 2013b) or GURU developed later in this work, which is formulated in Control-Volume Finite-Difference (CVFD)

method. Specifically, all grid-based properties are stored through an ordered list, such as grid name, pore volume, rock type, phase saturation etc., and all connection-based properties are stored through a connection list, such as names of two grids in a connection, connection type, and transmissibilities etc. As for the ordering of porosity types, HinkleyWang et al. (2013) recommended that the porosity type with the highest permeability is first and the one with the lowest permeability comes last, and this facilitates the LU factorization process.

Besides, in the traditional Dual-Porosity Model, a fracture grid is always connected with a matrix grid in the same physical location, and thus even those inter-porosity properties are conveniently treated as grid-based properties. However, in our design, a porosity type might be connected to multiple other porosity types (inter-porosity connection), and also flow within each porosity type (intra-porosity connection) can also be active or inactive. Therefore, the scenario here is much more complex than that in Dual-Porosity Model, and thus here a binary connection table is proposed to solve this problem conveniently. For example, **Fig. 2.7** is a fluid transport pyramid for a Quad-Porosity Dual-Permeability Model. In this model P1 and P2 are connected to all porosity types and flow among themselves is permitted as well; P3 and P4 are both only tied to P1 and P2 in parallel and flow among themselves is not allowed here. To effectively characterize this, **Table 2.3** is a binary connection table designed to control the inter-porosity and intra-porosity connection from **Fig. 2.7**. In **Table 2.3**, value "1" represents an active connection between two porosity types while value "0" means an inactive connection. Because of the natural symmetry in connection, the binary connection table is symmetric as well. Here in

the table the main diagonal entries control the intra-porosity connection, and those off-diagonal entries control the inter-porosity connections. Therefore, through changing the values in the table, arbitrary inter-porosity and intra-porosity in a model is effectively controlled.

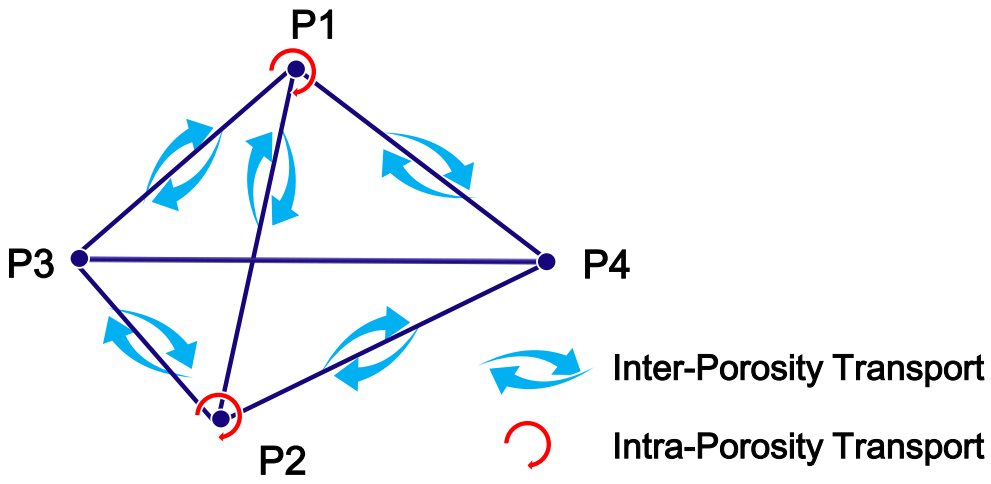

Fig. 2.7—Fluid transport pyramid of Quad-Porosity Dual-Permeability Model (four porosity types: P1, P2, P3, P4)

Table 2.3—Binary connection table to control connections of 4 porosity types in Fig. 2.7

	P1	P2	P3	P4
P1	1	1	1	1
P2	1	1	1	1
P3	1	1	0	0
P4	1	1	0	0

Following the binary connection **Table 2.3**, assume that single phase fluid flow in the models in **Fig. 2.5** and **2.6**. The Jacobian matrix of the Quad-Porosity Dual-Permeability Models in **Fig. 2.5** and **2.6** are respectively shown in **Fig. 2.8 (a)** and **(b)**.

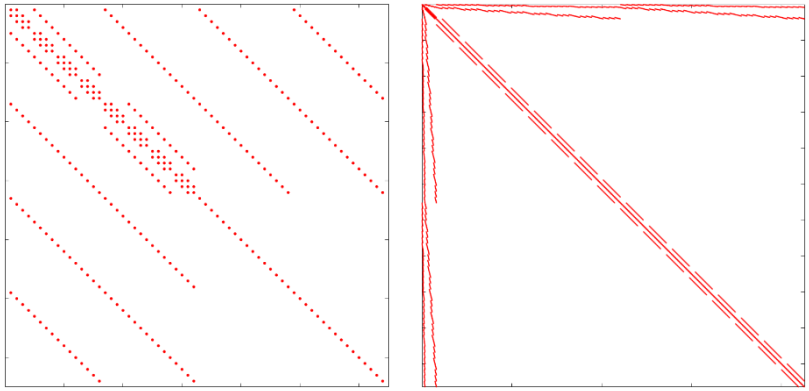

(a) (b)

Fig. 2.8—Jacobian matrices of Quad-Porosity Dual-Permeability Models (QPDK): (a) Jacobian matrix for Fig. 2.5 without matrix subdivision; (b) Jacobian matrix for Fig. 2.6 with matrix subdivision.

In **Fig. 2.8(a)**, the porosity ordering sequence follows P1-P2-P3-P4, we can observe that the whole Jacobian matrix is structured and banded, because the non-neighbor connection between different porosity systems is one-to-one mapping. Besides, those diagonal terms are mainly intra-porosity flux Jacobian and accumulation Jacobian, while the off-diagonal terms are mainly inter-porosity flux Jacobian. Similarly, the porosity ordering sequence in **Fig. 2.8(b)** follows HF-NF-IM-OM. Because here the non-neighbor connection between different porosity systems is no longer one-to-one mapping, there are irregular patterns in the off-diagonal terms for the inter-porosity flux Jacobian. Further,

there are three diagonal bands in the lower right part of the Jacobian, since here the matrix domain is subdivided and intra-matrix flux is captured by high resolution.

2.4 Summary

In this chapter, starting from conventional Dual-Porosity Models, a general shape factor formulation considering matrix subdivision in arbitrary direction is derived, and it is comprehensively validated with numerical experiments. Besides, the original model of Kazemi et al. (1976) is demonstrated to be a special case of this formulation. Based on the porosity subdivision and the new shape factor formulation, a general Multi-Porosity Model is proposed to honor arbitrary modeling porosity types and flexible porosity subdivisions, and also conventional Multi-Porosity Model without subdivision is considered as one of configurations here. The Multi-Porosity Model is developed in unstructured fashion, such that it naturally becomes compatible with unstructured reservoir simulator. Besides, the intra-porosity and inter-porosity connection in the Multi-Porosity Model is flexibly controlled through a binary connection table.

CHAPTER III

VALIDATION OF GENERAL MULTI-POROSITY MODEL*

Based on the previously developed Multi-Porosity Model, the main purpose of this chapter is to demonstrate its robustness. Specifically, three subtopics are discussed in this chapter, shown as the following,

- Verification of Dual-Porosity Model;
- Verification of Triple-Porosity Model;
- Application of Multi-Porosity Model to two phase shale gas reservoir modeling.

3.1 Dual-Porosity Models

Dual-Porosity is a special case of Multi-Porosity Model when the number of porosity systems is two. Therefore, Dual-Porosity Model is firstly verified. To validate our implementation of the Dual-Porosity Model, three examples similar to Lim and Aziz (1995) were used to validate the application of different shape factors, and further the matrix subdivision in Dual-Porosity Model is applied to see if it would make any difference in solution.

* Part of the this chapter is reprinted with permission from "General Multi-Porosity Simulation for Fractured Reservoir Modeling" by Yan B., Alfi M., An C., Cao Y., Wang Y., Killough J., 2016.` Journal of Natural Gas Science and Engineering, Volume 33, Pages 777-791, Copyright 2016 by Elsevier. Part of this chapter is reprinted with permission from "Extended Abstract: Advanced Multiple Porosity Model for Fractured Reservoirs" by Yan B., Alfi M., An C., Cao Y., Wang Y., Killough J., 2015. Paper presented at the International Petroleum Technology Conference (IPTC 2015). Copyright 2015 by SPE.

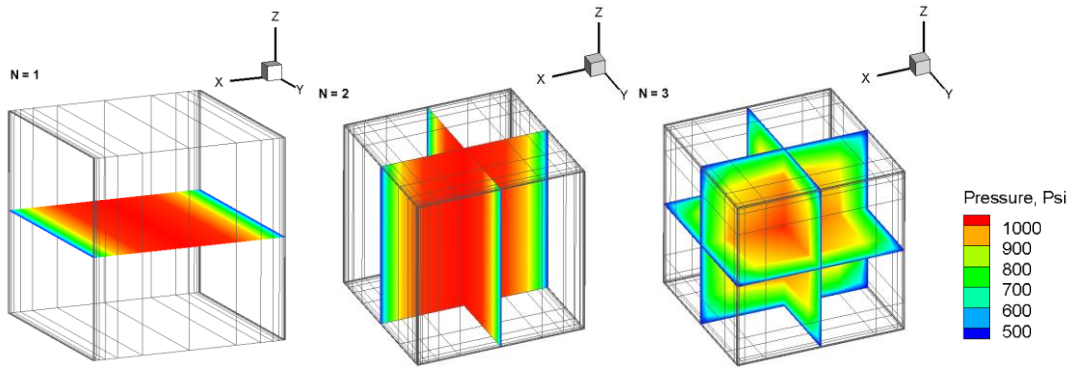

Fig. 3.1—Fine-Grid Single-Porosity Models for $N = 1, 2, 3$.

Fig. 3.1 shows three different cases of Fine-Grid Single-Porosity Models. When $N = 1$, a matrix block is bounded by 1 set of fractures in x direction (only discretized in x direction); when $N = 2$, a matrix block is bounded by 2 sets of fractures in both x and y directions (discretized in x and y directions); when $N = 3$, a matrix block is bounded by 3 sets of fractures in x, y and z directions (discretized in x, y and z directions). Besides, logarithmic grid spacing around the fractures is applied to resolute the transient flow in Single-Porosity Models, and their results are treated as calibrated solutions. As a comparison, the Dual-Porosity Models are set in equal model size with corresponding Single-Porosity Models, and they have only one grid block for matrix and fracture respectively. Besides, in Dual-Porosity Models, fracture permeability values are scaled to keep the same fracture conductivity (Rubin 2010), and fracture porosity values are modified to conserve the pore volume.

Table 3.1 shows necessary data for comparison between Fine-Grid Single-Porosity Models and Dual-Porosity Models. Note that there are no wells in those Fine-Grid Single-Porosity Models and Dual-Porosity Models, however, fracture systems are set

as constant pressure boundary conditions, $p_f = 500\,psia$, and initial matrix pressure is $p_m = 1{,}000\,psia$. Because of the pressure contrast between matrix and fracture, fluid in the matrix flows into the fracture system in different directions. **Fig. 3.1** shows the pressure profile at early periods in the three different Fine-Grid Single-Porosity Models, and it presents that transient flow effect occurs in those regions neighboring the fracture systems. In Lim and Aziz's cases, fluid properties are correlated from steam table, and here in the cases of this work, the fluid is methane and it properties are calculated through Peng-Robinson EOS.

Table 3.1—Parameters for Fine-Grid Single-Porosity Models and Dual-Porosity Models

Fine grid, N = 1	
Grid dimensions	22 x 1 x 1
Grid spacing (ft)	Δx = 0.005, 0.005, 0.01, 0.02, 0.04, 0.08, 0.16, 0.32, 0.64, 1.28, 2.445, 2.445, 1.28, 0.64, 0.32, 0.16, 0.08, 0.04, 0.02, 0.01, 0.005, 0.005;
	$\Delta y = \Delta z$ = 10;
Fine grid, N = 2	
Grid dimensions	22 x 22 x 1
Grid spacing (ft)	$\Delta x = \Delta y$ = same as Δx for N = 1;
	$\Delta z = 10$
Fine grid, N = 3	
Grid dimensions	12 x 12 x 12
Grid spacing (ft)	$\Delta x = \Delta y = \Delta z =$ 0.01, 0.02, 0.08, 0.32, 1.28, 3.30, 3.30, 1.28, 0.32, 0.08, 0.02, 0.01;
Rock properties for fine grid models	
Matrix porosity	0.05
Matrix permeability (mD)	0.001
Fracture porosity	1.0
Fracture permeability (mD)	100,000
Dual-Porosity	

Table 3.1—Continued.

Grid dimensions	1 by 1 by 1
Grid spacing (ft)	$\Delta x = \Delta y = \Delta z = 10$
Matrix porosity	0.05
Matrix permeability (mD)	0.001
Fracture porosity	0.001 (N = 1); 0.002 (N = 2); 0.006 (N = 3);
Fracture permeability (mD)	100
Reservoir conditions for all models	
Initial pressure ($psia$)	1000
Fracture pressure ($psia$)	500 for $t > 0$
Initial temperature (°F)	600 for $t > 0$

Dual-Porosity Models based on the shape factors of Warren and Root (1962), Kazemi et al. (1976), Coats (1989), and Lim and Aziz (1995) are compared with corresponding Fine-Grid Single-Porosity Models. All cases here are for single-phase compressed gas flow, and cumulative gas production with time for $N = 1, 2, 3$ are all plotted in **Fig. 3.2.**

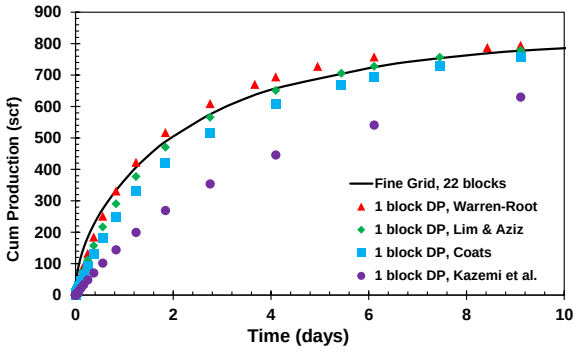

(a)

Fig. 3.2—Cumulative gas production for three different sets of cases: (a) $N = 1$: 1 set of fractures; (b) $N = 2$: 2 sets of fractures; (c) $N = 3$: 3 sets of fractures.

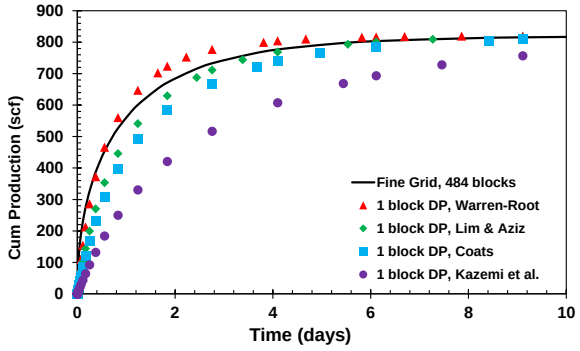

(b)

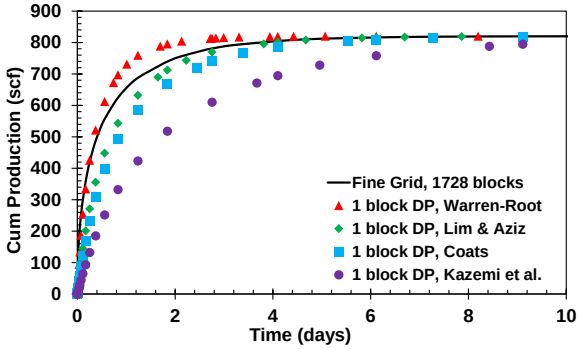

(c)

Fig. 3.2—Continued

In **Fig. 3.2**, the results of those Dual-Porosity Models with Lim and Aziz's shape factor are in good consistency with Fine-Grid Single-Porosity Models for most of the time scale, but those results based on shape factors of Kazemi et al are far smaller than that of the calibrated Fine-Grid Single-Porosity models. This can be explained by our previous analysis that Kazemi's model assumes a linear flow between matrix and fracture, and it

underestimates the matrix-fracture transfer rate. Besides, in all the three figures in **Fig. 3.2**, the results are consistently shown in sequence: (DP, Warren-Root) > (Fine Grid Model) > (DP, Lim and Aziz) > (DP, Coats) > (DP, Kazemi et al.), which makes good agreement with Lim and Aziz's results (Lim and Aziz 1995), and this can also be explained by the relative magnitude of shape factors in different models. Therefore, these results above have already proven the robustness of our implementation for Dual-Porosity Model configuration.

The transient flow between fracture and matrix usually occurs at the early period. Especially for reservoirs with high contrast of permeability in different porosity types, the transient flow usually lasts for a long period. From **Table 3.4**, the matrix permeability in Dual-Porosity Model is 100,000 times lower than the fracture permeability, therefore, the transient flow between matrix and fracture should be very important and last for a long time. Since all three series ($N = 1,2,3$) of Dual-Porosity Models without subdivision provide consistent results, let's observe the case with matrix bounded by three sets of fractures ($N = 3$, **Fig. 3.2(c)**) in a logarithmic time scale, shown as **Fig. 3.3**.

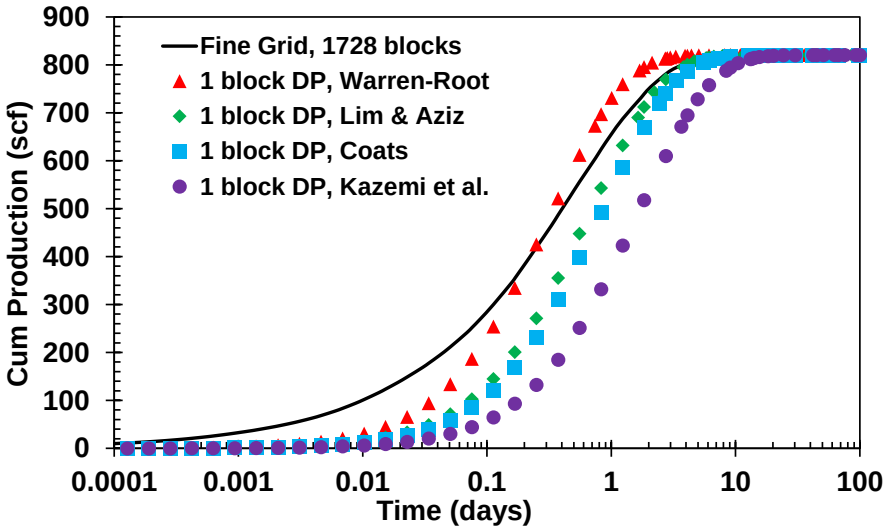

Fig. 3.3—Results for system with three sets of fractures in logarithmic time scale

Fig. 3.3 shows that at the early time none of those Dual-Porosity Models with classic shape factor models matches well with the calibrated Fine-Grid Single-Porosity Model, because there is only one matrix grid in all those Dual-Porosity Models, and this cannot accurately capture the non-linear transient flow between matrix and fracture.

Therefore, for the case $N = 3$, we will further consider if the subdivision in the matrix porosity is helpful to enhance the accuracy. Here, a series of Dual-Porosity Models with Matrix Subdivision based on the shape factor from Equation (2.16) are also compared with Fine-Grid Single-Porosity Model ($N = 3$). Those models correspond to the single porosity with 3 sets of fractures in **Fig. 3.1**, so there is no well in the model as well. Fracture system serves as a constant pressure boundary condition, $p_f = 500\,psia$, and matrix pressure is initially at $1{,}000\,psia$. Three cases of Dual-Porosity Models with matrix subdivision are simulated: the matrix grid dimensions of the three cases are

respectively 7 by 7 by 7, 9 by 9 by 9, and 11 by 11 by 11, and the fracture grid dimensions are still 1 by 1 by 1, and here logarithmic subdivision grid spacing in matrix domain is applied. **Fig. 3.4** is an example of Dual-Porosity Model with matrix subdivided into 9 by 9 by 9 grids. Other parameters for Dual-Porosity Models are the same as the Dual-Porosity Model ($N = 3$) in **Table 3.1**.

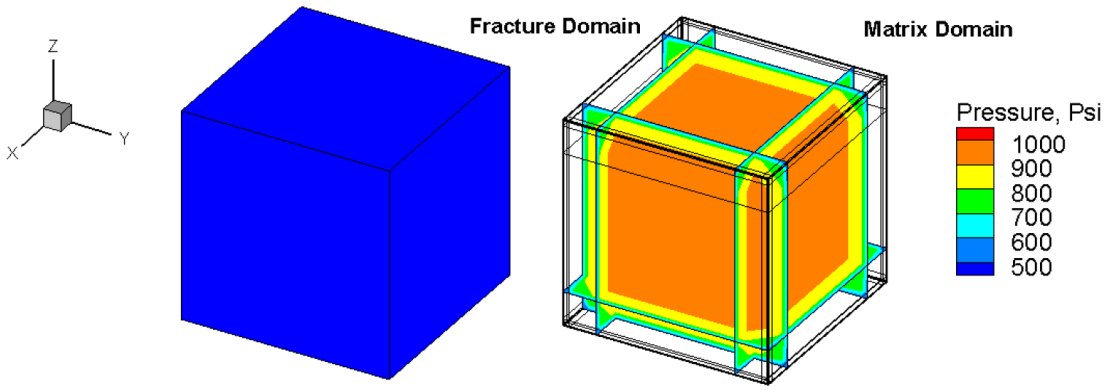

Fig. 3.4—Dual-Porosity Model with Matrix Subdivision: fracture, 1 grid; matrix, 9 by 9 by 9 grids.

The results are plotted in **Fig. 3.5** with Fine-Grid Single-Porosity Model as a calibrated model.

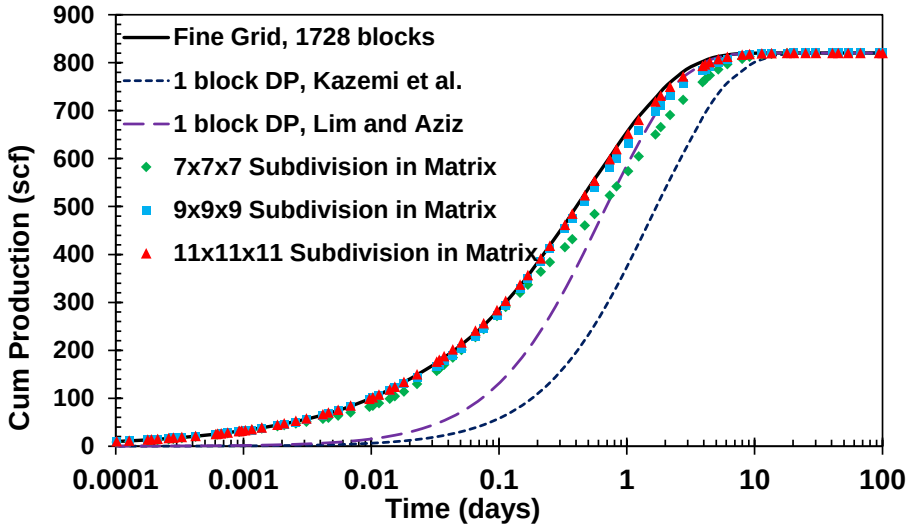

Fig. 3.5—Results for system with three sets of fractures, with matrix subdivision in Dual-Porosity Models, in logarithmic time scale

Fig. 3.5 shows that with the increase of matrix subdivision, the solutions of the three Dual Porosity Models with matrix subdivision (marker curves) get closer to the calibrated model (black solid line). Besides, we also present two Dual-Porosity Models without matrix subdivision (dash lines), whose shape factor are based on the model of Kazemi et al. (1976) and the model of Lim and Aziz (1995) respectively. Through comparison we can see that the transient flow at the early period in those Dual Porosity Models with Matrix Subdivision is far better captured than that in Dual Porosity Models without Matrix Subdivision, since with subdivision the non-linear flow between matrix block and fracture now becomes local linear flow between matrix sub-block and fracture with much higher resolution. This is consistent with our expectation.

3.2 Triple-Porosity Models

In the previous section the Dual-Porosity Models have been proved to be robust. Besides, good improvement on transient flow has been obtained with matrix subdivision scheme. Since Dual-Porosity Model is a special case of Multi-Porosity Model, we hope to validate the model with more porosity types as well.

In the following a gas reservoir model in 2-D is presented. In the reservoir, there are 6 sets of x-axis oriented fractures and 6 sets of y-axis oriented fractures partitioning the reservoir (matrix), and those x-axis oriented fractures have much higher permeability than those y-axis oriented fractures. In the reservoir a producer is located in the upper-left corner, cell (1, 1), which is also the intersection of the 1^{st} fractures in x and y directions, and the producer is constrained by constant bottom-hole pressure at $p_{wf} = 725\ psia$, and initial reservoir pressure is $p_0 = 4{,}350\ psia$. Details about the reservoir parameters are shown in **Table 3.2**. Since the permeability values in x-axis oriented fractures, y-axis oriented fractures, and partitioned matrix blocks are significantly different in magnitude, the reservoir is considered as a model with three different porosity types, and thus gas production from the reservoir is simulated by both Fine-Grid Single-Porosity Model and Triple-Porosity Models.

Table 3.2—Parameters for a model with 6 sets of x-axis oriented fractures (FX) and 6 sets of y-axis oriented fractures (FY)

Fine grid model	
Number of FX	6
Number of FY	6
Grid dimensions	$56 \times 56 \times 1$
Grid spacing (ft)	$\Delta x = \Delta y =$ 0.00328084, 0.328084x10, 0.00328084, 0.328084x10, 0.00328084, 0.328084x10, 0.00328084, 0.328084x10, 0.00328084, 0.328084x10, 0.00328084; $\Delta z =$ 0.328084;
Rock properties for fine grid model	
Matrix block size (ft)	$3.28084 \times 3.28084 \times 3.28084$
Matrix porosity	0.2
Perm. of matrix (mD)	0.01
Fracture aperture (ft)	0.00328084
Porosity of FX	1.0
Porosity of FY	0.1
Perm. of FX (mD)	1.0×10^5
Perm. of FY (mD)	1.0×10^3
Triple-Porosity Model	
Grid dimensions	$5 \times 5 \times 1$ for case without matrix subdivision
Grid spacing (ft)	$\Delta x = \Delta y =$ 3.2845, $\Delta z =$ 0.328084 for case without matrix subdivision
Porosity of matrix	0.2
Perm of matrix (mD)	0.01
Porosity of FX	1.1986×10^{-3}
Porosity of FY	1.1986×10^{-4}
Perm. of FX (mD)	100
Perm. of FY (mD)	1.0
Reservoir conditions for all models	
Initial pressure ($psia$)	4350
Well pressure ($psia$)	725 for $t > 0$
Temperature (°F)	180 for $t > 0$

Fine-Grid Single-Porosity is treated as a calibrated solution. **Fig. 3.6** is the pressure map at early production period from the model. In **Fig. 3.6**, it shows that pressure decreases more in x-axis direction than that in y-axis direction, because fracture conductivity in x-axis oriented fractures is higher than that in y-axis oriented fractures.

With fine grid discretization in matrix, transient flow between the matrix and fracture is well captured in **Fig. 3.6**.

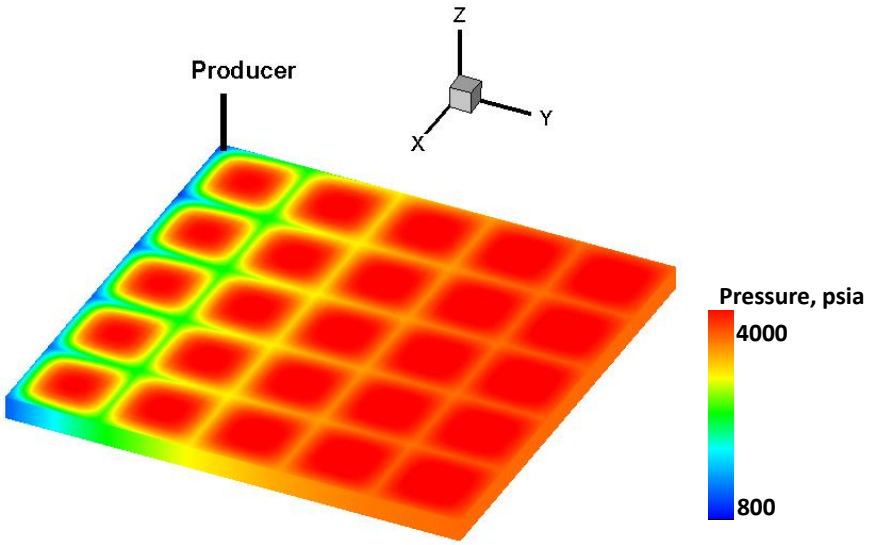

Fig. 3.6—Pressure profile of Fine-Grid Single-Porosity Model, time step: 0.002905 hours

Further, to simulate the reservoir through Triple-Porosity Model, those x-axis oriented fractures and y-axis oriented fractures are treated as two independent porosity domains because of their high contrast of permeability or conductivity. To conserve both pore volume and flow conductivity in fractures (Rubin 2010), values of fracture porosity and permeability in the Triple-Porosity Model are modified and thus different from those in Single-Porosity Model (**Table 3.2**). Besides, the matrix blocks in the reservoir (**Fig. 3.6**) are completely isolated by the two orthogonal fracture sets in the reservoir, so Triple-

Porosity Dual-Permeability Model (TPDK) is very appropriate here, in which fluid flow between different matrix blocks is not allowed.

In the Triple-Porosity Models, the producer with constant pressure constraint is perforated in cell (1, 1) in x-axis oriented fracture domain with the highest permeability, since in the Fine-Grid Single-Porosity Model (**Fig. 3.6**) this location is spatially perforated with the producer as well. The producer is constrained by constant bottom-hole pressure $p_{wf} = 725\ psia$, and initial reservoir pressure is $p_0 = 4350\ psia$.

In TPDK Models without Matrix Subdivision, results of different models to calculate shape factors are compared in **Fig. 3.7**. It shows that the model of Lim and Aziz (1995) can provide us with a much more accurate result than the model of Kazemi et al. (1976), and this is very consistent with our results of Dual-Porosity Models. However, during the early period (before 1 hour) even the model of Lim and Aziz (1995) deviates from the Fine Grid Model because of the inaccurate characterization of transient flow. For example at time of 0.01 hour, the model of Lim and Aziz (1995) produces 33.7% less than that from Fine-Grid Single Porosity Model, and the model of Kazemi et al. (1976) produces 59.75% less than that from Fine-Grid Single Porosity Model (note that here production rate is in logarithmic scale). This deviation might be more significant when the permeability contrast between matrix and fracture increases and transient flow lasts longer.

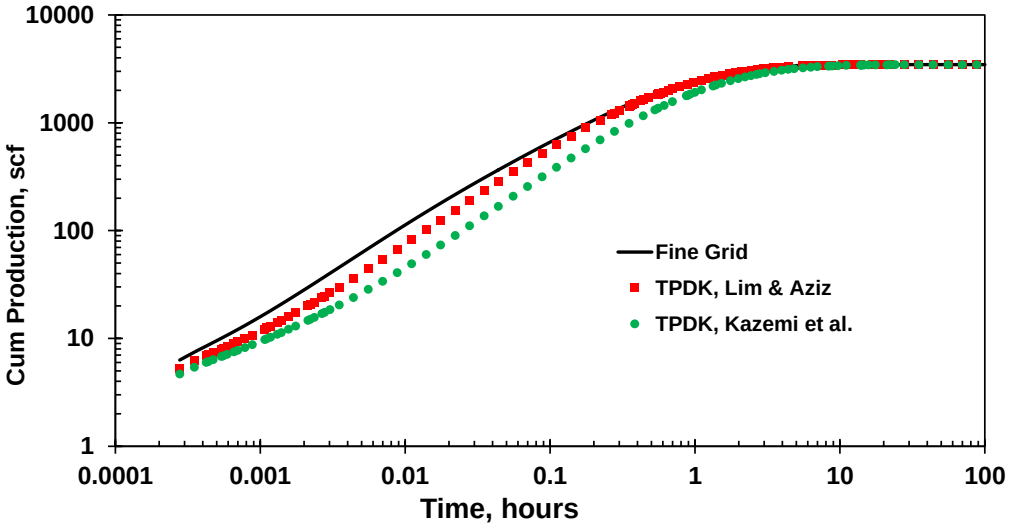

Fig. 3.7—Gas production comparison between Triple-Porosity Dual-Permeability (TPDK) Models without Matrix Subdivision (different shape factors) and Fine-Grid Single-Porosity Model

In TPDK Models with Matrix Subdivision, equal matrix subdivision is applied and three different cases of matrix subdivisions are presented, respectively 2 by 2 by 1, 4 by 4 by 1, and 6 by 6 by 1 in $x - y - z$ space, and the shape factor calculation for them is based on Equation (2.16). The results are shown in **Fig. 3.8**. In **Fig. 3.8**, it shows that with an increase of matrix subdivision in TPDK Models, the results gradually approach to that of the Fine-Grid Single-Porosity Model. When a matrix block is subdivided into 6 by 6 by 1 sub-blocks, the result of TPDK Model basically overlaps with the Single-Porosity Model, and only 2.4% rate difference exist between them. Similar to **Fig. 3.6**, **Fig. 3.9** is the pressure profile in different porosity system at the same time step in TPDK Model with 6 by 6 by 1 matrix subdivision. It shows that the pressure in the matrix is the highest, followed by y-axis oriented fracture system, and finally x-axis oriented fracture system.

This is consistent with the permeability rank in the three porosity systems (matrix < y-axis fracture < x-axis fracture). Besides, the transient flow in the matrix system is captured very well. Therefore, it further validates that the Multi-Porosity Model with Subdivision can significantly improve the solution for transient flow.

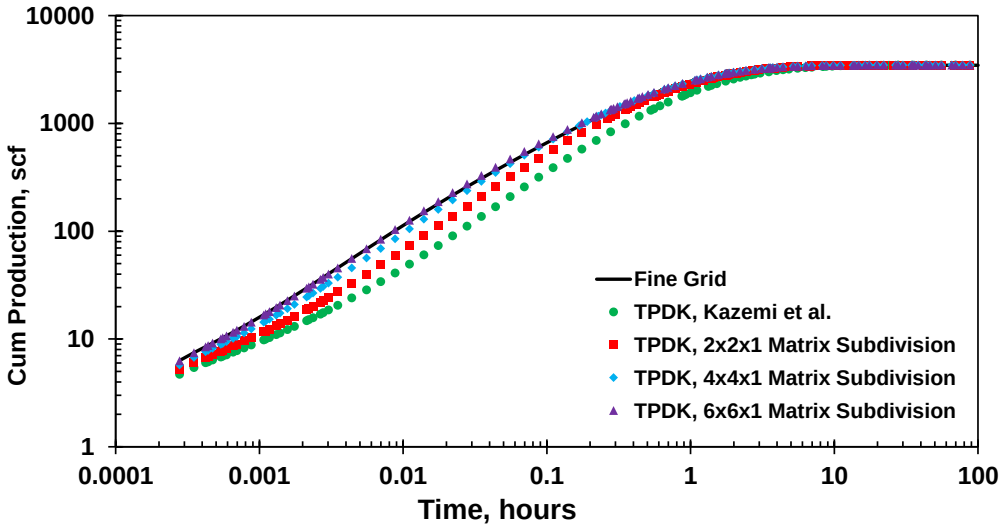

Fig. 3.8—Gas production comparison between Triple-Porosity Dual-Permeability (TPDK) Models with Matrix Subdivision and Fine-Grid Single-Porosity Model

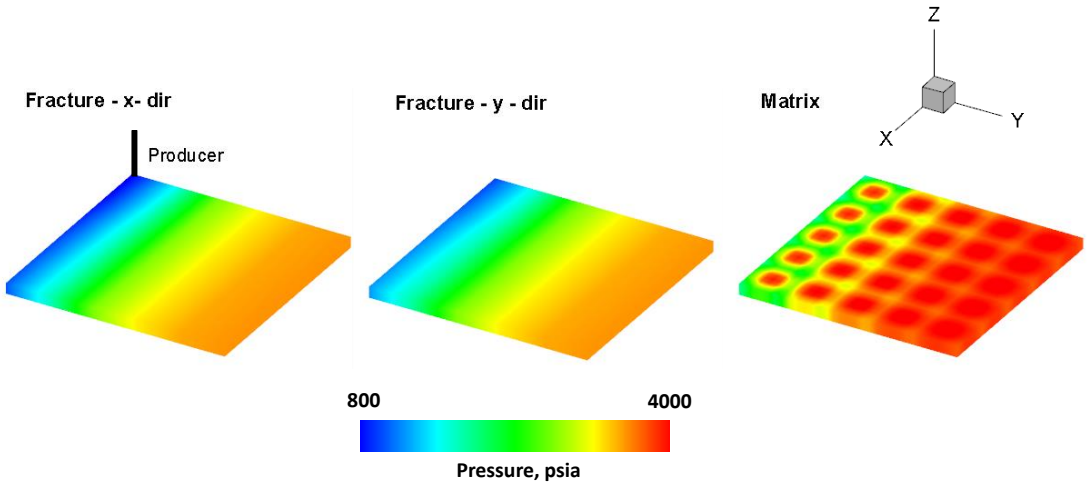

Fig. 3.9—Pressure profile of Triple-Porosity Dual-Permeability Model with 6 by 6 by 1 matrix subdivision. Time step: 0.002905 hours

Besides, the numbers of grid blocks used to discretize those different models are compared, and the results are presented in **Fig. 3.10**. Here the Fine-Grid Single-Porosity Model have used far more grid blocks than other models since it is treated as an accurate solution. In Triple-Porosity Dual-Permeability (TPDK) Models, the more the matrix subdivision, the larger the number of grid blocks. TPDK Model with shape factor of Kazemi et al. (1976) (purple bar) and TPDK Model with shape factor of Lim and Aziz (1995) (green bar) have no matrix subdivision and they have the smallest number of grid blocks. For TPDK Models with matrix subdivision, the larger the subdivision number is, the more the grid blocks are used. However, all those Triple-Porosity Models use much lower grid numbers to characterize the model.

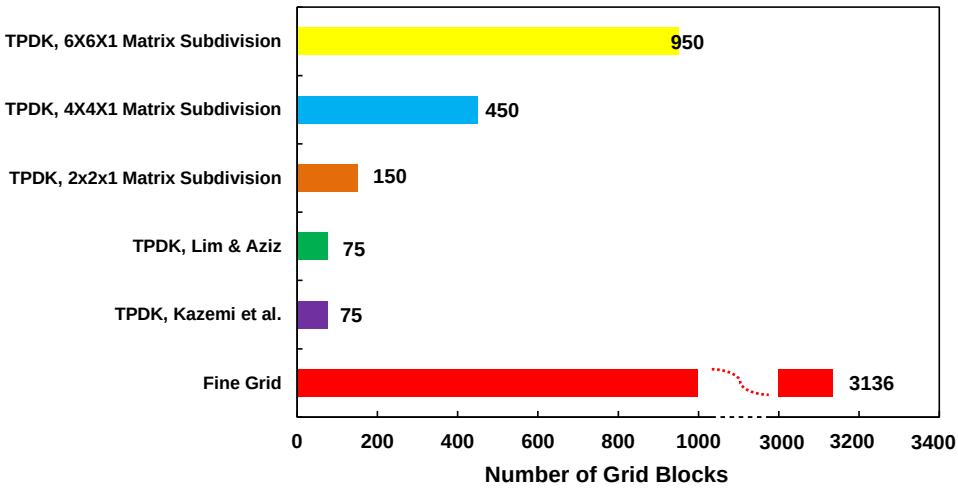

Fig. 3.10—Comparison of grid numbers between Triple-Porosity Dual-Permeability (TPDK) Models and Fine-Grid Single-Porosity Model.

Correspondingly the CPU time for each models is also plotted in **Fig. 3.11**. The results show that the CPU cost for those Triple-Porosity Dual-Permeability Models is much cheaper than Fine-Grid Single-Porosity Model, since those models have fewer grid blocks. In the reservoir matrix blocks are isolated by fracture sets, and thus flow between matrix blocks is not allowed in the Triple-Porosity Dual-Permeability Models. This further reasonably reduces the complexity of connectivity in the reservoir, and make those Triple Porosity Models run more efficiently. Therefore, even though TPDK model with $6 \times 6 \times 1$ matrix subdivision (950) have around $1/3$ of the number of grid blocks in the Fine-Grid Single-Porosity Model (3136), while the CPU time for the former model (38.7 sec) is around 1/25 of the CPU time for the latter model (964.5 sec) and the results of those two are matched well (**Fig. 3.8**). Besides, we can observe that CPU cost increases with matrix

subdivision in **Fig. 3.11**, and it has similar trend to the number of grid blocks used in those models (**Fig. 3.10**).

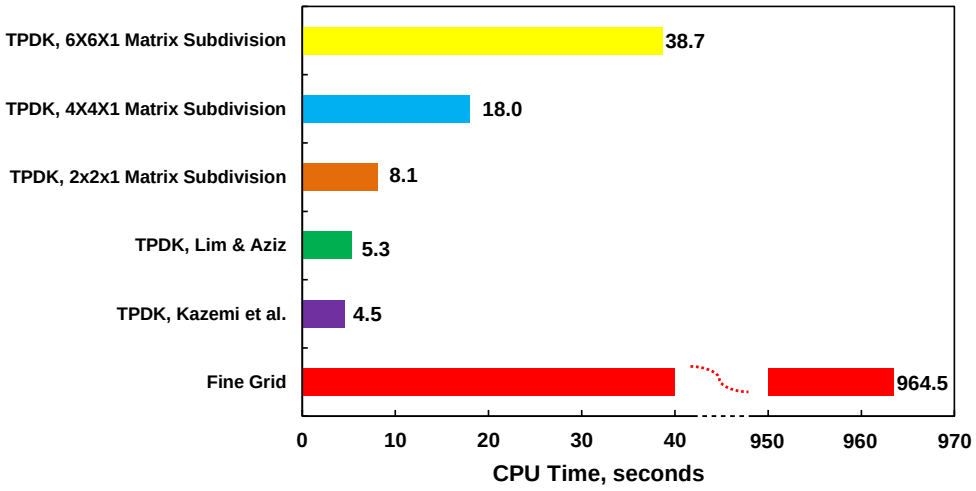

Fig. 3.11—Comparison of CPU time between Triple-Porosity Dual-Permeability (TPDK) Models and Fine-Grid Single-Porosity Model

3.3 Two Phase Flow in a Shale Gas Reservoir

After the Multi-Porosity Model is benchmarked in the single phase scenario, it is applied into a two-phase (gas/water) shale gas reservoir. The shale gas reservoir is separated into four different porosity types, including hydraulic fracture (HF), natural fracture (NF), inorganic matrix (IM) and organic matrix (OM). Besides, each porosity system is allowed to communicate with each other. Hydraulic fracture serves a constant pressure and constant saturation boundary condition for the reservoir. Therefore, it is actually a Quad-Porosity Quad-Permeability (QPQK) Model. In the model, inorganic matrix is considered to be water wet, and organic matter is considered to be gas wet. Linear

relative permeability curves and no capillary pressures are considered in the two fracture systems, and Corey's correlations of capillary pressure and relative permeability curves are applied into the two matrix systems. **Fig. 3.12** shows the capillary pressure curve used for the simulation, and **Fig. 3.13** shows the imbibition relative permeability curve implemented in the simulator.

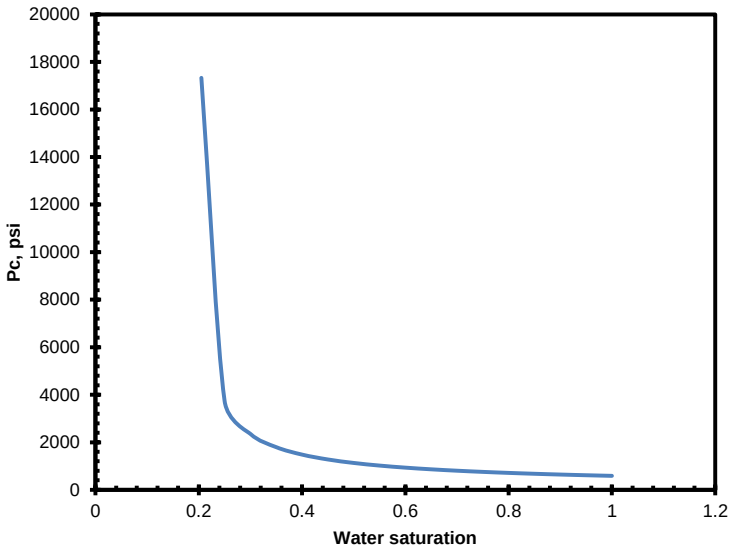

Fig. 3.12—Capillary pressure in the shale model

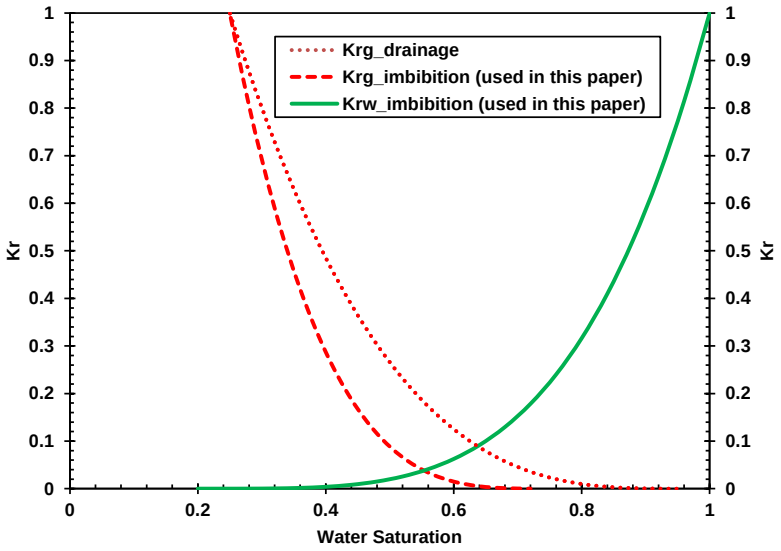

Fig 3.13—Relative permeability curve in the shale model

Other input parameters during the simulation are presented in the **Table 3.3** and **Table 3.4**.

Table 3.3—Data for quad-porosity model for each porosity

	HF	NF	IM	OM
$k_f w_f$ $(mD \cdot ft)$	100	5	-	-
k (nD)	-	-	100	50
ϕ (v/v)	1e-4	3e-5	0.06	0.30
Pressure $(psia)$	500 (constant)	3000	3000	3000
Initial S_g (v/v)	0.1	0.7	0.7	0.99
T (°F)		180 (constant)		
Wetting phase	Aqueous	Aqueous	Aqueous	Organic

Table 3.4—Reservoir geometry parameter for quad-porosity model

Reservoir size (ft)	3100 by 1500 by 50
Horizontal well length (ft)	1300
Spacing of hydraulic fracture (ft)	100
Half-length of hydraulic fractures (ft)	200
Thickness of hydraulic fracture (ft)	50
Number of hydraulic fractures	6
Grid size	100 ft by 100 ft by 50
Scheme I	No matrix subdivision
Scheme II	5 by 5 by 1 matrix subdivision

As shown in **Fig. 3.14**, two different QPQK Models are applied to simulate the reservoir: (1) Scheme I: Quad-Porosity Model without porosity subdivision in inorganic and organic matrix; (2) Scheme II: Quad-Porosity Model with porosity subdivision in inorganic and organic matrix. In **Fig. 3.14 (a)** and **(b)**, the red part in hydraulic fracture porosity is to represent both hydraulic fracture and horizontal wellbore. In **Fig. 3.14(b)**, the matrix blocks in Scheme II is subdivided into 5 by 5 by 1 cells in $x - y - z$ space.

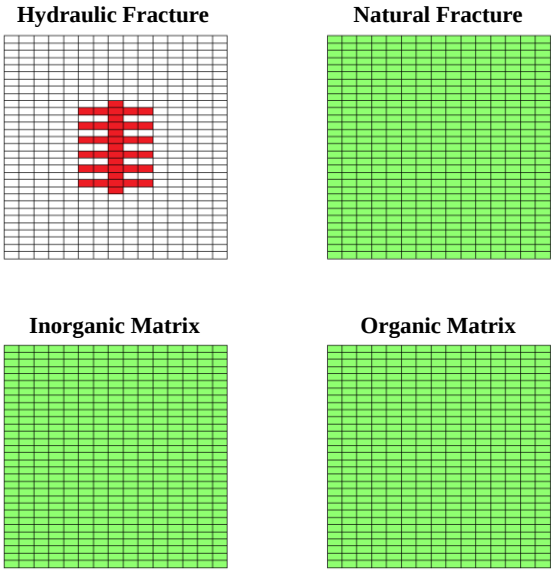

(a)

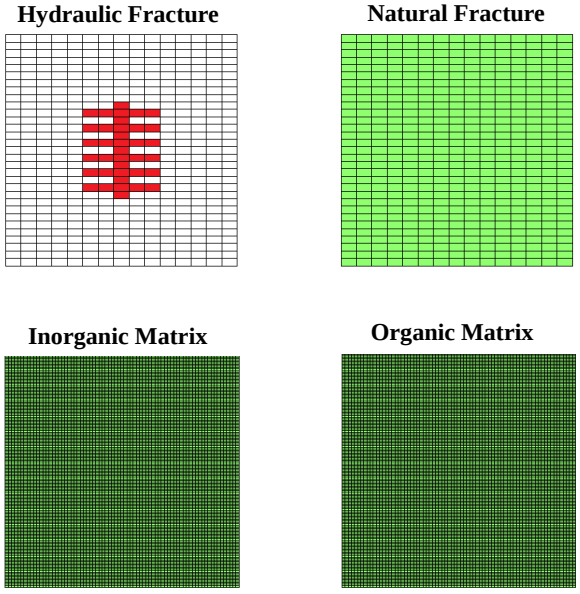

(b)

Fig. 3.14—Two different schemes to discretize the quad-porosity reservoir model: (a) Scheme I: Quad-Porosity Model without matrix subdivision; (b) Scheme II: Quad-Porosity Model with subdivision in inorganic and organic matrix.

Through running both models, the average pressure in each porosity system is shown in **Fig. 3.15**. Considering Scheme II as the calibrated results, the pressure difference between the two schemes are acceptable, as shown in **Fig. 3.15**. Besides, in **Fig. 3.15**, during production the pressure in the reservoir changes in sequence: natural fracture first, followed by inorganic matrix, and ultimately organic matrix. The sequence is consistent with the order of permeability in the three porosity systems. This is further validated by the pressure map of both models after 20 years gas production, as shown in **Fig. 3.16**. Besides, due to the coarse gridding in the two matrix domains, Scheme I cannot capture the transient flow with high resolution, but Scheme II improves the resolution through the grid refinement in the matrix domain.

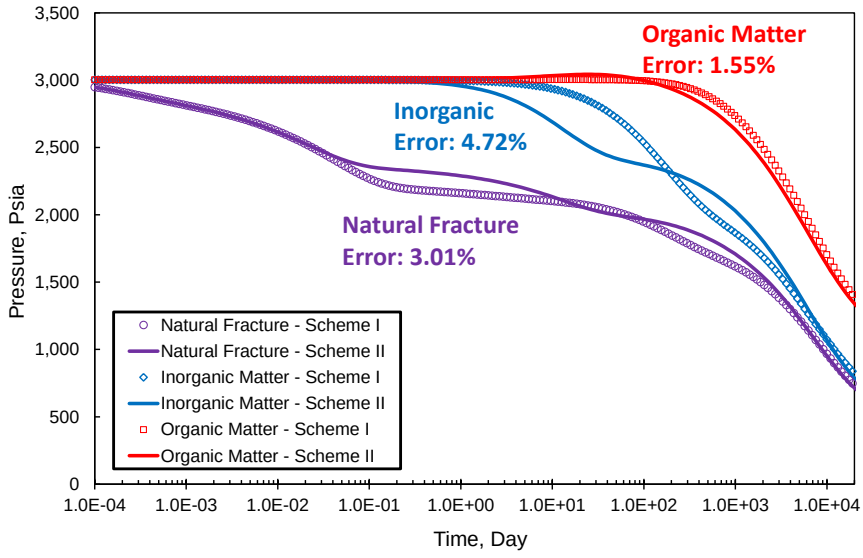

Fig. 3.15—Average pressure in each porosity system for Scheme I and II.

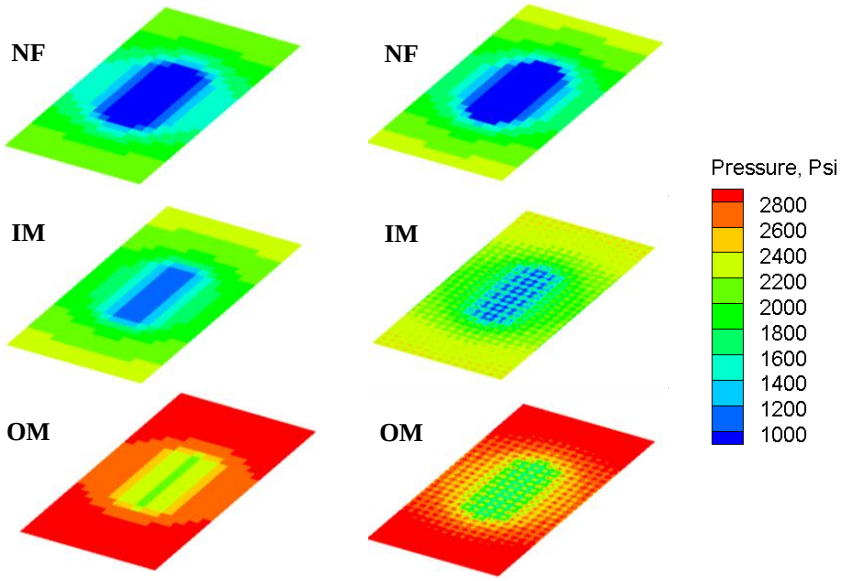

Fig. 3.16—Pressure map after 20 years production: left column – Scheme I; right column – Scheme II.

The average water saturation in each porosity system is shown in **Fig. 3.17**. In this plot, it shows that water saturation in natural fracture system decreases at an early period, and ultimately remains at negligible water saturation. At early period, natural fracture system is the upstream of both water and gas flow. Since the water mobility between inorganic matrix and natural fracture is much lower than that between natural fracture and hydraulic fracture, most of the water in natural fracture flows into hydraulic fracture and wellbore, and ultimately water saturation in natural fracture becomes negligible. At the later production period, water is imbibed from hydraulic fracture system to inorganic matter because of the boundary condition. Organic matrix is assumed to non-water wet, and the initial water saturation there is extremely low at 0.01. Therefore, during the whole

production period, single gas phase flow occurs in the organic matrix. The difference of average water saturation between those two different schemes are still quite good here.

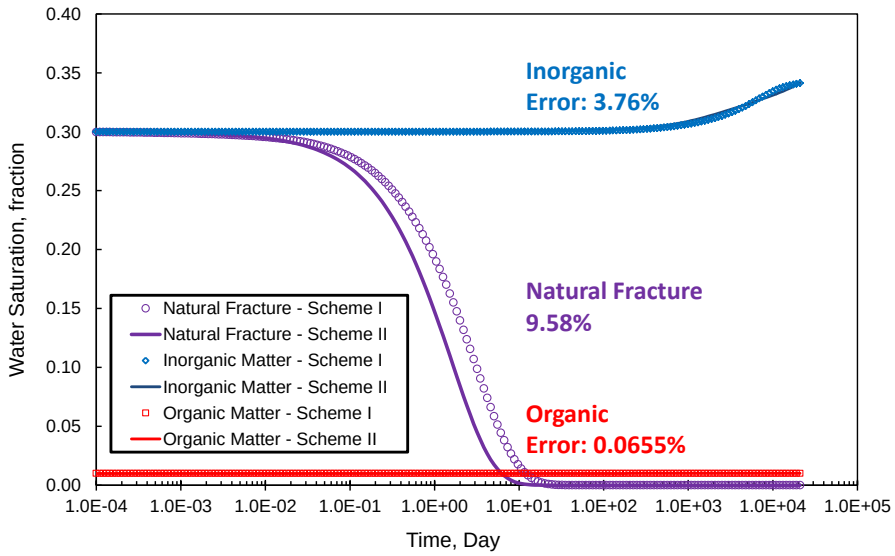

Fig. 3.17—Average water saturation in each porosity types in Scheme I and II

Ultimately, the gas production for both schemes are shown in **Fig. 3.18**. Consistent results are still obtained, and the difference is caused by their different capabilities to capture the transient flow between matrix and fracture.

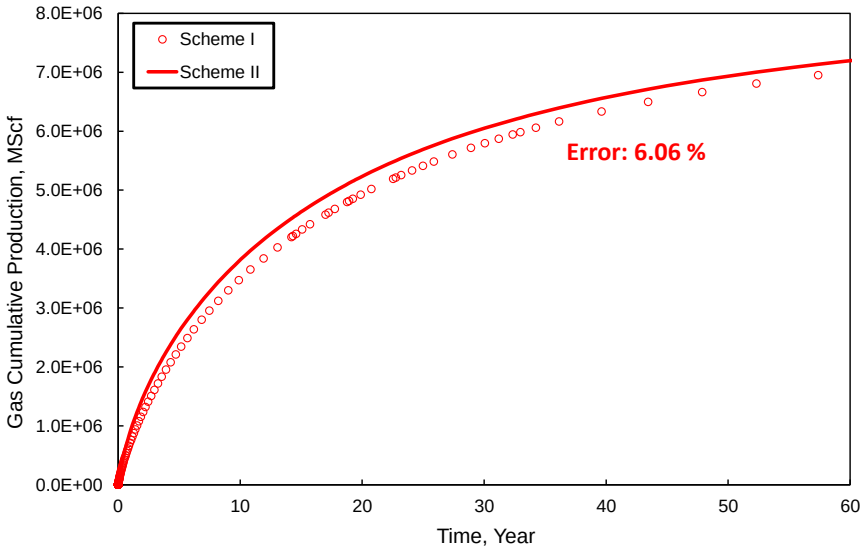

Fig. 3.18—Gas production in Scheme I and II

3.4 Summary

In this chapter, it is demonstrated that the results of Dual-Porosity Models with Lim and Aziz's shape factor are in good consistency with Fine-Grid Single-Porosity Models for most of the time scale, but the Dual-Porosity Models with shape factor of Kazemi et al. underestimates the solution. This is very consistent with the results from literature (Lim and Aziz 1995), and it directly proves the robustness of the implementation in this work.

However, those conventional Dual-Porosity Model fails to accurately characterize the transient flow between matrix and fracture at early production period. With the application of porosity (matrix) subdivision in Multi-Porosity Models, the examples of Dual-Porosity Models and Triple-Porosity Models demonstrate that Multi-Porosity Model with Subdivision successfully enhances the accuracy of transient flow at early production

period, since the decomposed porosity sub-blocks can characterize the nonlinear fluid transfer between different porosity systems very well. Besides, the performance of Multi-Porosity Model is also improved compared to the Fine-Grid Single-Porosity Model.

Finally, Quad-Porosity Quad-Permeability Models with and without matrix subdivision are successfully applied into two-phase shale gas reservoir, and they provide consistent results, and the model with matrix subdivision brings higher resolution in the matrix domains.

CHAPTER IV

GENERAL UNSTRUCTURED RESERVOIR UTILITY

Numerical reservoir simulation is one of the most important approaches to investigate multiphase fluid flow transport through porous media. The framework of reservoir simulators is based on numerical solutions of material balance, energy balance and stress equilibrium equations, and ultimately mimics the complex fluid flow behavior in subsurface reservoirs. This chapter illustrates the workflow of a fully implicit unstructured compositional reservoir simulator. The simulator developed in this chapter is called **G**eneral **U**nstructured **R**eservoir **U**tility (**GURU**).

4.1 Model Assumption

GURU is designed to be general, and its framework is developed based on the following assumptions,

- Control-Volume Finite-Difference space discretization;
- Backward first order fully implicit time discretization;
- Isothermal condition in the subsurface system;
- Two-point flux approximation;
- Fluid flux is dominated by Darcy flow;
- Knudsen diffusion and gas slippage flow also contributes to gas flux;
- Gas can be stored by adsorption;

- Oil and gas fluid properties are calculated through vapor-liquid equilibrium based on Equation of State;
- Water is inertial and not involved in thermodynamic equilibrium of hydrocarbon components;
- Multiple fluid systems such as oil/water, oil/gas/water and gas/water are allowed;
- Capillary pressure and gravity are considered.

The compositional reservoir simulator is implemented based on control-volume finite-difference method (CVFD) (Cao 2002) with two-point flux approximation (TPFA). This approach records grid discretization by grid and connection information, as shown in **Fig. 4.1**. It tracks grid discretization via two classes: "Cell" stores grid-based static properties including geometric information and rock and fluid properties; "Connection" mainly contains flux related properties for connected grid blocks. Therefore, even with complex grid geometry conforming geological features, this approach enables to accept unstructured grid discretization without barriers.

```
TYPE Cell
   INTEGER :: ID
   INTEGER :: RockType
   DOUBLE :: PoreVolume
   ….
END TYPE
```

```
TYPE Connection
   INTEGER :: ID
   INTEGER :: cell_A
   INTEGER :: cell_B
   DOUBLE :: Transmissibility
    …
END TYPE
```

Fig. 4.1—Unstructured data format defined by FORTRAN syntax

4.2 Primary Mathematical Formulation

Based on the primarily solved equations in compositional simulation, there mainly exist two types of formulation, respectively mass balance type and volume balance type (Cao 2002; Valbuena 2015). Primary equations in mass balance type are represented by the mass balance equations for each species in the reservoir fluids (Chien et al. 1985; Coats 1980; Collins et al. 1992; Fussell and Yanosik 1979; Young and Stephenson 1983), and this type of formulation can be solved by either Fully Implicit Method (FIM) or IMplicit Pressure Explicit Saturation (IMPES). On the other hand, the concept of volume balance was introduced to ensure that the pore volume must be completely occupied by the total fluid volume in a grid block, and based on this the volume balance equation is transformed into the pressure equation (Acs et al. 1985; Wong et al. 1990), and it is usually solved by IMplicit Pressure Explicit Mass (IMPEM).

Further, there are two types of primary variables to solve, respectively natural variables (Coats 1980) or overall quantities (Young and Stephenson 1983). Natural variables are convenient in terms of Jacobian matrix derivation, but yet it requires to switch primary variables when phase appearance/disappearance occurs. On the contrary, when overall qualities are used as the primary variables, it is necessary to use chain rule to construct Jacobian system, but there is no need to switch primary variables as phase changes. In GURU Jacobian is constructed by numerical perturbation for the convenience of implementation, and overall qualities are selected as primary variables to construct the global linear system inside GURU. As a result, a modified Young and Stephenson (1983) compositional formulation is adopted in GURU, showing in the Section 4.2.1.

4.2.1 Mass Balance Equations

In this section, the mass balance equations related hydrocarbon component and water are presented. As stated in the assumptions presented in Section 4.1, water is assumed to be inertial and the dissolved water in oil and gas phases and the dissolution of hydrocarbon components in aqueous phase are ignored. If a cell j is arbitrarily connected with another cell via grid surface s, the mass balance equation associated with the hydrocarbon component i ($i = 1, \cdots, n_h$) in cell j is presented in Equation (4.1).

$$R_{i,j} = \frac{V_j}{\Delta t}\left(N_{i,j}^{n+1} - N_{i,j}^{n}\right) + \frac{V_j}{\Delta t}\left(M_{i,j}^{n+1} - M_{i,j}^{n}\right) - \sum_s T_s\left(\lambda_o \tilde{\rho}_o x_i \Delta\Phi_o + \lambda_g \tilde{\rho}_g y_i \Delta\Phi_g\right) - \sum_p\left(\tilde{\rho}_o x_i q_o^p + \tilde{\rho}_g y_i q_g^p\right)_j = 0 \quad (4.1)$$

In Equation (4.1), the first term is the accumulation of hydrocarbon component i in compressed storage, and N_i is defined in Equation (4.2), which represents the moles of hydrocarbon component i stored in compressed status in unit cell volume. The second term is the accumulation of hydrocarbon component i by adsorption, and M_i is defined in Equation (4.3), which represents the moles of hydrocarbon component i stored by adsorption in unit cell volume. The multi-component gas adsorption/desorption formulation in Equation (4.3) is defined based on general extended Langmuir model (Cao et al. 2015). The third term in Equation (4.1) is the Darcian flux term here, and the forth term is the source or sink term.

$$N_i = \phi(s_o \tilde{\rho}_o x_i + s_g \tilde{\rho}_g y_i) \quad (4.2)$$

$$M_i = (1-\phi)\rho_s \tilde{\rho}_g^{sc} \frac{V_{L,i} y_i \frac{p_g}{p_{L,i}}}{1 + \sum_{k=1}^{n_h} y_k \frac{p_g}{p_{L,k}}} \quad (4.3)$$

Similarly, the mass balance equation of water component in cell *j* is defined in Equation (4.4). Here water phase flux obeys Darcy's law, and water component exists in compressed state in pore space, as shown in Equation (4.5).

$$R_{w,j} = \frac{V_j}{\Delta t}\left(N_{w,j}^{n+1} - N_{w,j}^{n}\right) - \sum_s T_s \lambda_w \tilde{\rho}_w \Delta\Phi_w - \sum_p \left(\tilde{\rho}_w q_w^p\right)_j = 0 \tag{4.4}$$

$$N_w = \phi s_w \tilde{\rho}_w \tag{4.5}$$

In Equations (4.1) and (4.4), T_s is defined as transmissibility in connection via grid surface s, and it is a geometric coefficient to evaluate the connectivity between two cells. The inter-cell transmissibility is calculated by harmonic average (Equation (4.6)). The half–cell transmissibility for neighbor connection is defined in Equation (4.7).

$$T_s = \frac{T_{s,j} T_{s,j+1}}{T_{s,j} + T_{s,j+1}} \tag{4.6}$$

$$T_{s,j} = \frac{k_j A_j}{L_j} \tag{4.7}$$

λ_α $(\alpha = o, w, g)$ is the fluid mobility related to each phase in Darcian flux calculation, and it is defined in Equation (4.8). Fluid mobility, molar density and mole fraction in the flux terms of those mass balance equations are evaluated by upstream weighting based on the direction of phase potential difference.

$$\lambda_\alpha = \frac{k_{r\alpha}}{\mu_\alpha} \tag{4.8}$$

Phase potential Φ_α considers both phase pressure p_α and gravitational force on the fluid, which is defined by Equation (4.9). Therefore, to calculate Darcian flux at

connection s, the potential gradients in Equation (4.1) and (4.4) are evaluated in split form, as shown in Equation (4.10). The calculation of phase pressures will be discussed in the auxiliary formulation part.

$$\Phi_\alpha = p_\alpha - g_c \rho_\alpha D \tag{4.9}$$

$$\Delta\Phi_\alpha = \Delta p_\alpha - g_c \rho_{\alpha,s} \Delta D \tag{4.10}$$

Inter-phase transport problem in the vertical direction occurs when there are phase discontinuities in two vertically connected cells, and this might lead to numerical instability during compositional simulation. To solve this problem the inter-cell phase average mass density is weighted by phase saturation but not based on arithmetic average (Bowen and Crumpton 2003), as shown in Equation (4.11).

$$\rho_{\alpha,s} = \frac{S_{\alpha,j}\rho_{\alpha,j} + S_{\alpha,j+1}\rho_{\alpha,j+1}}{S_{\alpha,j} + S_{\alpha,j+1}} \tag{4.11}$$

Besides, if cell j is perforated by an active well, a source or sink will be taken into account in mass balance equations of the cell, and the phase volumetric production rate at the local perforation p is calculated based on Peaceman Equation (Peaceman 1990). Assume there is a perforation p in cell j, then the volumetric rate of phase α becomes,

$$q_\alpha^p = WI_p \cdot \lambda_{\alpha,p}\left(p_p - p_{\alpha,j}\right), \tag{4.12}$$

where WI_p is the well geometric index for perforation p in a well, and $\lambda_{\alpha,p}$ is the well mobility at perforation p, and p_p and $p_{\alpha,j}$ are respectively the wellbore pressure at the perforation p and the phase pressure in perforated cell j.

In GURU the well geometric index is a flexible user-defined input, and it can be calculated based on geometric parameters of wellbore and perforated cell. If a rectangular grid block is perforated by a vertical well, WI_p is calculated by Equation (4.13). In the scenario of horizontal wells, WI_p can still be obtained by updating corresponding spatial variables in Equations (4.13) and (4.14).

$$WI_p = 2\pi \frac{\Delta z \sqrt{k_x k_y}}{ln\left(\frac{r_o}{r_w}\right)+S} \tag{4.13}$$

$$r_o = 0.28 \frac{\left(\Delta x^2 \sqrt{k_y/k_x}+\Delta y^2 \sqrt{k_x/k_y}\right)^{1/2}}{\sqrt[4]{k_y/k_x}+\sqrt[4]{k_x/k_y}} \tag{4.14}$$

If the perforation p belongs to a producer, the well mobility at the perforation is upstreamed and equals to fluid mobility in the perforated cell j, but special consideration should be taken into with regards to the well mobility in an injector, which equals to the total fluid mobility in the perforated cell (Valbuena 2015). Therefore, the well mobility is summarized in Equation (4.15),

$$\lambda_{\alpha,p} = \begin{cases} = \left(\frac{k_{r\alpha}}{\mu_\alpha}\right)_j & (p \in producer) \\ = \sum_{\alpha=o,g,w} \left(\frac{k_{r\alpha}}{\mu_\alpha}\right)_j & (p \in injector) \end{cases} \tag{4.15}$$

4.2.2 Volume Balance Equation

In GURU it is assumed there are at most three phases (water, oil and gas) in a reservoir system, so there exists a volume balance equation with regards to total fluid volume (excluding adsorption) and pore space volume. The constraint ensures that the total fluid volume of all phases in cell *j* equals to its pore volume, and it is defined as Equation (4.16),

$$R_{vol,j} = PV_j - \sum_{\alpha=o,g,w} V_{\alpha,j} = 0 \tag{4.16}$$

Equation (4.16) also serves as one of the primary reservoir equations. Phase volumes are functions of phase moles and phase molar densities, and phase saturations can be calculated based on phase volumes and total pore volume. Further, saturations is applied to calculate capillary pressure and relative permeability (rock-fluid function).

4.2.3 Well Residual Equation

There exist multiple well controls, including constant rate, constant bottom-hole pressure or their combinations. Well residuals are also involved as part of the primary equations, and they are also solved by fully implicit method (Fung et al. 2005). In GURU, five different well residuals are implemented, including constant bottom-hole pressure (Equation (4.17)), constant oil surface volume rate (Equation (4.18)), constant gas surface volume rate (Equation (4.19)), constant liquid (oil and water) surface volume rate (Equation (4.20)), and constant water surface volume rate (Equation (4.21)).

$$R_{well} = p_{wf} - p_{wf}^{*} = 0 \tag{4.17}$$

$$R_{well} = \frac{(\tilde{Q}_o + \tilde{Q}_g) f_l^{sc}}{\tilde{\rho}_o^{sc}} - Q_{V,o}^* = 0 \tag{4.18}$$

$$R_{well} = \frac{(\tilde{Q}_o + \tilde{Q}_g) f_v^{sc}}{\tilde{\rho}_g^{sc}} - Q_{V,g}^* = 0 \tag{4.19}$$

$$R_{well} = \frac{(\tilde{Q}_o + \tilde{Q}_g) f_l^{sc}}{\tilde{\rho}_o^{sc}} + \frac{\tilde{Q}_w}{\tilde{\rho}_w^{sc}} - Q_{V,ow}^* = 0 \tag{4.20}$$

$$R_{well} = \frac{\tilde{Q}_w}{\tilde{\rho}_w^{sc}} - Q_{V,w}^* = 0 \tag{4.21}$$

All of those five well residuals are applicable to producer wells. For example, if a producer is controlled by a combined schedule of constant surface oil volume rate and a minimum BHP, then the primary equation will be either Equation (4.17) or (4.18). If the current reservoir condition can maintain a constant surface oil volume rate, the well residual becomes Equation (4.18); otherwise, it will turn to Equation (4.17). As for injectors, Equations (4.17) and Equation (4.19) are used in gas injectors, and Equations (4.17) and (4.21) are applied in water injectors. Combined schedules are also applicable for injectors, and its selection criteria is identical to that in producer. Besides, any of those controls related to hydrocarbon components requires surface flash calculation to convert hydrocarbon component moles to volumetric qualities in surface condition.

4.3 Auxiliary Equations

The primary equations in Section 4.2 serves as the basic structure of the global primary equation system, yet auxiliary equations provide additional constraints to close the system. As a result, in this section several important auxiliary equations used in the

multiphase compositional simulation are discussed, including equation of state, vapor-liquid equilibrium, fluid properties, rock-fluid functions and rock properties.

4.3.1 Equation of State

In GURU hydrocarbon properties are calculated based on the Peng-Robinson Equation of State (PR-EOS) (Peng and Robinson 1976), and it is applied in terms of cubic equation to get the analytical solution of the compressibility factor Z. The detailed formulation about PR-EOS can be referred to **Appendix A**.

$$Z^3 - (1 - B)Z^2 + (A - 3B^2 - 2B)Z - (AB - B^2 - B^3) = 0 \quad (4.22)$$

The EOS can be directly used to calculate fluid properties and fugacity coefficient for each component in a specific phase, shown as Equation (4.23). The fugacity coefficients and their derivatives to pressure and phase compositions can also be analytically solved from the Equation of State, which can be referred to Appendix C in (Cao 2002). Those results further provide input for Vapor-Liquid Equilibrium calculation.

$$ln\varphi_i = -\ln(Z - B) + (Z - 1)\frac{b_i}{b} - \frac{A}{2\sqrt{2}B}\left[\frac{1}{a}\left(2\sqrt{a_i}\sum_{j=1}^{n_h} x_j\sqrt{a_j}(1 - \kappa_{ij})\right) - \frac{b_i}{b}\right] ln\left(\frac{Z+(1+\sqrt{2})B}{Z+(1-\sqrt{2})B}\right) \quad (4.23)$$

4.3.2 Vapor-Liquid Equilibrium

Vapor-liquid equilibrium (VLE) is used to calculate oil and gas fluid properties. Given bulk fluid compositions z_i, pressure p and temperature T, fluid thermodynamic

properties can be determined by VLE. Therefore, in GURU this procedure is decoupled from the primary equation system, and this favors to reduce the dimension of the Jacobian system in reservoir simulation and allows flexible interface with EOS and VLE calculation from a third party. When primary or secondary variables are updated at time or newton level, VLE calculation becomes necessary.

4.3.2.1 VLE Residuals

Two residuals are solved in the VLE calculation, including component phase fugacity equilibrium and molar vapor fraction equilibrium. The first residual is fugacity equilibrium. In two-phase flash calculation, the component fugacity equilibrium is shown as the following,

$$R_{f,i} = lnK_i + ln\varphi_i^v - ln\varphi_i^l = 0, \qquad i = 1, \cdots, n_h \tag{4.24}$$

The second residual is a component and phase material-balance constraint, called the Rachford-Rice Equation (Rachford and Rice 1952). This function is monotonic and continuous, shown as Equation (4.25),

$$R_r = \sum_{i=1}^{n_h}(y_i - x_i) = \sum_{i=1}^{n_h} \frac{z_i(K_i-1)}{1+f_v(K_i-1)} = 0 \tag{4.25}$$

The Equations (4.24) and (4.25) together solve the phase component equilibrium ratio K_i and the vapor mole fraction f_v. Those two equations are usually solved through combining Successive Substitution Iteration method (SSI) and Newton-Raphson method (NR) (Firoozabadi 1999; Li and Firoozabadi 2012; Whitson and Brule 2000). Equation

(4.24) is highly nonlinear since K_i changes nonlinearly with pressure, temperature and compositions. The details of SSI and NR method for VLE calculation can be referred to **Appendix B** in this work.

Initial guesses of K_i and vapor mole fraction f_v with good quality can speed up the convergence of VLE calculation and avoid the trivial solution. If no additional data is available, Wilson's correlation (Wilson 1968) is usually used to estimate K_i as shown in Equation (4.26). However, estimation based on this correlation is not accurate at high pressure conditions and leads to the trivial solution. On the other hand, it is numerically reliable to estimate K_i from a converged flash of the same fluid or fluid with close compositions at similar pressure and temperature conditions (Whitson and Brule 2000). For example, K_i from similar conditions such as those from the previous time step, previous newton step, or neighboring non-perforated grid blocks can provide initial guesses for equilibrium ratios and phase mole fractions. Further, if the quality of those values are not ensured, traditionally it turns to stability testing for K_i values with lowest tangent plane distance values (Li and Firoozabadi 2012). However, the stability test is usually quite expensive in computation and is not always necessary if the current thermodynamic condition is far away from the saturation point.

$$lnK_i = ln\frac{p_{ci}}{p} + 5.373(1+\omega_i)\left(1-\frac{T_{ci}}{T}\right) \tag{4.26}$$

4.3.2.2 VLE Preconditioned by Compositional Space

To avoid quality check of estimation based on similar thermodynamic conditions and unnecessary stability testing, methods for safeguard estimation of K_i values and vapor

mole fraction f_v are proposed and discussed in the following two sections. Fluids in compositional simulation can be classified into two categories: fluids with slight composition changes or fixed composition and fluids with sharply varying composition. The first scenario is applicable to the depletion processes from conventional reservoirs, except for gas-condensate reservoirs and volatile-oil reservoirs. The second scenario usually occurs in miscible flooding processes of gas injection and depletion processes of gas-condensate or volatile oil reservoirs. Based on the characteristics of those two scenarios, two different compositional spaces are constructed prior to the flash calculation. Using single variable or multiple variables interpolation from the compositional spaces, good initial guesses of K_i values and vapor mole fractions f_v can be achieved. The compositional space based on slightly varying or constant composition has already been successfully implemented in GURU.

4.3.2.2.1 Fluids with Slightly Varying or Constant Composition

When fluid composition is fixed or slightly changes, it is reasonable to assume that the equilibrium ratios K_i and vapor mole fraction f_v are only a function of pressure and temperature. The degree of freedom further reduces to pressure only in isothermal condition. As an example, a petroleum fluid with 11 components from Maljamar Reservoir Oil at 89.96 °F from Li and Firoozabadi (2012) is used. Its CO_2 fraction is 0.1667 and other compositions are normalized based on the number of moles from the original data. The bubble point pressure is calculated to be $p_b = 1576.1874\,psia$ at 89.96 °F. Reducing the pressure from p_b to around $50\,psia$ (lower end), the changes of f_v and K_i is

shown in **Fig. 4.2** and **4.3**. As pressure decreases from p_b to $50\ psia$, the vapor mole fraction gradually increases from 0.0 to 0.5573 (**Figure 4.2**). In addition, **Figure 4.3** shows that the component equilibrium ratios K_i change significantly and even cover orders of magnitude for some (pseudo) components, such as C_{21-28} and C_{29+}.

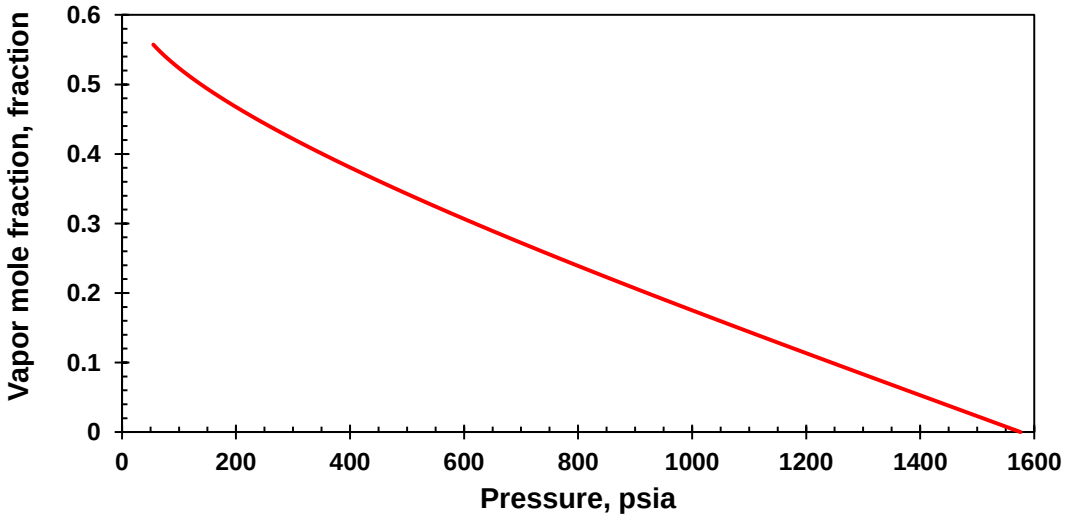

Fig. 4.2—Vapor mole fraction of Maljamar Reservoir Oil at 89.96 °F, CO_2 fraction is 0.1667

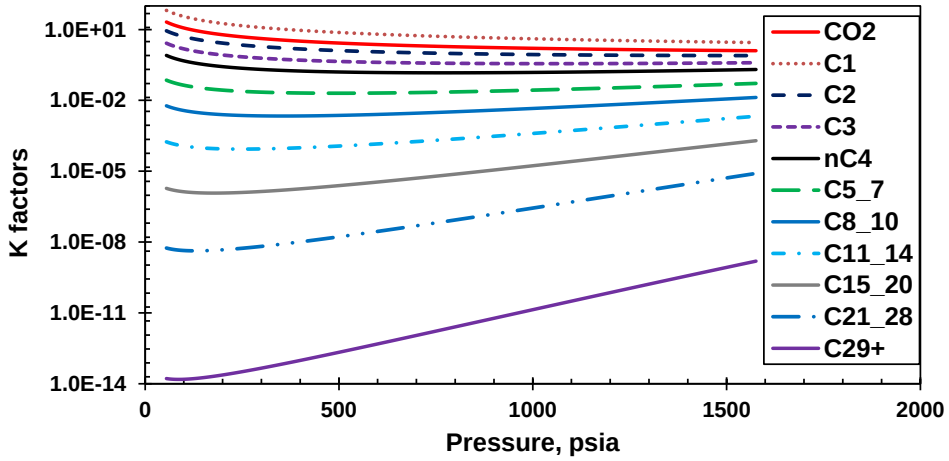

Fig. 4.3—Component K-values of Maljamar Reservoir Oil at 89.96 °F, CO_2 fraction is 0.1667

The curves in **Fig. 4.2** and **4.3** actually define a discrete compositional space for isothermal constant composition fluid. As a result, the initial guesses of f_v and K_i at an arbitrary pressure can be interpolated from this space as long as the pressure falls into the pressure range defined in the space. A correct root-searching direction is thus ensured to efficiently converge the flash calculation. Since f_v and K_i become trivial at pressure out of its range in **Fig. 4.2** and **4.3**, the requirement to conduct interpolation is unconditionally satisfied.

Essentially, in the compositional space the independent variable is pressure and the dependent variables are equilibrium ratios K_i and vapor mole fraction f_v, as shown in Equations (4.27) and (4.28). Assume that saturation pressure and the corresponding equilibrium ratios K_i are given, a pressure vector is constructed by reducing pressure from saturation pressure to a very low end pressure. Flash calculation at different pressures can

then be efficiently performed following the pressure decreasing direction, since the first initial guess after saturation pressure can be adopted from values at saturation pressure condition.

$$K_i = g_1(p) \tag{4.27}$$

$$f_v = g_2(p) \tag{4.28}$$

The basic VLE procedure for fixed composition scenario is provided in **Fig. 4.4**. Step 1 is a static procedure, where a 2D compositional space defining $P - K_i$ and $P - f_v$ relationships is constructed. This compositional space or database can be established before the dynamic simulation or outside of the simulator kernel, for example at the initialization step. The regular dynamic flash procedure starts from Step 2 to 4 in the red dash rectangular box. Even though the interpolated vapor mole fraction f_v may not exactly results in the convergence of Rachford-Rice (RR) Equation, it will be definitely improved after the first SSI iteration. Alternatively, a preconditioning procedure to improve f_v can be done through evaluation of RR equation based on the initial estimates. Therefore, those two alternative options are provided in Step 3.

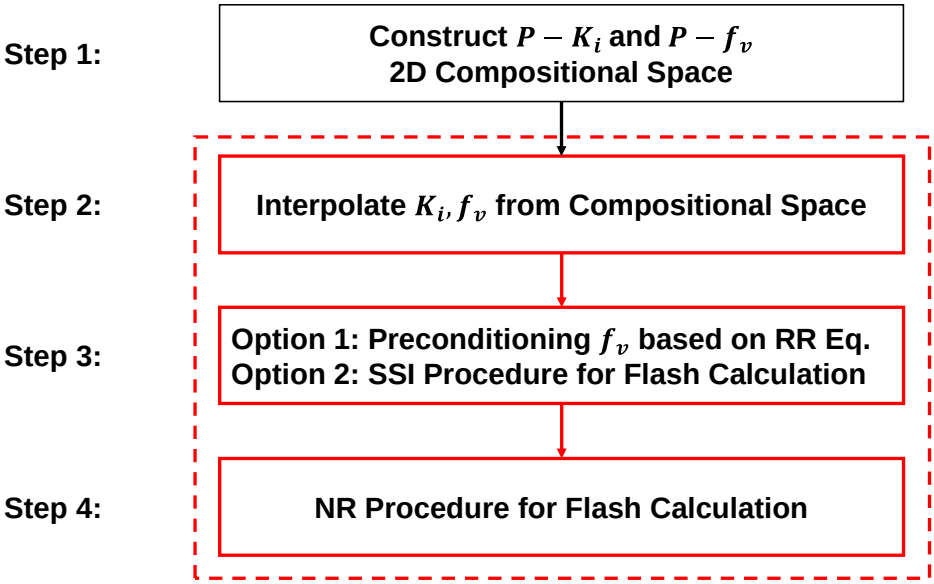

Fig. 4.4—Workflow of VLE procedure for fixed fluid compositions

4.3.2.2.2 Fluids with Sharply Varying Composition

The approach proposed above is appropriate to predict phase behavior of petroleum fluid with a fixed composition. However, fluid composition is generally variable in many cases such as gas flooding processes. Take the petroleum fluid with 7 components from North Ward Estes oil at 82.99 °F as an example (Li and Firoozabadi 2012). CO_2 is considered as the injected component and other compositions are normalized based on the number of moles from the original data. VLE is performed with CO_2 mole fraction changing from 0.01 to 0.8. The corresponding phase diagram is shown in **Fig. 4.5**. Clearly the bubble point pressure increases with the increase of CO_2 mole fraction. When CO_2 mole fraction is higher than 0.55, the bubble point pressure increases significantly. In the original data there is a small region of three phase, but it is not shown in two phase diagram here. However, this never hinders the investigation purpose here.

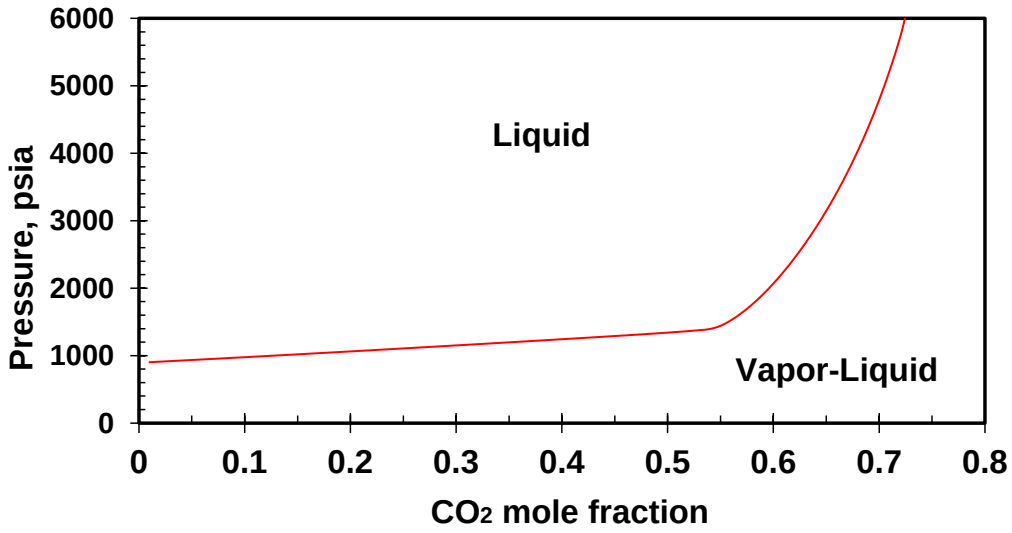

Fig. 4.5—Phase diagram of North Ward Estes oil at 82.99 °F with different CO_2 mole fraction

Following the path of bubble point line in **Fig. 4.5**, the equilibrium ratios K_i for the 7 components versus CO_2 mole fraction are plotted in **Fig. 4.6**. It shows that K_i of all components ultimately converges to values very close to 1, which is actually near the critical condition. The K_i changes for components PC_4 and PC_5 are respectively in the magnitude of 10^6 and 10^{11} as CO_2 mole fraction increases from 0.01 to 0.8. The high nonlinearity presented in this varied composition scenario makes those conventional K_i estimation methods inaccurate. Since the basic assumption of constant composition is not valid anymore, initial guess from the proposed approach in the previous section cannot favorably speed up the flash calculation convergence.

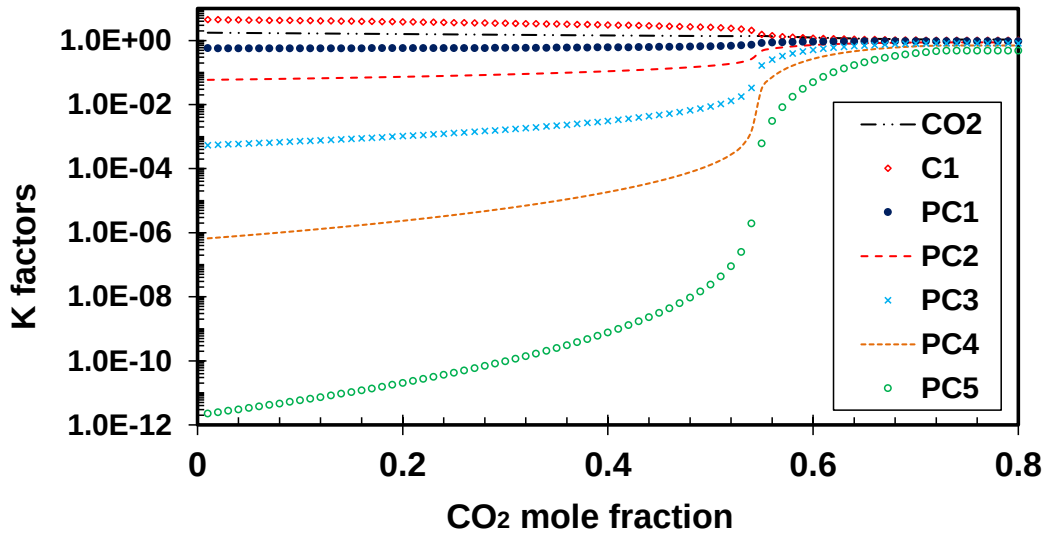

Fig. 4.6—K-values of North Ward Estes oil at 82. 99 °F following the bubble point line in Fig. 4.5

As the mole fractions of the injected components continuously increase and are ultimately mixed with original petroleum fluid, the composition changes sharply. In addition to pressure, compositional dynamics change the PVT behavior correspondingly. Therefore, it is reasonable to define those components causing changes as a pseudo key component (hereafter referred as "PKC"), which provides an additional freedom to predict the phase behavior of petroleum fluids. The rest of the components in the original reservoir fluid can be lumped as a pseudo idle component (hereafter referred as "PIC"), whose change is induced by PKC. In other scenarios such as depletion processes from gas-condensate or volatile-oil reservoirs, PKC can be defined similarly with an analysis on which component or components in the reservoir fluid dominate the phase behavior.

The introduction of PKC is to help further successfully define a compositional space, in which pressure and PKC mole fraction are considered as independent variables.

The equilibrium ratios K_i and vapor mole fraction f_v are correspondingly treated as dependent variables in Equation (4.29) and (4.30). Assume that the saturation pressures at different PKC mole fractions and equilibrium ratios K_i at those saturation pressures are calculated in advance, a vector of pressure decreasing from saturation pressures to a low end pressure and a vector of PKC mole fraction can be generated. VLE calculation in the compositional space can be efficiently performed using a two-level loop with the pressure in the inner loop and PKC mole fraction in the outer loop. Initial guess of K_i and f_v can be obtained through multi-variable interpolation from the compositional space based on specific pressure and PKC mole fraction condition.

$$K_i = g_3(p, z_{PKC}) \tag{4.29}$$

$$f_v = g_4(p, z_{PKC}) \tag{4.30}$$

The workflow of VLE procedure for sharply varying composition scenario is provided in **Fig. 4.7**. Step 1 is the compositional space construction. Different from Step 1 in **Fig. 4.4**, it constructs a 3D compositional space controlled by pressure and PKC mole fraction z_{PKC}. The dynamic flash includes Step 2 to 4 in the red dash rectangular box. Similar to **Fig. 4.4**, here two options are offered in Step 3. It should be noted that the compositional space is pre-constructed before the dynamic flash calculation, implying a minimal computational overhead.

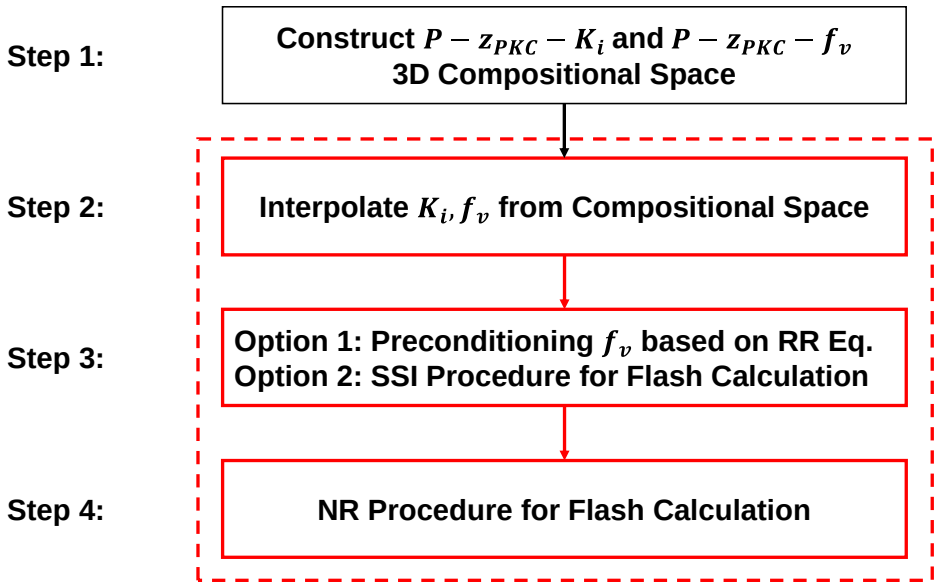

Fig. 4.7—Workflow of flash calculation for fluid with sharp varying composition

4.3.3 Volume Translation

After hydrocarbon fluid properties are calculated by PR-EOS and VLE, a volume translation procedure is used to correct the predicted volumetric properties (Péneloux et al. 1982). However, this procedure does not alter VLE calculation before, so it does not add much complexity. A component correction factor c_i is calculated for each component, as shown in Equation (4.31).

$$c_i = \mathcal{S}_i b_i, (i = 1, 2, \cdots, n_h) \tag{4.31}$$

where $\mathcal{S}_i$ is a shift factor for each component, and b_i is calculated by Equation (A.7) in **Appendix A**.

The overall and phase volume correction factors are calculated by composition weighted average.

$$c = \sum_{i=1}^{n_h} c_i z_i \tag{4.32}$$

$$c_l = \sum_{i=1}^{n_h} c_i x_i \tag{4.33}$$

$$c_v = \sum_{i=1}^{n_h} c_i y_i \tag{4.34}$$

Based on Equations (4.32) to (4.34), the molar volumes and Z-factors are corrected.

$$\mathcal{v}^{shift} = \mathcal{v} - c \tag{4.35}$$

$$\mathcal{v}_l^{shift} = \mathcal{v}_l - c_l \tag{4.36}$$

$$\mathcal{v}_v^{shift} = \mathcal{v}_v - c_l \tag{4.37}$$

$$Z_\alpha^{shifit} = \frac{p\mathcal{v}_\alpha^{shifit}}{RT} \tag{4.38}$$

4.3.4 Oil and Gas Viscosities

After performing VLE and volume translation, oil(liquid) and gas(vapor) viscosities are calculated based on the Lohrez-Bray-Clark correlation (Lohrenz et al. 1964), shown as Equation (4.39),

$$\mu_\alpha = \mu_\alpha^* + \frac{1}{\xi_\alpha}\left[\left(0.0093324\tilde{\rho}_{r_\alpha}^4 - 0.40758\tilde{\rho}_{r_\alpha}^3 + 0.058533\tilde{\rho}_{r_\alpha}^2 + 0.023364\tilde{\rho}_{r_\alpha} + 0.1023\right)^4 - 0.0001\right] \tag{4.39}$$

where μ_α is the phase viscosity, cP; μ_α^* is the phase viscosity at atmospheric pressure, cP; ξ_α is the phase viscosity parameter; $\tilde{\rho}_{r_\alpha}$ is the reduced phase molar density, $lbmol/ft^3$.

The phase viscosity at atmospheric pressure μ_α^* in Equation (4.39) is calculated based on Equations (4.40) to (4.45).

$$\mu_\alpha^* = \frac{\sum_{i=1}^{n_h} x_i^\alpha \mu_i^* \sqrt{MW_i}}{\sum_{i=1}^{n_h} x_i^\alpha \sqrt{MW_i}} \tag{4.40}$$

$$x_i^\alpha = \begin{cases} x_i, & \alpha = l\ (liquid/oil\ phase) \\ y_i, & \alpha = v\ (vapor/gas\ phase) \end{cases} \tag{4.41}$$

$$\mu_i^* = \begin{cases} \frac{0.00034 T_{ri}^{0.94}}{\xi_i}, & T_{ri} \le 1.5 \\ \frac{0.0001778(4.58T_{ri} - 1.67)^{5/8}}{\xi_i}, & Otherwise \end{cases} \tag{4.42}$$

$$T_{ri} = \frac{T}{T_{ci}} \tag{4.43}$$

$$p_{ri} = \frac{p}{p_{ci}} \tag{4.44}$$

$$\xi_i = 5.4402 \frac{T_{ci}^{1/6}}{MW_i^{1/2} p_{ci}^{2/3}} \tag{4.45}$$

The phase viscosity parameter ξ_α in Equation (4.39) is calculated based on Equations (4.46) to (4.49),

$$\xi_\alpha = 5.4402 \frac{T_{pc_\alpha}^{1/6}}{MW_\alpha^{1/2} p_{pc_\alpha}^{2/3}} \tag{4.46}$$

$$T_{pc_\alpha} = \sum_{i=1}^{n_h} x_i^\alpha T_{ci} \tag{4.47}$$

$$p_{pc_\alpha} = \sum_{i=1}^{n_h} x_i^\alpha p_{ci} \tag{4.48}$$

$$MW_\alpha = \sum_{i=1}^{n_h} x_i^\alpha MW_i \tag{4.49}$$

The reduced phase molar density $\tilde{\rho}_{r_\alpha}$ in Equation (4.39) is defined by the ratio of phase molar density $\tilde{\rho}_\alpha$ to pseudocritical phase molar density $\tilde{\rho}_{pc_\alpha}$, as shown in Equations (4.50) to (4.51),

$$\tilde{\rho}_{r_\alpha} = \frac{\tilde{\rho}_\alpha}{\tilde{\rho}_{pc_\alpha}} \tag{4.50}$$

$$\tilde{\rho}_{pc_\alpha} = \frac{1}{\sum_{i=1}^{nh} x_i^\alpha v_{c_i}} \tag{4.51}$$

4.3.5 Water Properties

Water density is calculated based on water formation volume factor B_w, and B_w is related to water compressibility C_w and pressure changes (Schlumberger 2012),

$$\rho_w = \frac{\rho_w^{sc}}{B_w} \tag{4.52}$$

$$B_w = \frac{B_w^{ref}}{1+X+0.5X^2} \tag{4.53}$$

$$X = C_w(p - p_{ref}) \tag{4.54}$$

Viscosity are treated as a function of pressure, and it is calculated based on water viscosibility C_{μ_w} and pressure changes (Schlumberger 2012),

$$\mu_w = \frac{\mu_w^{ref}}{1+Y+0.5Y^2} \tag{4.55}$$

$$Y = -C_{\mu_w}(p - p_{ref}) \tag{4.56}$$

4.3.6 Rock-Fluid Functions

4.3.6.1 Capillary Pressure

In fluid dynamics capillary pressure is the pressure difference across the phase interface between two immiscible fluids. In petroleum engineering capillary pressure is usually defined as Equation (4.57), which is a phase pressure difference between non-wetting phase and wetting phase.

$$p_c = p_{nwet} - p_{wet} \tag{4.57}$$

Based on Equation (4.57), only oil phase pressure is involved in the primary variable vector, and other phase pressures are considered as secondary variables. Usually oil is considered to be a non-wetting phase in oil-water system, and gas is treated as non-wetting phase if it exists. Capillary pressures are considered to be functions of fluid saturations in GURU.

4.3.6.2 Relative Permeability Curve

In GURU phase relative permeability is involved in multiphase Darcian flux term and well term in mass balance equations. Relative permeability curves can be measured through experiments, and are characterized as functions of saturations. There exist multiple methods to obtain three phase oil relative permeability, and here the default oil relative permeability calculation method is Stone II (Stone 1973), as shown in Equation (4.58),

$$k_{ro} = k_{rocw}[\left(\frac{k_{row}}{k_{rocw}} + k_{rw}\right)\left(\frac{k_{rog}}{k_{rocw}} + k_{rg}\right) - k_{rw} - k_{rg}] \tag{4.58}$$

where k_{ro} is the oil relative permeability in oil-gas-water system; k_{row} represents the oil relative permeability at actual water saturation; k_{rocw} denotes the oil relative permeability at connate water saturation; k_{rw} is the water relative permeability at actual water saturation; k_{rog} is the oil relative permeability at connate water saturation and actual gas saturation; k_{rg} is the gas relative permeability at actual gas saturation.

4.3.7 Rock Compressibility

Rock porosity or pore volume reduces with the decrease of pore pressure, and vice versa. Therefore, the rock porosity is calculated based on rock compressibility and pore pressure changes (Dake 1978), as shown in Equation (4.59),

$$\phi = \phi_{ref} e^{C_r(p-p_{ref})} \tag{4.59}$$

Rock compressibility is a property associated with rock type. For example, in fractured reservoirs the compressibilities of fracture and matrix can be different.

4.3.8 Gas Shale Apparent Permeability

Shale matrix is extremely tight and the influences of non-Darcy flow in the nano-porous media cannot be ignored. In shale matrix, organic matrix or kerogen distributes in inorganic matrix (Ambrose et al. 2012). Nano-pores are widely developed in kerogen due to the generation of hydrocarbon in geological ages (Wang and Reed 2009), and those nano-pores have good capacity for absorbed gas and compressed gas storage (Ambrose et al. 2012). Besides, the interaction between gas molecules and nano-pore wall influences

the gas flow within the nano-pores. Thus gas slippage and Knudsen diffusion is also important and can be considered using matrix apparent permeability (Civan 2010; WuChen et al. 2015; Wu et al. 2016; WuLi et al. 2015).

Since GURU considers rock types as cell information (**Figure 4.1**), this eases the consideration of gas slippage and Knudsen diffusion in shale matrix through tracking rock type of cells. Therefore, the dynamic gas matrix apparent permeability or half-transmissibility (Equation (4.7)) in each cell is incorporated through a permeability multiplier as defined in Equation (4.60),

$$k = \begin{cases} \eta k_0, & cell\ j\ \in shale\ matrix\ \&\ gas\ flux\ only \\ k_0, & otherwise \end{cases} \tag{4.60}$$

where η is gas apparent permeability multiplier, dimensionless; k_0 is the intrinsic medium permeability, mD.

As shown in Equation (4.60), if only Darcy flow is considered for the specific component or fluid, the permeability is constant at k_0.

GURU is a compositional simulator, so the apparent permeability multiplier is based on gas component instead of gas phase. Specifically it is related to Knudsen number $K_{n,i}$ (Equation (4.61)), which is a ratio of mean free path of gas molecule to pore radii. The mean free path λ_i is calculated component-wise (Jiang and Younis 2016) through Equation (4.62) ,and average matrix pore radii is calculated through the correlation from Aguilera (2010) (Equation (4.63)). Ultimately the apparent permeability multiplier η_i is also individually for each gas component, and is defined through Equation (4.64) and (4.65).

$$K_{n,i} = \frac{\lambda_i}{r} \tag{4.61}$$

$$\lambda_i = \frac{1}{\sqrt{2}\pi\tilde{\rho}_g N_A d_{m,i}^2} \tag{4.62}$$

$$r = 2.665\left(\frac{k_0}{100\phi}\right)^{0.45} \tag{4.63}$$

$$\eta_i = f\left(K_{n,i}\right) = (1 + \alpha_i K_{n,i})(1 + \frac{4K_{n,i}}{1+K_{n,i}}) \tag{4.64}$$

$$\alpha_i = \frac{128}{15\pi^2}\arctan(4K_{n,i}^{0.4}) \tag{4.65}$$

4.4 Global Linear System

4.4.1 Primary Equations and Variables

There exist two main categories of primary equations or residuals in GURU, including reservoir residuals and well residuals. The reservoir residuals are Equations (4.1), (4.4) and (4.16), and the well residuals is any one of the Equations from (4.17) to (4.21). Correspondingly, two categories of primary variables are solved from the primary equations: the first category is the reservoir primary variables, including the number of moles of each hydrocarbon component N_i and the number of moles of water component N_w in unit cell volume, oil pressure p_o; and the second category is the bottom-hole pressure p_{wf}. **Table 4.1** summarizes those primary equations and variables in the fully implicit compositional formulation. As shown in **Table 4.1**, $(n_h + 2) \times nCells$ reservoir residuals and $nWells$ well residuals are solved as primary equations, which correspond to the same number of primary variables. Here $nCells$ and $nWells$ represent number of active cells and wells in the model respectively.

Table 4.1—Summary of primary equations and variables

Equations	Number	Variables	Number
Mass balance (4.1)	$n_h \times nCells$	N_i	$n_h \times nCells$
Mass balance (4.4)	$1 \times nCells$	N_w	$1 \times nCells$
Volume balance (4.16)	$1 \times nCells$	p_o	$1 \times nCells$
Any well constraint from (4.17) to (4.21)	$1 \times nWells$	p_{wf}	$1 \times nWells$
Total	$(n_h + 2) \times nCells + nWells$		$(n_h + 2) \times nCells + nWells$

Therefore, the residual vector $\vec{R}$ is formed by reservoir and well residuals, and its size is thus $(n_h + 2) \times nCells + nWells$. The global ordering of the residual vector is shown in Equation (4.66). The ordering of reservoir residuals is shown in Equation (4.67), where there is an inner component loop nested in the cell loop; on the other hand, well residuals follow the reservoir residuals and are ordered by the ordering of active wells, as shown in Equation (4.68).

$$\vec{R} = \begin{bmatrix} \vec{R}_{res} \\ \vec{R}_{well} \end{bmatrix} \tag{4.66}$$

$$\vec{R}_{res} = \begin{bmatrix} \vec{R}_{i,j} \\ R_{w,j} \\ R_{vol,j} \end{bmatrix}_{i=1,\cdots,n_h;\ j=1,\cdots,nCells;} \tag{4.67}$$

$$\vec{R}_{well} = \left[R_{well,w} \right]^T_{w=1,\cdots,nWells} \tag{4.68}$$

Similarly, the primary unknown vector $\vec{X}$ is comprised of reservoir and well variables, and its length equals to the residual vector. The ordering for $\vec{X}$ is,

$$\vec{X} = \begin{bmatrix} \vec{X}_{res} \\ \vec{X}_{well} \end{bmatrix} \tag{4.69}$$

$$\vec{X}_{res} = \begin{bmatrix} \vec{N}_{i,j} \\ N_{w,j} \\ p_{o,j} \end{bmatrix}_{i=1,\cdots,n_h; j=1,\cdots,nCells;} \tag{4.70}$$

$$\vec{X}_{well} = \left[p_{wf,w} \right]^{T}_{w=1,\cdots,nWells} \tag{4.71}$$

The global linear system of the model becomes Equation (4.72). Further it can be written in the format of Equation (4.73). In Equation (4.73), the Jacobian system includes reservoir Jacobian (top row) and well Jacobian (bottom row), and this is consistent with the ordering of the primary variables and equations.

$$J\vec{\delta} = \vec{R} \tag{4.72}$$

$$\begin{bmatrix} \frac{\partial \vec{R}_{res}}{\partial \vec{X}_{res}} & \frac{\partial \vec{R}_{res}}{\partial \vec{X}_{well}} \\ \frac{\partial \vec{R}_{well}}{\partial \vec{X}_{res}} & \frac{\partial \vec{R}_{well}}{\partial \vec{X}_{well}} \end{bmatrix} \begin{bmatrix} \overrightarrow{\Delta X}_{res} \\ \overrightarrow{\Delta X}_{well} \end{bmatrix} = \begin{bmatrix} \vec{R}_{res} \\ \vec{R}_{well} \end{bmatrix} \tag{4.73}$$

4.4.2 Jacobian Calculation and Construction

The Jacobian matrix in GURU are calculated based on numerical differentiation for the sake of its easy implementation and mechanistic investigation purpose in this work. Numerical Jacobian basically requires two functional evaluations for the residual equations (Dennis and Schnabel 1983), as shown in Equations (4.74) to (4.75),

$$\frac{\partial R_i}{\partial x_j} = \frac{R_i(x_j+\epsilon_j) - R_i(x_j)}{\epsilon_j} \tag{4.74}$$

$$\epsilon_j = \sqrt{\eta} \cdot \max\{|\vec{x}|, typical\ x_j\} \cdot \Theta(x_j) \tag{4.75}$$

where R_i is the residual function, x_j is the perturbed variable, ϵ_j is the perturbation, η is machine precision, $\Theta(x_j)$ is the correct root searching direction of x_j, and $|\vec{x}|$ is the variable vector belonging to the same type, which in GURU can be $\{N_i\}$, $\{N_w\}$, $\{p_o\}$ and $\{p_{wf}\}$.

Further, ϵ_j is ensured to be an exact float number in computer by manipulating it as Equations (4.76) and (4.77) (Dennis and Schnabel 1983).

$$temp = x_j + \epsilon_j \tag{4.76}$$

$$\epsilon_j = temp - x_j \tag{4.77}$$

Fig. 4.8 presents the comparison between numerical differentiation and analytical differentiation. It is based on the derivatives of a well residual with regards to 6 related independent variables. It shows that numerical differentiation can provides sufficient accuracy for fully implicit approach here.

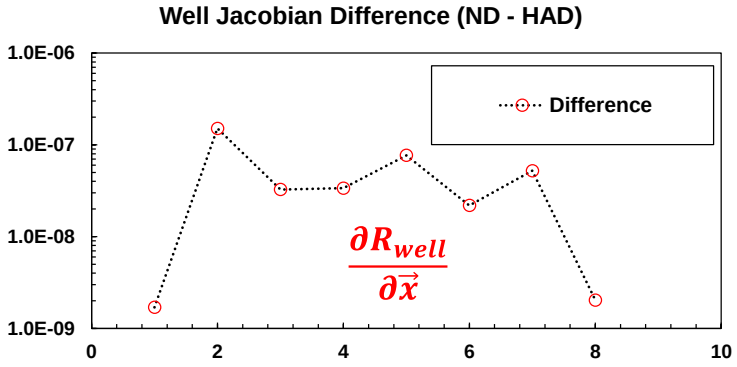

Fig. 4.8—Comparison between numerical differentiation (ND) and hard analytical differentiation (HAD)

As discussed in Lim et al. (1995), block-based approach to construct Jacobian has to evaluate each term in the residuals by cell and cannot avoid trivial zero transmissibilities for cells with non-flow boundary conditions, and it becomes extremely difficult and redundant for unstructured grid discretization. Moreover, there exist intrinsic symmetries in the mass balance equations. Specifically the flux terms between two connected cells in the mass balance equations are opposite and they are connection-based, but the accumulation term in the mass balance equations and all the volume balance equations become locally cells-based. Certainly extra care needs to be taken for source/sink terms, but their contribution to the reservoir mass balance equation systems is sparse but not global.

Following the philosophy of Lim et al. (1995), the Jacobian construction is split into two parts, including connection-based Jacobian and cell-based Jacobian. For example, **Fig. 4.9(a)** is a case of 1-D single phase black-oil model, and well is temporarily not considered in the domain. The construction of Jacobian is a summation of connection-based Jacobian and cell-based Jacobian, as shown in **Fig. 4.9(b)**. It shows that Jacobian submatrix related to flux has both diagonal and off-diagonal entries, and the distribution of those nonzero entries depends on the cell connection topology during grid-discretization. In this 1-D problem here Jacobian submatrix related to flux is simply tridiagonal. On the other hand, the Jacobian submatrix related to accumulation has only diagonal entries. In multiphase black-oil problems or compositional problems, their X and Y in the Jacobian might become block submatrices, and the dimensions of those submatrices are determined by the degree of freedom solved in each cell.

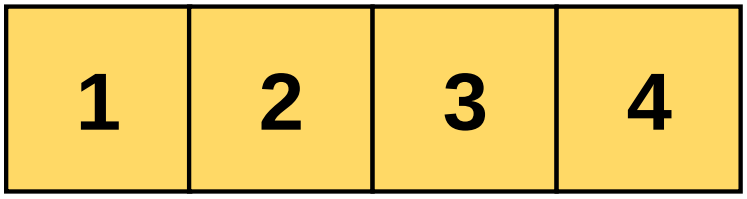

(a)

$$J_r = \begin{bmatrix} X & X & & \\ X & X & X & \\ & X & X & X \\ & & X & X \end{bmatrix} + \begin{bmatrix} Y & & & \\ & Y & & \\ & & Y & \\ & & & Y \end{bmatrix}$$

Connection – Based Jacobian(Flux) | Cell – Based Jacobian (Accumulation)

(b)

Fig. 4.9— (a) 1-D single phase black-oil model with 4 cells; (b) Jacobian for (a)

Moreover, by applying overall qualities as primary variables, the splitting Jacobian construction approach also leads to perfectly linearized accumulation term in Jacobian for mass balance equations. Taking Equations (4.1) and (4.4) as examples, their accumulation Jacobian terms with regards to component mass in cell, excluding gas adsorption/desorption here, become constant as shown in Equations (4.78) and (4.79).

$$\frac{\partial}{\partial N_{i,\mathrm{j}}^{n+1}}\left\{\frac{V_j}{\Delta t}\left(N_{i,\mathrm{j}}^{n+1} - N_{i,\mathrm{j}}^{n}\right)\right\} = \frac{V_j}{\Delta t} \tag{4.78}$$

$$\frac{\partial}{\partial N_{w,j}^{n+1}}\left\{\frac{V_j}{\Delta t}\left(N_{w,j}^{n+1} - N_{w,j}^{n}\right)\right\} = \frac{V_j}{\Delta t} \tag{4.79}$$

4.4.3 Jacobian Storage and Linear Solvers

Jacobian matrices in compositional simulation are usually sparse. Depending on the linear solver requirement, multiple sparse matrix storage formats and their mutual convertors are implemented in GURU, including triplet format, Compressed Row Storage (CRS), and Modified Compressed Row Storage (MCRS) (Tuminaro et al. 1999). Their memory cost follows the sequence of triplet format > CRS > MCRS. Since the Jacobian filling process in GURU is aligned with the ordering of primary variables in Equation (4.73), the matrix is firstly stored in triplet format and then transformed into other formats based on the requirement of linear solvers.

GURU is interfaced with two different GMRES iterative solvers with ILU preconditioners. The first one is from Ju and Burkardt (2011), which is compatible with CRS matrix format. The other one is from Aztec library developed by Tuminaro et al. (1999), which requires MCRS matrix format. For the flash/VLE calculation, linear solver is also required to solve the small dense Jacobian matrix of vapor-liquid equilibrium. Here the small Jacobian matrix is stored in full format because of its simplicity. The linear system in VLE is solved by a self-implemented direct solver of Gaussian Elimination with pivoting method.

4.5 Simulation Workflow

GURU is implemented through a group of modules with independent features, and the purpose of this design is to make it be highly extendable for future research. Currently, GURU includes six main modules (**Fig. 4.10**), including rock-fluid, fluid, well control,

mobility, flow equations, and linear solver modules. Specifically, rock-fluid module is to calculation rock properties, and rock-fluid function, such as relative permeability and capillary pressure. Fluid module is important and includes some of the most frequently called subroutines such as VLE and PR-EOS subroutines. Besides, water properties and multi-component gas adsorption/desorption is calculated here. Well control module is to analyze different well constraints, calculate wellbore gradient, and construct well Jacobian and residuals. Mobility module is to compute mobility for flux and also other flux-related sub-terms. Flow equation module is to construct global Jacobian and residuals (RHS) in the linear system. Ultimately, the linear solver module is engine to solve linear systems in compositional simulation. GURU is prototyped with MATLAB (Mathworks 2015), and then completely rewritten in object-oriented FORTRAN (Chapman 2007).

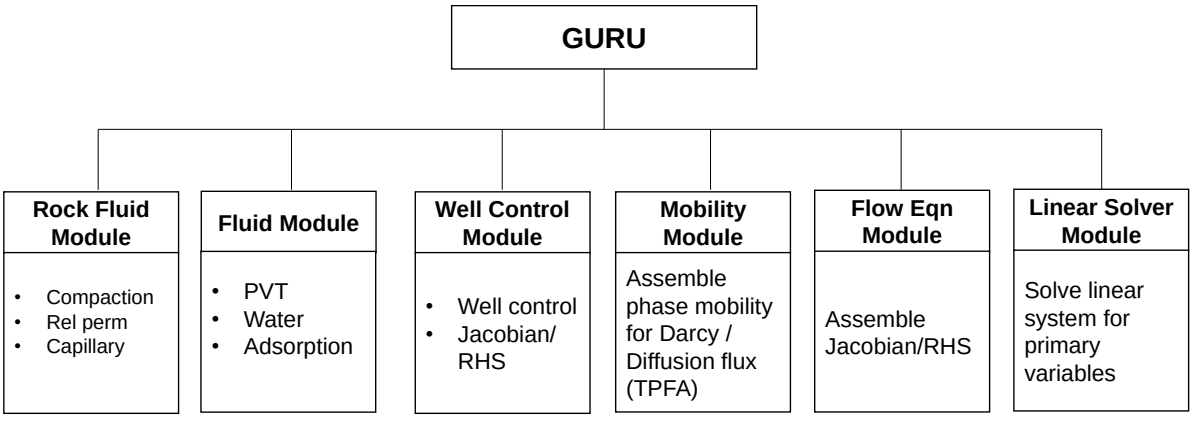

Fig. 4.10—Module tree in GURU

The simulation workflow is presented in **Fig. 4.11**. After the input file is read, data quality is carefully checked, and miscellaneous data and initialization is calculated during

this step. Next, data passes through the simulator engine at time-loop level. The newton solver is the kernel of the simulator and starts with initial guesses of the primary variables, then constructs linear system and delivers it to linear solver package. After linear solver converges, solution is returned to update primary variables, followed by updating secondary variables. The newton loop is repeated until certain convergence criterion is reached. Converged results returned from the kernel is further output as data files, curves, and pictures etc. Then get into the next time-step until all simulation time-steps are finished. Therefore, the newton loop is nested in the time-step loop.

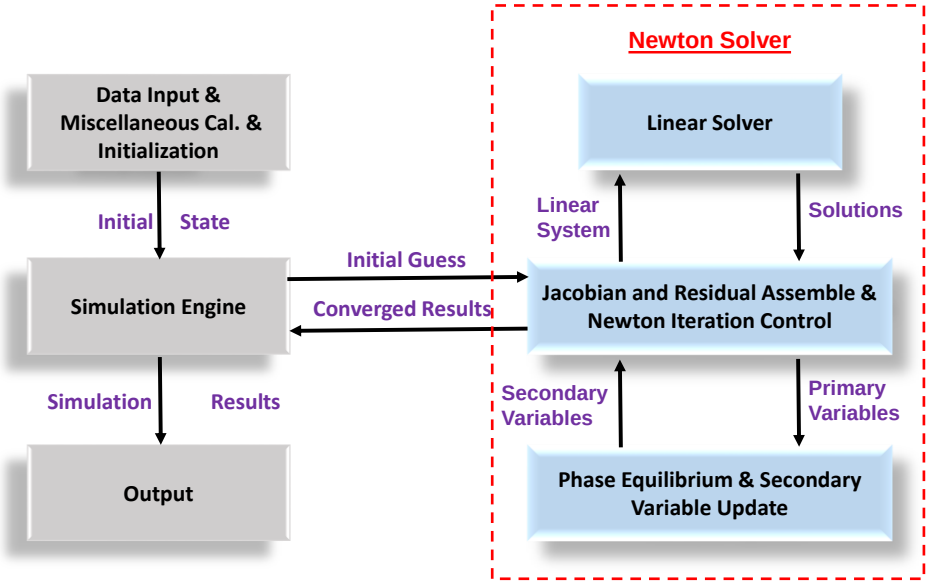

Fig. 4.11—Simulation workflow in GURU

4.6 Summary

In this chapter, a fully implicit unstructured compositional simulator GURU has been developed. Based on Control-Volume Finite-Difference method, the simulator enables to flexibly handle different grid discretization approaches. Besides, the adoption of overall qualities variables enables GURU to avoid variable switch when phase changes. Gas shale mechanisms such as multi-component adsorption/desorption, Knudsen diffusion and gas slippage flow have been implemented in GURU, so it is ready for shale gas reservoir modeling. Besides, an efficient set of compositional space preconditioned vapor-liquid equilibrium calculation methods have been proposed, and they are appropriate for fluid with slightly varying or constant composition and fluid with sharply varying composition.

CHAPTER V

VALIDATION OF GURU AND VLE ALGORITHMS

In Chapter IV, the formulation of GURU and its overall workflow have been comprehensively discussed. Based on this, the main task of this chapter is to validate the simulator and its related algorithms with regards to the following three aspects,

- 3D multiphase compositional simulation based on GURU;
- Multiphase discrete fracture reservoir modeling based on GURU;
- Validation of efficiency for the new proposed VLE workflow.

5.1 Compositional Simulation Benchmark Case

GURU is unstructured such that it has no limitation to spatial dimension any more. Therefore, here a synthetic 3D 3-phase case is tested to calibrate it with Eclipse 300 (Schlumberger 2012), which is an industrial standard compositional simulator. In **Fig. 5.1**, there are two wells drilled in the reservoir, with a water injector perforated at cell (1, 1, 1) and cell (1, 1, 3) and a producer perforated at cell (15, 15, 1) and cell (15, 15, 2), thus the model represents a quarter of an inverted five-spot pattern. Besides, horizontal permeability distribution is shown in **Fig. 5.1**. Horizontal permeability in each layer is the same and the ratio of vertical to horizontal permeability is 0.10. Thus the permeability field is heterogeneous and anisotropic.

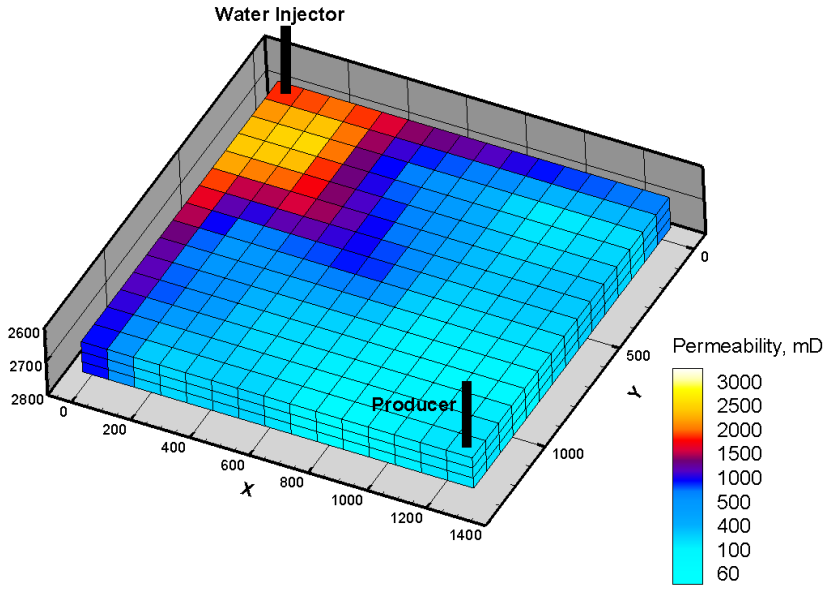

Fig. 5.1—Horizontal permeability distribution in the benchmark case

Table 5.1—Basic reservoir parameters in compositional simulation benchmark case

Reservoir size (ft^3)	$1{,}320 \times 1{,}320 \times 90$
Grid dimension in x-y-z space	$15 \times 15 \times 3$
Reservoir top depth (ft)	2,665
Porosity (v/v)	0.2
Mean horizontal permeability k_h (mD)	400.2
k_v/k_h (mD)	0.1
Water saturation S_w	0.35
Initial reservoir pressure ($psia$)	6,000
Reservoir temperature (°F)	200
Perforated cells for producer	(15, 15, 1) and (15, 15, 2)
Reference depth for producer (ft)	2,680
Minimum producer BHP ($psia$)	1,000
Maximum producer oil rate (stb/day)	2,000
Perforated cells for injector	(1, 1, 1) and (1, 1, 3)
Reference depth for injector (ft)	2,680
Maximum injector BHP ($psia$)	6,500
Minimum injector water rate (stb/day)	2,000
Simulation time (days)	365

The basic reservoir parameters are presented in **Table 5.1**. The initial reservoir pressure is $6{,}000\ psia$, initial water saturation is 0.35 and irreducible water saturation is 0.16. The producer is constrained by a minimum BHP, $1{,}000\ psia$, and a maximum oil rate, $2{,}000\ STB/day$, while the injector is controlled by a maximum BHP, $6{,}500\ psia$, and a minimum water rate, $2{,}000\ STB/day$. Since this is a Cartesian model, the well index for GURU is calculated based on Peaceman's model (Peaceman 1990).

The compositional fluid properties are illustrated in **Table 5.2**. As shown in **Table 5.2**, there are 5 components ($CO_2, CH_4, C_{2-4}, C_{5-6}, C_{7+}$) in the hydrocarbon mixture, and the bubble point pressure p_b for the fluid mixture is $5{,}557.517\ psia$. Because here the initial reservoir pressure ($6{,}000\ psia$) is higher than the original fluid bubble point pressure, so the reservoir starts with oil and water, and then gas phase appears as pressure quickly decreases below bubble point pressure.

Table 5.2—Compositional fluid properties for 5-component EOS characterization

Component	n(initial)	T_c (°F)	P_c ($psia$)	ω	M_w (g/mol)	δ_{i,CO_2}	δ_{i,CH_4}
CO_2	0.0006	88.46	1071.33	0.28686	44.01	-	-
CH_4	0.6001	117.40	667.78	0.013	16.093	0.1	-
C_{2-4}	0.0655	132.35	578.51	0.02567	0.02567	-	-
C_{5-6}	0.0403	605.10	510.15	0.19164	0.19164	-	0.018
C_{7+}	0.2935	630.00	357.87	0.89134	0.89134	-	0.041
p_b ($pisa$)	5,557.517						

The rock fluid table are from the work of (Valbuena 2015). Oil-water and oil-gas relative permeability curves are presented in **Fig. 5.2(a)** and **(b)**, and the oil relative

permeability is calculated based on Stone II method (Stone 1973). Further, in **Fig. 5.2(c)** oil-water capillary pressure is considered but that oil-gas capillary pressure is considered to zero.

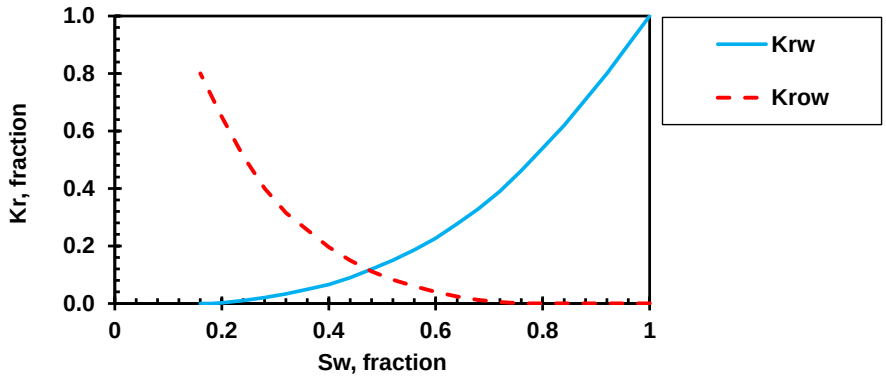

(a)

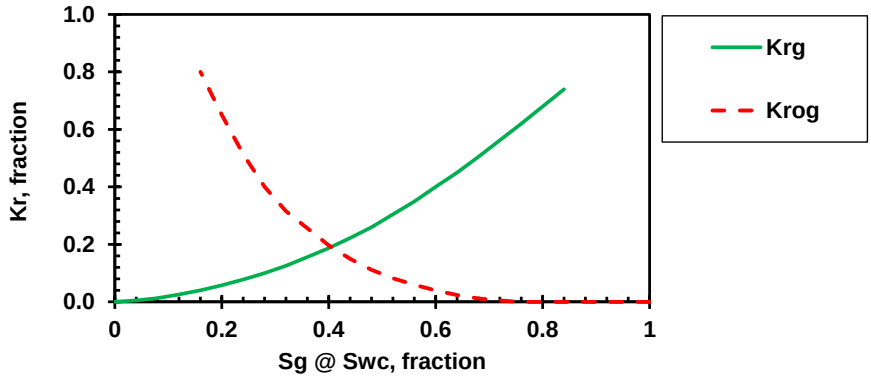

(b)

Fig. 5.2—Rock-fluid functions used in this study. (a) Oil and water relative permeability in the matrix and fractures; (b) Oil and gas relative permeability in the matrix and fracture; (c) Oil-water and gas-oil capillary pressure curves. Oil-gas capillarity is assumed to be zero.

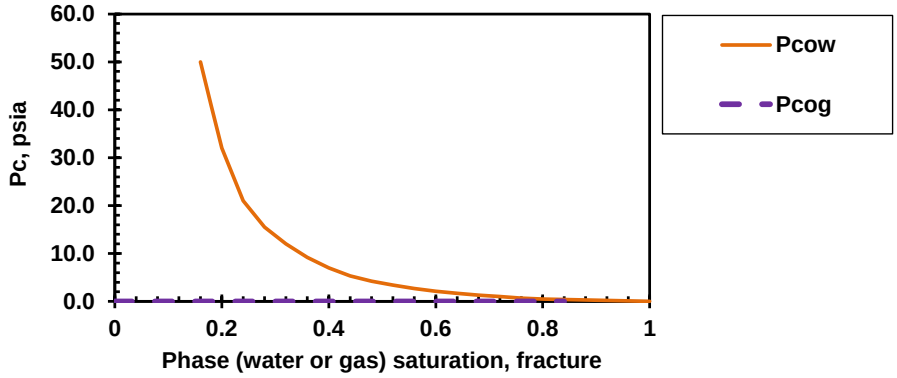

(c)

Fig. 5.2—Continued.

The reservoir model with the same input data runs through GURU and Eclipse 300, and here the comparison between them is presented in **Fig. 5.3**. **Fig. 5.3** illustrates that a very good match between GURU and Eclipse 300 results is obtained with respects to those important reservoir performance parameters. The relative difference (L-2 norm) between the two simulators is quite small and acceptable. In **Fig. 5.3(b)** and **(d)** it shows there is a switch of producer schedule from constant oil rate to constant bottom-hole pressure, and the transition of the switch in GURU is quite smooth and very close to Eclipse results.

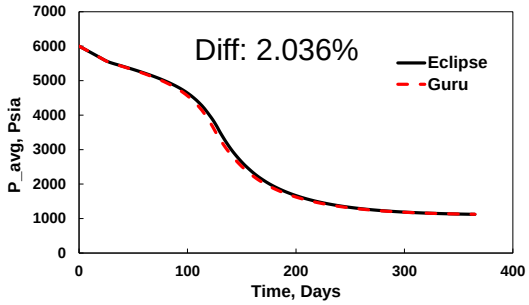

(a) Average reservoir pressure

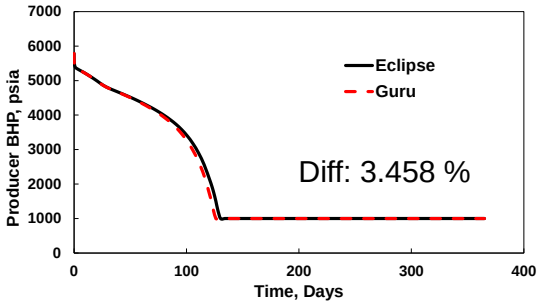

(b) Producer bottom-hole pressure

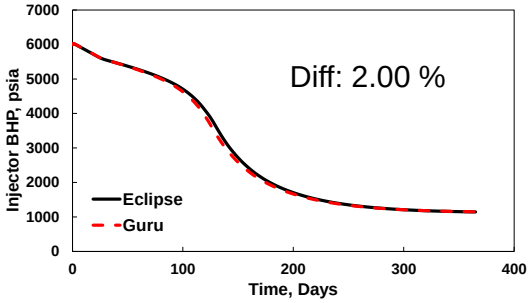

(c) Injector bottom-hole pressure

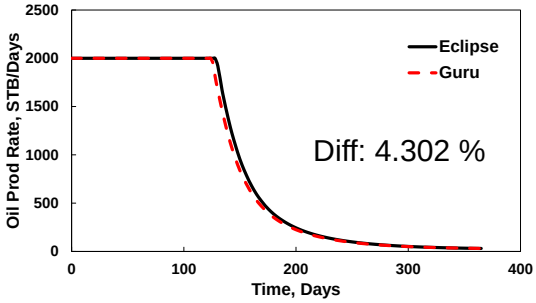

(d) Oil production rate

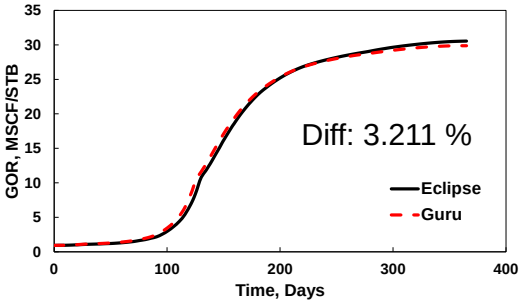

(e) Gas oil ratio

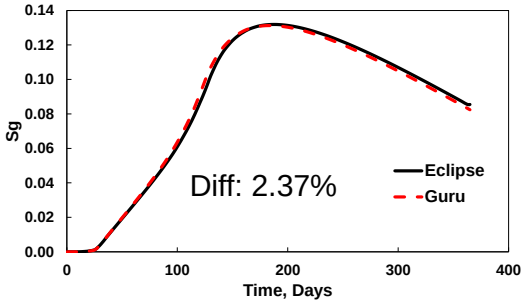

(f) Average gas saturation

Fig. 5.3—Comparison of GURU and Eclipse 300 for the benchmark case

There are vertically 3 layers in the reservoir. Because of the fluid density contrast, it is expected to observe fluid segregation phenomenon. **Fig. 5.4** shows the average gas and water saturation in 3 layers in the reservoir. **Fig. 5.4(a)** shows that water saturation

increases with reservoir depth increasing and gradually accumulates at the bottom layer. On the other hand, after pressure drop to bubble point pressure, gas bubbles emit and lift to the top layer and gas saturation increases as reservoir depth decreases, as shown in **Fig. 5.4(b)**.

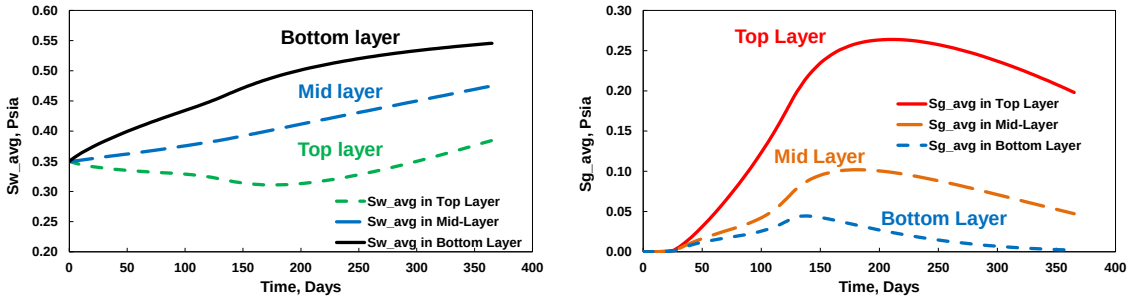

(a) (b)

Fig. 5.4—Layer averaged fluid saturation with time in the model: (a) S_w; (b) S_g

Fig. 5.5 illustrate the saturation map of water and gas in the reservoir at 302.7 $days$ ($p_{avg} < p_b$). It shows that the water saturation is the highest near the water injector and a water bed forms at the bottom layer, while the gas saturation is highest as gas cap at the top layer and almost zero at bottom layer, which is consistent with blue dash line in **Fig. 5.4(b)**. Because gas has much higher well mobility than other phases, gas saturation is lower at the top layer nearby the producer than that in neighboring zone at the same layer.

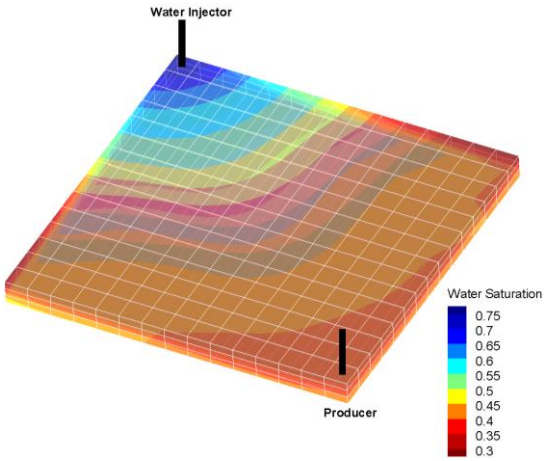

(a)

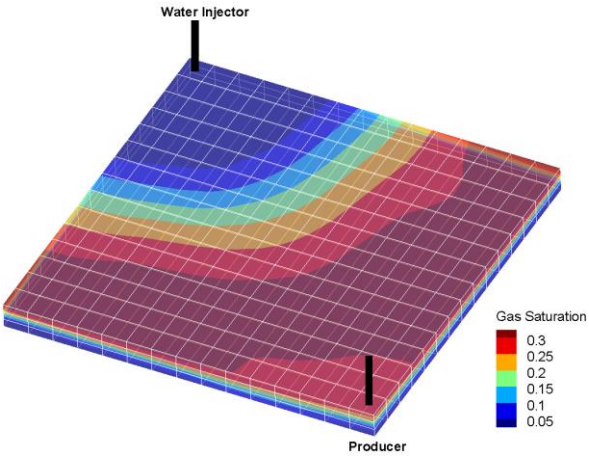

(b)

Fig. 5.5—Water (a) and gas (b) saturation map at t = 302.7 $days$

5.2 Discrete Fracture Reservoir Models

One of the thrust areas of GURU is to handle complex grid discretization, so discrete geological features such as fracture networks can be conveniently handled by GURU. In this section two different unstructured grid discretization approaches from external resources are compared based on upon GURU platform.

5.2.1 Enhanced Discrete Fracture Network (EDFN)

The first approach is Enhanced Discrete Fracture Network (EDFN) Model from the work of Mi et al. (2016). EDFN adopts the concept of Dual-Porosity Model that fracture network contributes the global flow and matrix blocks serve as source/sink terms for the fracture system. However, instead of being treated as a homogenized domain, fracture system is discretized based on fracture intersection and extremities. By doing this the details of fractures are accurately captured with the minimum number of fracture computational elements (**Fig. 5.6**). Therefore, in EDFN fractures always serve as boundaries of matrix blocks and reduces the complexity of matrix-fracture connection.

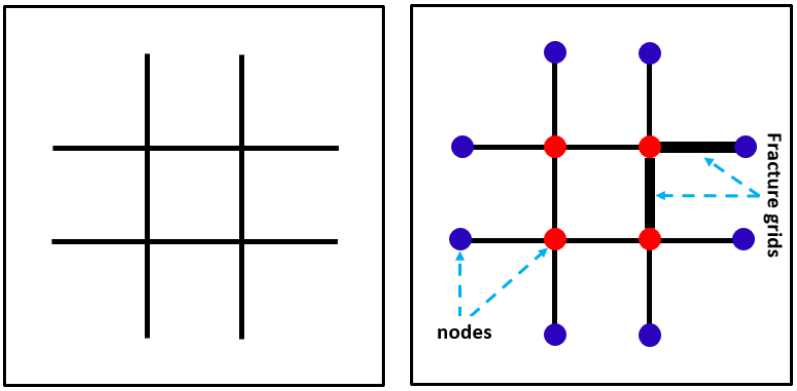

(a) (b)

Fig. 5.6—(a) Schematic of fracture network distributed in 2D domain; (b) fracture grids defined by fracture intersections (red nodes) and fracture extremities (blue nodes) (based on Mi et al. (2016))

Further, matrix domain is coarsely partitioned by the closest distance to the local fracture grid by rapid image processing algorithm (Sarda et al. 2001). For example, the matrix domain in **Fig. 5.6** is coarsely partitioned into a grid map as shown in **Fig. 5.7**. In **Fig. 5.7**, any point in a colored matrix block is closer to the corresponding fracture grid than to any other fracture grids in the domain.

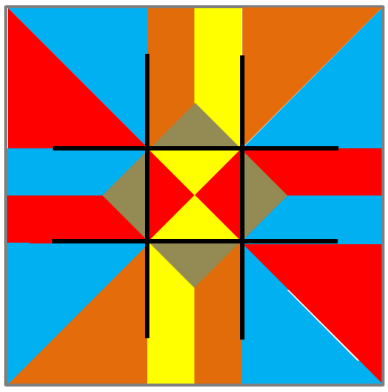

Fig. 5.7—Discretization of the matrix medium in Fig. 5.6 (based on Mi et al. (2016))

The geometries of the coarse matrix grid block can be different depending on the controlling area of each fracture grid. The accuracy of flow simulation may be heavily impacted especially when the matrix blocks have extremely large grid volumes. It thus becomes necessary to improve the numerical accuracy. In EDFN a coarse matrix block with irregular shape (**Fig. 5.8(a)**) is firstly mapped to a rectangular matrix block with the same grid volume (**Fig. 5.8(b)**) with the width being equal to the associated fracture length (black solid lines in **Fig. 5.8**). Further, the rectangular matrix block is logarithmically refined in the direction perpendicular to the fracture surface. The flow in between those

logarithmic fine matrix grids is simply 1D flow. The transient flow between the matrix and fracture then can be accurately captured through fine partition in each local coarse matrix block.

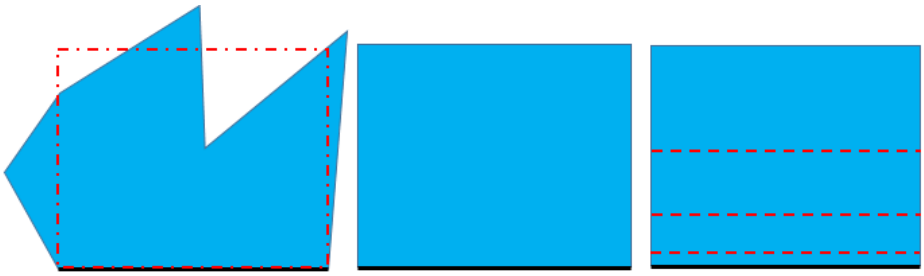

(a) (b) (c)

Fig. 5.8—Improve matrix resolution through transforming into a rectangular block and 1D logarithmic refinement (based on Mi et al. (2016)).

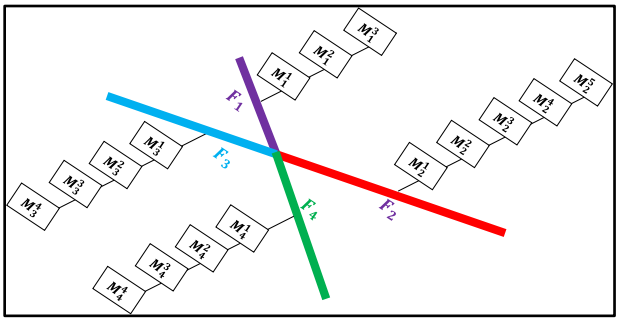

Fig. 5.9—Connection schematic in EDFN. F_i: fracture grid i; M_i^j: matrix subgrid j associated with F_i

As an illustration, the 2D connection topology for two intersected fractures is shown in **Fig. 5.9**. For simplicity it is assumed that only one coarse matrix grid block is connected with each fracture grid, and the maximum number of matrix grid refinement is

5. As shown in **Fig. 5.9**, EDFN is theoretically a Dual-Porosity Single-Permeability Model, but it honors the fracture sparsity and orientation.

5.2.2 Embedded Discrete Fracture Model (EDFM)

Embedded Discrete Fracture Model (EDFM) is recently a very popular approach for fractured reservoir modeling (Chai et al. 2016a, 2016b; Lee et al. 2001; Moinfar et al. 2013, 2014). The basic idea is that fractures are treated as quadrilateral plates embedded into the structured matrix background. Therefore, the obvious advantage of this approach is that it maximally conserves the structured grid discretization and thus brings a more structured Jacobian system during flow simulation.

The fluid flow transfer between matrix and fracture is based on geometric transmissibility in terms of Non-Neighbor Connection (NNC). On the other hand, matrix grids are globally connected with each other in terms of Neighbor Connection (NC). Therefore, EDFM is actually theoretically a Dual-Porosity Dual-Permeability Model. In this work, the EDFM grid discretization is provided by the preprocessor developed by Chai et al. (2016b).

5.2.3 Comparison of EDFN and EDFM

GURU is the platform to run both EDFN and EDFM Models here, and it only requires different grid discretization following the format of GURU. In this case there are 31 arbitrarily oriented fractures in a rectangular reservoir, shown in **Fig. 5.10(a)**, and the

fracture system exhibits global connectivity. A producer is drilled at the center of the rectangular domain and perforates one of the fractures.

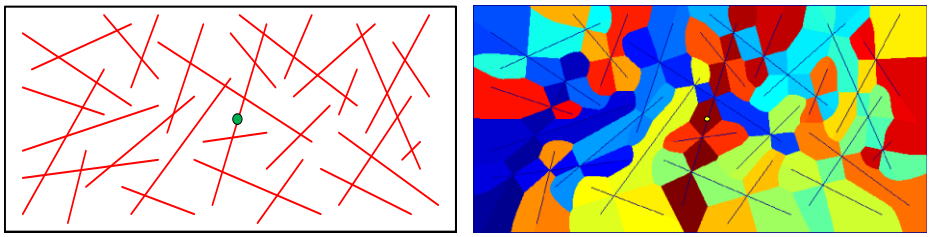

(a) (b)

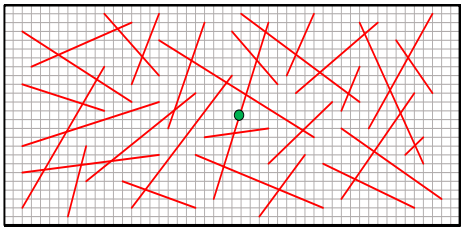

(c)

Fig. 5.10—(a) reservoir with 31 non-orthogonal fractures; (b) EDFN discretization; (c) EDFM discretization.

The discretization of this reservoir model are presented in **Fig. 5.10(b)** and **(c)**. In **Fig. 5.10(b)**, EDFN is applied and the matrix domain is discretized by coarse matrix blocks with varying sizes. Further to further ensure the solution accuracy, matrix blocks are refined by maximally 5 logarithmic sub-grids. In **Fig. 5.10(c)**, EDFM treats fractures as line segments and the matrix is discretized by fine rectangular grids. Basic reservoir parameters are illustrated in **Table 5.3**. Here both of the discrete fracture models

completely capture fracture orientations, so fracture conductivity, fracture and matrix pore volumes in those two different models are exactly identical.

Table 5.3—Basic reservoir parameters

Reservoir size (ft^3)	$1{,}000 \times 500 \times 100$
Reservoir top depth (ft)	3,050
Number of fractures	31
Fracture permeability k_f (mD)	1,000
Fracture aperture w_f (ft)	0.5
Fracture porosity ϕ_f (v/v)	0.4
Matrix permeability k_m (mD)	0.1
Matrix porosity ϕ_m (v/v)	0.2
Wellbore radius (ft)	0.25
Water saturation S_w	0.35
Initial pressure ($psia$)	5,000
Reservoir temperature (°F)	200
Minimum bottom-hole pressure ($psia$)	1,000
Maximum oil rate (stb/day)	100
Simulation time (days)	1,000

The rock-fluid functions for both matrix and fracture are presented in **Fig. 5.11 (a)** to **(c)**. Linear relative permeability curves are used in the fractures. In the matrix we consider that gas saturation is zero in oil-water system, while oil-gas system is measured at connate water saturation ($S_{wc} = 0.16$). Stone II method (Stone 1973) is used to calculate three-phase relative permeabilities. In **Fig. 5.11(c)** capillary pressures in the fractures are considered to be zero, while the capillary pressures between oil and water in the matrix are considered as a function of water saturation. It is assumed that matrix is water-wet here.

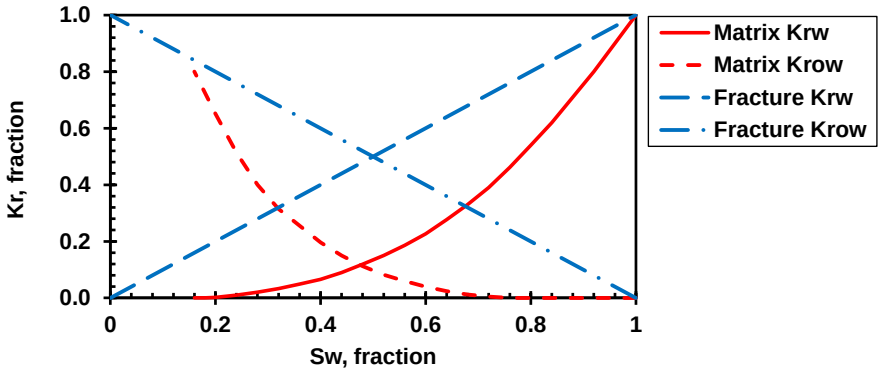

(a)

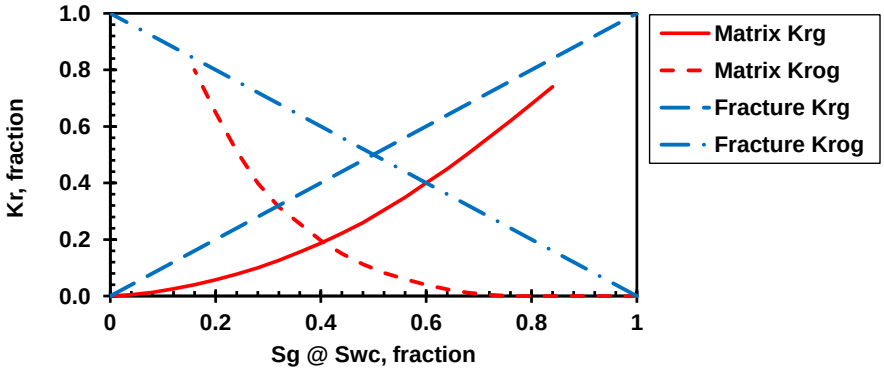

(b)

Fig. 5.11—Rock-fluid functions used in this study. (a) Oil and water relative permeability in the matrix and fractures; (b) Oil and gas relative permeability in the matrix and fracture; (c) Oil-water and gas-oil capillary pressure curves. Oil-gas capillarity is assumed to be zero.

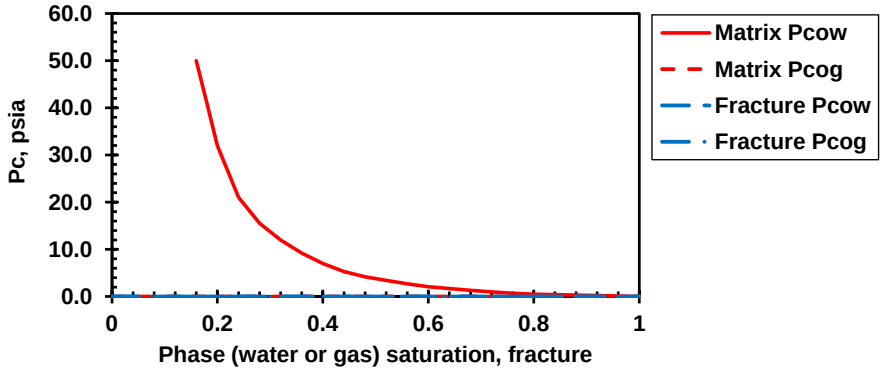

(c)

Fig. 5.11—Continued.

The fluid compositional properties are from **Table 5.2**. In this case the initial reservoir pressure ($5{,}000\ psia$) is lower than the fluid bubble point pressure ($5{,}557.517\ psia$), such that there are always three mobile phases, including oil, gas and water during the whole depletion process in the reservoir.

The Jacobian systems for those two approaches are shown in **Fig. 5.12**. In both approaches fracture domain is discretized first, followed by matrix domain (**Fig. 5.12(a)**). **Fig. 5.12(b)** is the Jacobian for EDFN, and **Fig. 5.12(c)** is the Jacobian for EDFM. In both Jacobian systems there is an unstructured diagonal block at the upper left, caused by the irregular fracture-to-fracture connections; there is a structured diagonal block at the lower right block, induced by the structured intra-matrix connections. The off-diagonal blocks are caused by matrix-to-fracture connections.

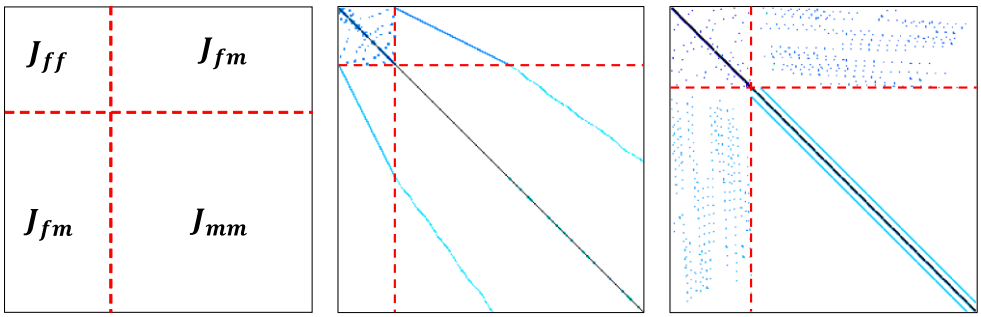

(a) (b) (c)

Fig. 5.12—Jacobian matrix for two different models at the same newton: (a) structure of Jacobian; (b) Jacobian of EDFN; (c) Jacobian of EDFM.

From **Fig. 5.12** we can observe that the Jacobian of EDFN is much simpler than that of EDFM. To better interpret this, their discretization difference is illustrated in **Table 5.4**. Through comparison it shows EDFN has much lower grid and connection number than those of EDFM, and this can be attributed to the optimized fracture and 1D matrix discretization in EDFN. As a result, the Jacobian of EDFN is much smaller than that of EDFM. This greatly reduces the computational burden on linear solver and thus improves efficiency when EDFN is applied.

Table 5.4—Comparison of discretization of EDFN and EDFM Models

	Grid NO.	Connection NO.	Jacobian dimension	Jacobian nonzeros
EDFN	490	579	3,431 × 3,431	16,302
EDFM	1,694	3,312	11,859 × 11,859	71,794

5.2.3.1 No Capillary Pressure

Here the capillary pressure in the matrix is firstly ignored. The results of EDFN and EDFM models are plotted in **Fig. 5.13**, and their differences based on L-2 norm are reported in **Table 5.5**.

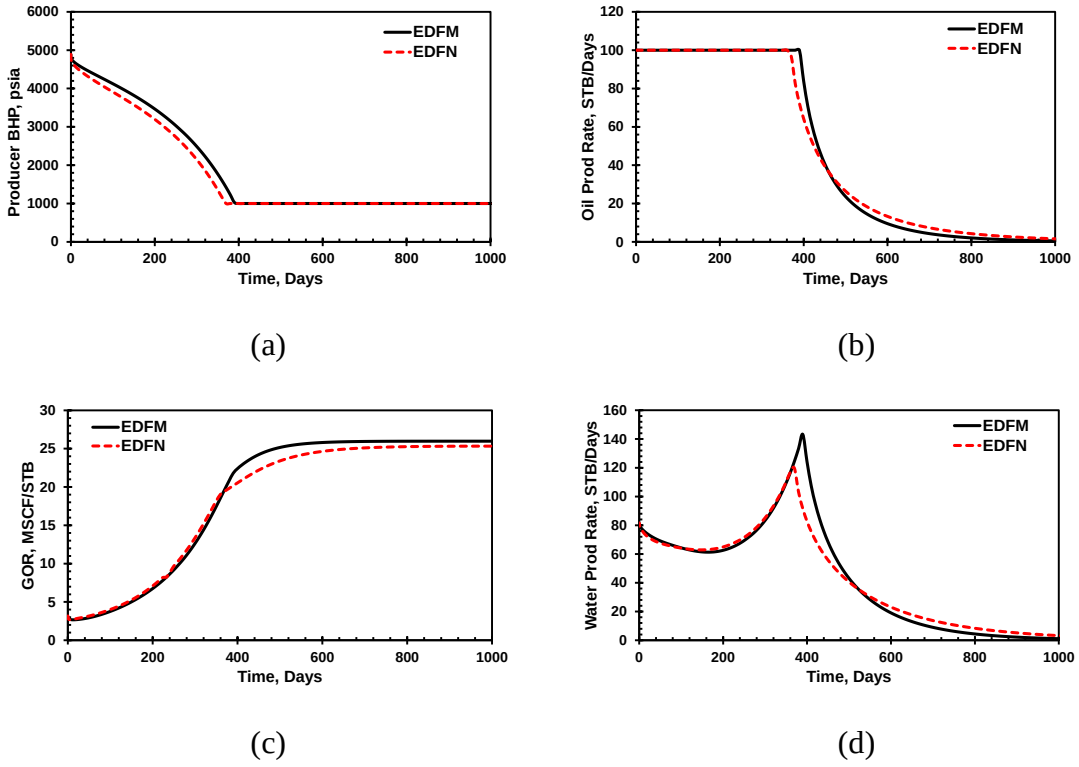

Fig. 5.13—Results for the case without considering capillarity pressure. (a) bottom-hole pressure; (b) oil production rate; (c) production gas-oil ratio (GOR); (d) water production rate; (e) reservoir average oil saturation; (f) reservoir average gas saturation.

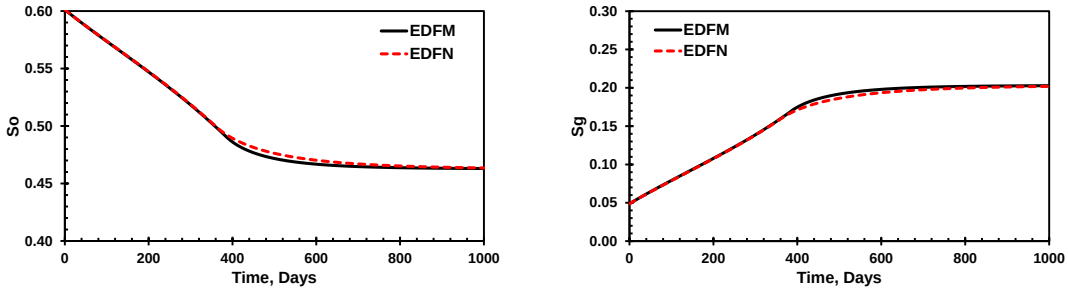

(e) (f)

Fig. 5.13—Continued.

Table 5.5—Difference between EDFN and EDFM Models

BHP	Oil rate	GOR	Water rate	Average S_o	Average S_g
5.22%	5.73%	4.44%	13.52%	0.41%	1.49%

Those two models provide very consistent results in terms of producer BHP, oil rate, GOR, average oil and gas saturation. The main difference lies in water rate. Specifically the EDFN model has a lower peak water rate than that of the EDFM model. In the EDFM model matrix is globally connected, while in the EDFN model matrix is locally connected to fractures (**Fig. 5.9**). Therefore, EDFM is a Dual-Porosity Dual-Permeability Model, while EDFN is a Dual-Porosity Single-Permeability Model. Besides, in EDFM it is extremely difficult to logarithmically refine the matrix grid surrounding inclined fractures, but this is what we adopt in the EDFN model. All those factors combined together induce that the EDFM model can maintain longer constant oil rate and lower peak water rate in its matrix block.

5.2.3.2 Considering Capillary Pressure

Further, water-oil capillary pressure in the matrix (**Fig. 5.11(c)**) is introduced in this case. The results of EDFN and EDFM models are presented in **Fig. 5.14**, and their differences are illustrated in **Table 5.6**.

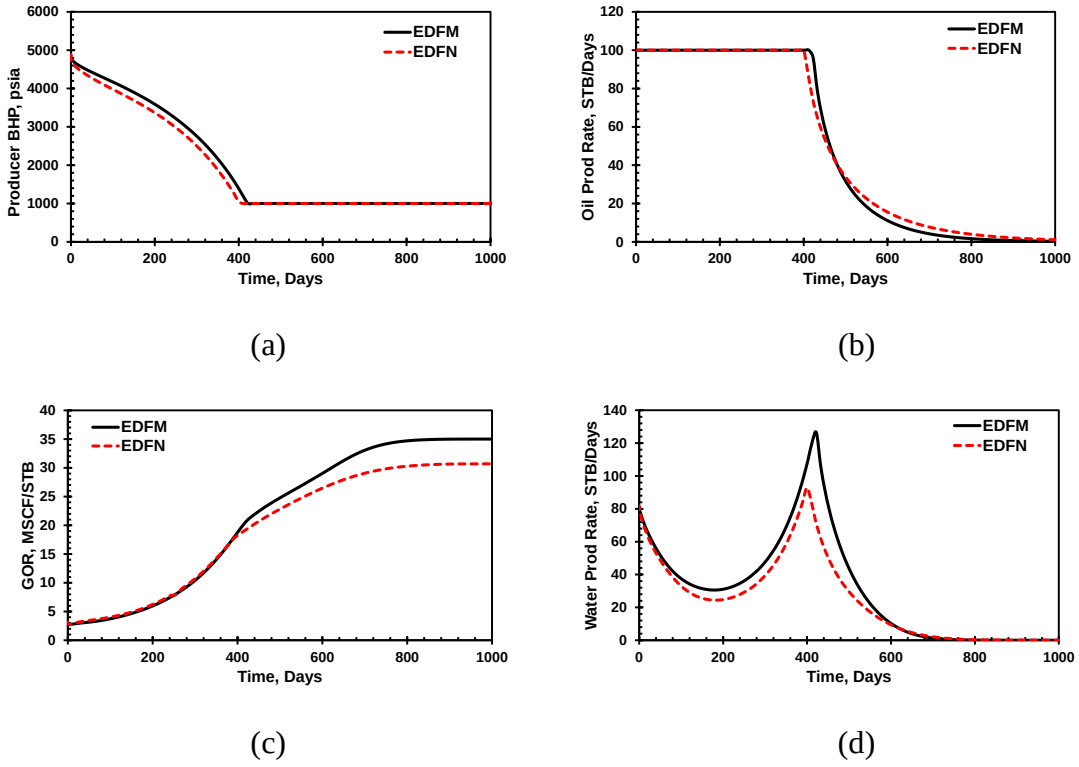

Fig. 5.14—Results for the case with considering capillarity pressure. (a) bottom-hole pressure; (b) oil production rate; (c) production gas-oil ratio; (d) water production rate; (e) reservoir average oil saturation; (f) reservoir average gas saturation.

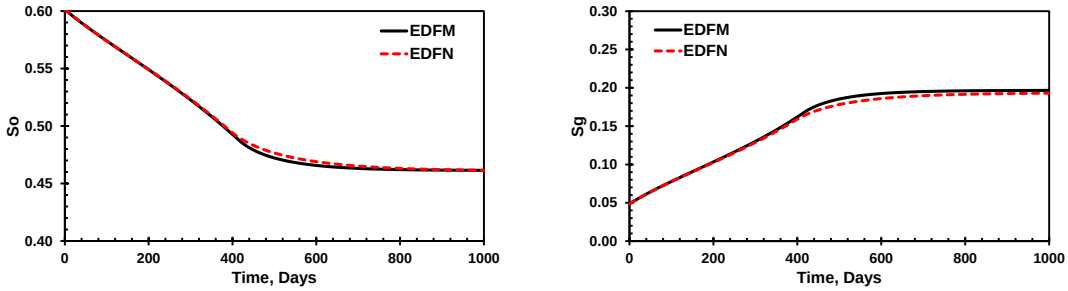

(e) (f)

Fig. 5.14—Continued.

Table 5.6—Error of EDFN model compared to EDFM model

BHP	Oil rate	GOR	Water rate	Average S_o	Average S_g
5.62%	6.08%	11.15%	22.58%	0.33%	2.43%

It shows that both models still have very consistent results (**Table 5.6**). The most significant difference of those two models lies in water producing rate, which is the same as what we observe in this case ignoring water-oil capillary pressure in the matrix domain. This can be caused by different grid configurations: EDFM here uses uniform grid refinement in matrix domain (**Fig. 5.10(c)**) and EDFN actually uses logarithmic grid refinement in each coarse matrix block (**Fig. 5.8**). Besides, in the matrix water is wetting phase, so the existence of water-oil capillary pressure actually retards the water flux from matrix to fracture. As a result, it is reasonable to see more difference of water producing rate with considering capillary pressure.

5.3 Performance of Compositional Space Preconditioned VLE

The compositional space preconditioned VLE/flash algorithms proposed in Section 4.3.2.2 are evaluated to demonstrate their performance, and two subsections are discussed, including fixed fluid composition and sharply varying fluid composition with CO_2 injection.

5.3.1 Fixed Fluid Composition

The workflow of VLE calculation for fixed fluid composition is validated using six different fluid samples from Li and Firoozabadi (2012). The samples are Acid Gas, Oil B, Maljamar Reservoir Oil, Maljamar Separator Oil, Bob Slaughter Block Oil, and North Ward Estes Oil, respectively, in which CO_2 is mixed with hydrocarbon components. Using two-phase flash calculation as an example, the mole fractions of CO_2 are a little different from the original data to avoid three-phase region. Fluid composition, temperature and corresponding bubble point pressure defining those fluid samples are presented in **Table 5.7**. Other PVT parameters are the same as in Table 3 to 8 from Li and Firoozabadi (2012).

The 2D compositional spaces are firstly constructed. Pressure decreases from bubble point pressures p_b to 50 psia with an average pressure interval of 5 psia for each compositional space. With the given composition and temperature in **Table 5.7**, VLE calculation is conducted to build the space database. Then dynamic VLE calculation based on initial guess interpolated from compositional space can be performed conveniently.

Table 5.7—Fluid composition and saturation pressure of six fluid samples (Li and Firoozabadi 2012)

	Acid Gas	Oil B	Maljamar Reservoir Oil	Maljamar Separator Oil	Bob Slaughter Oil	North Ward Estes Oil
CO_2	0.19242	0.66914	0.16667	0.65517	0.34099	0.44635
N_2	0.19314	0.00161	-	-	-	-
H_2S	0.05404	-	-	-	-	-
C_1	0.18858	0.05454	0.24492	-	0.05872	0.11298
C_2	0.29026	0.01348	0.08492	-	-	-
C_3	0.08156	0.00994	0.06958	-	-	-
iC_4	-	0.00120	-	-	-	-
nC_4	-	0.01101	0.02758	-	-	-
iC_5	-	0.00529	-	-	-	-
nC_5	-	0.00719	-	-	-	-
C_{5-7}	-	-	0.10033	0.08117	-	-
C_6	-	0.01111	-	-	-	-
C_{8-10}	-	-	0.13175	0.11362	-	-
C_{11-14}	-	-	0.06858	0.05907	-	-
C_{15-20}	-	-	0.04400	0.03790	-	-
C_{21-28}	-	-	0.02300	0.01979	-	-
C_{29+}	-	-	0.03867	0.03328	-	-
PC_1	-	0.06067	-	-	0.44179	0.06584
C_{29+}	-	-	0.03867	0.03328	-	-
PC_1	-	0.06067	-	-	0.44179	0.06584
PC_2	-	0.05400	-	-	0.15849	0.08280
PC_3	-	0.04193	-	-	-	0.15974
PC_4	-	0.03192	-	-	-	0.08313
PC_5	-	0.01938	-	-	-	0.04915
PC_6	-	0.00761	-	-	-	-
n_h	6	16	11	7	4	7
T, °F	-137.83	94.01	89.96	89.96	105.00	82.99
p_b, $psia$	804.36	1225.25	1576.187	944.289	890.123	1286.696

Three approaches are used for flash calculation for comparison: (a) **WCIG + SSI + NR**, in which flash calculation (NR+SSI) is based on initial guess of K-values from

Wilson's correlation; (b) **CSIG + SSI + NR**, in which flash calculation (NR+SSI) is based on initial guess of K-values and vapor mole fraction from 2D compositional space; (c) **CSIG + RRP + NR**, in which flash calculation (NR only) is based on initial guess of K-values from 2D compositional space and vapor mole fraction from a Rachford-Rice preconditioning.

For those three cases, the same VLE convergence criteria are applied. Equation (5.1) (Schlumberger 2012) is used as SSI error for each iteration. SSI is switched to NR if the error is smaller than 10^{-2} or number of iterations is more than 2. In NR, the L-2 norm of global phase equilibrium residual vector $\left[R_{f,1}, R_{f,2}, \cdots, R_{f,n_c}, R_r\right]^T$ is used to evaluate the error with an ultimate convergence tolerance of 10^{-9}. The total number of flash iterations is the sum of SSI iteration and NR iteration. Since this parameter is independent of implementation platforms and languages, it is used to evaluate the performance of our algorithms.

$$\sum_{i=1}^{n_h} \left(\frac{\hat{f}_i^l}{\hat{f}_i^v} - 1\right)^2 < \varepsilon \tag{5.1}$$

To show the broad application of the workflow for two-phase flash calculation, 100 random pressures between $100\ psia$ and bubble point pressure of each sample are selected to test the flash algorithms. The flash iterations of different samples are presented in **Fig. 5.15 (a)** to **(f)**, representing Acid Gas, Oil B, Maljamar Reservoir Oil, Maljamar Separator Oil, Bob Slaughter Oil and North Ward Oil, respectively.

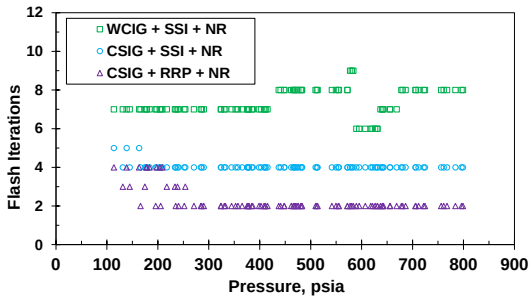

(a) Acid Gas

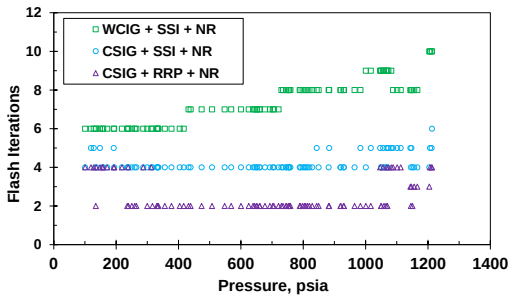

(b) Oil B

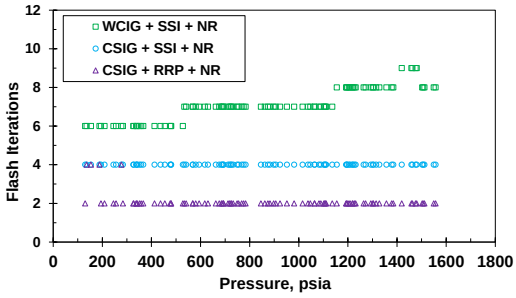

(c) Maljamar Reservoir Oil

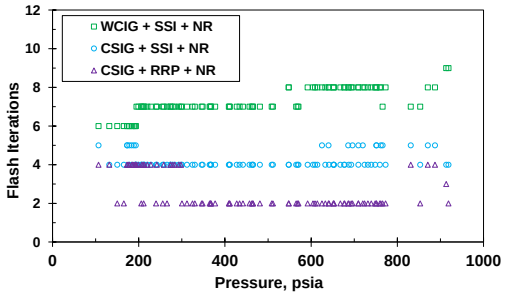

(d) Maljamar Separator Oil

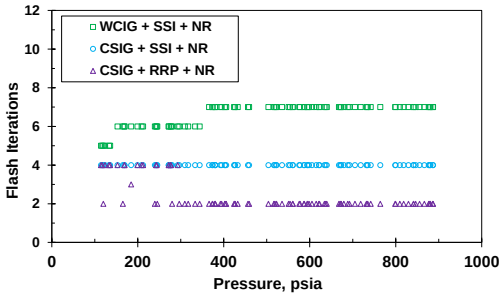

(e) Bob Slaughter Block Oil

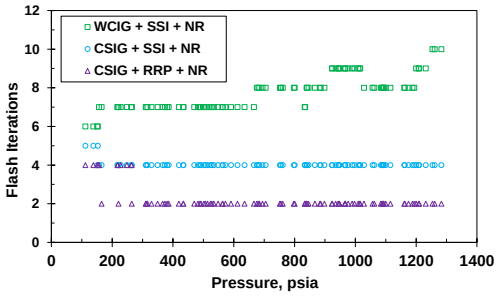

(f) North Ward Estes Oil

Fig. 5.15—Flash iteration for different fluid samples based on: (1) WCIG + SSI + NR (green square markers), (2) CSIG + SSI + NR (blue circle markers), (3) CSIG + RRP + NR (purple triangular markers), and 100 different pressure conditions randomly from range $[100, p_b]$ $psia$ for each fluid sample.

In **Fig. 5.15**, 1800 flash calculations (300 per fluid sample) are performed and converged, indicating successful implementation of the proposed flash algorithms.

Together with **Table 5.8**, the results show that WCIG + SSI + NR converges with the highest number of flash iterations (green square markers), followed by CSIG + SSI + NR and CSIG + RRP + NR that costs the lowest number of flash iterations. Those performances using different fluid samples soundly support that the initial guesses of K-values and vapor mole fraction interpolated from 2D compositional space are very close to the accurate results after reaching phase equilibrium.

Table 5.8—Average flash iterations of different fluid sample based on different approaches

	Average Flash Iterations		
Fluid Sample	**WCIG + SSI + NR**	**CSIG + SSI + NR**	**CSIG + RRP + NR**
Acid Gas	7.34	4.03	2.36
Oil B	7.41	4.22	2.55
Maljamar Reservoir Oil	7.10	4.00	2.08
Maljamar Separator Oil	7.24	4.20	2.61
Bob Slaughter Oil	6.65	4.00	2.37
North Ward Estes Oil	7.75	4.03	2.22

What's more, CSIG + RRP + NR on average costs about half iterations of CSIG + SSI + NR and one third iterations of WCIG + SSI + NR. In CSIG + RRP + NR, an evaluation of the interpolated vapor mole fraction through Rachford-Rice Equation becomes very helpful such that the SSI step can even be bypassed. Even though the interpolated K-values and vapor more fraction from the discrete compositional space may

not exactly satisfy the material balance and fugacity equilibrium, a direct evaluation of Rachford-Rice Equation can readily synchronize the vapor mole fraction with the interpolated K-values. This simple remediation improves the quality of the initial guess, allowing that mere NR can provide convergence.

In addition, it is also interesting to note in **Fig. 5.15** that the convergence is generally faster at low pressure than at high pressure for WCIG + SSI + NR. This is attributed to the fact that initial guess of K-values based on Wilson's correlation is not accurate at higher pressures, requiring more iterations to converge.

5.3.2 Sharply Varying Fluid Composition with Gas Injection

Flash calculation for sharp varying fluid composition with CO_2 injection is investigated using the North Ward Estes Oil as listed in **Table 5.7**. CO_2 mole fraction increases from 0.01 to 0.8 because of massive injection into the subsurface oil reservoir. The mole fractions of the other six components ($C_1, PC_1, PC_2, PC_3, PC_4$ and PC_5) in the fluid are normalized based on the original mole proportions for those components in the mixture. As shown in **Fig. 4.5** and **4.6**, the bubble point pressure increases and the K-values change nonlinearly during the CO_2 injection process, and thus here CO_2 is defined as the Pseudo Key Component (PKC).

Using the approach introduced in Section 4.3.2.2.2, a 3D compositional space is constructed defining $p - z_{CO_2} - K_i$ and $p - z_{CO_2} - f_v$ relationships. More specifically, under each discrete z_{CO_2}, pressure changes from individual bubble point pressure p_b to a low pressure (50 psia) with average pressure interval of 5 psia. z_{CO_2} changes from 0.01 to

0.8 with interval of 0.01. The $p - z_{CO_2} - f_v$ relation is plotted in **Fig. 5.16**, in which the color bar represents the magnitude of vapor mole fraction f_v. The curve of $f_v = 0$ is the liquid-vapor phase boundary, corresponding to the bubble point pressure curve in **Fig. 4.5** as well. As pressure increases and more CO_2 is dissolved into the mixture, vapor mole fraction increases and the mixture reaches close to miscible condition. The $p - z_{CO_2} - K_i$ relationship for each component is also established.

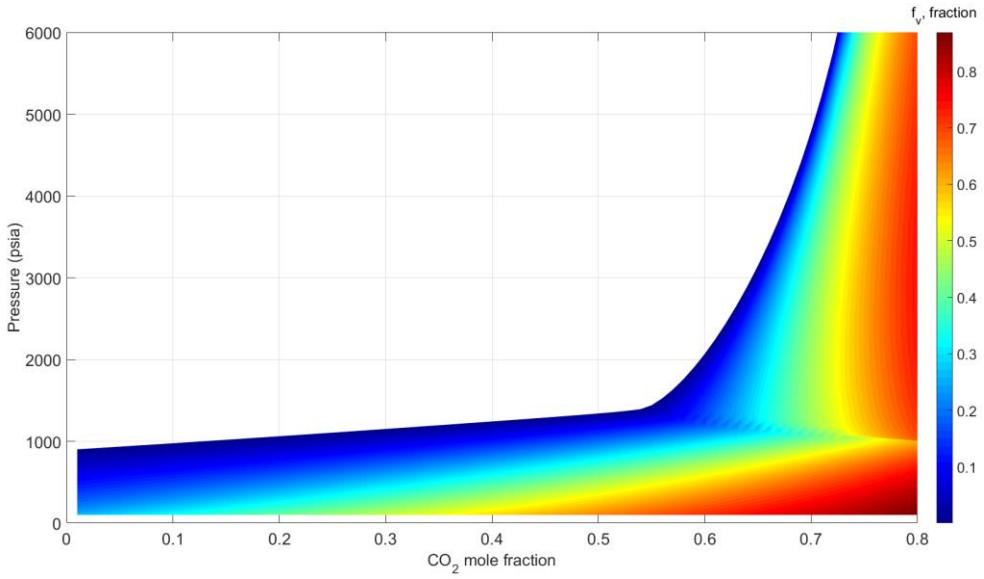

Fig. 5.16—Vapor mole fraction for CO_2 mixing with North Ward Estes Oil at 82.99 °F

The 3D compositional space constructed above defines phase equilibrium of North Ward Estes Oil with varying CO_2 mole fractions and pressure conditions. Following the workflow presented in **Fig. 4.7**, the space is further applied to interpolate K_i and f_v for flash calculations. As shown in **Table 5.9** and **Fig. 5.17**, 12 CO_2 mole fractions and

pressure conditions are prepared to validate the workflow, which covers a large range of conditions. Especially, Case 9 to 12 already reach to the miscible condition.

Table 5.9—12 CO_2 mole fractions and pressure conditions of North Ward Estes Oil

Case	CO_2 mole fraction	Pressure (psia)
1	0.010	400
2	0.190	750
3	0.310	820
4	0.430	860
5	0.550	900
6	0.589	1700
7	0.615	2000
8	0.641	2400
9	0.667	2700
10	0.683	2900
11	0.707	3300
12	0.734	3600

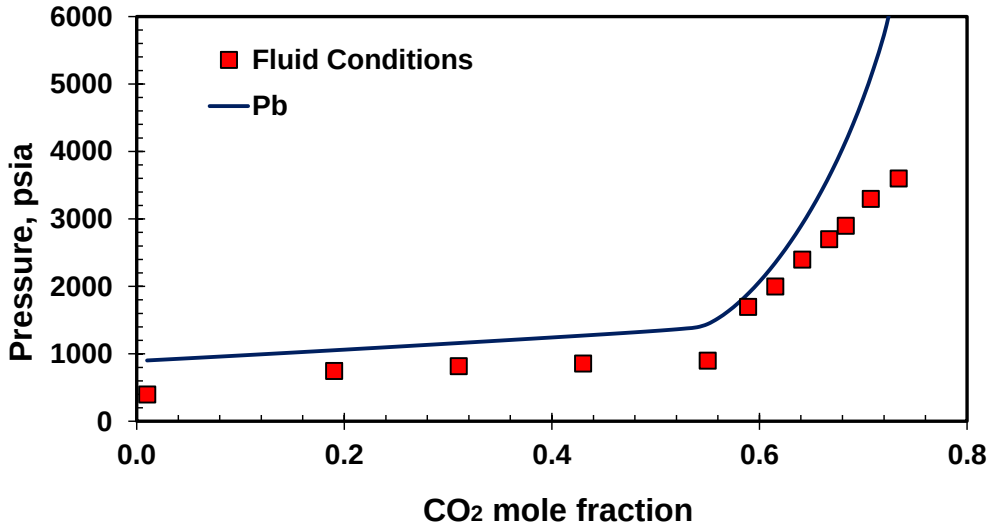

Fig. 5.17—CO_2 mole fractions and pressure conditions of North Ward Estes Oil

Three approaches are applied to perform the flash calculation, namely (a) **WCIG + SSI + NR**, (b) **CSIG + SSI + NR** and (c) **CSIG + RRP + NR**, which are the same as we defined in the previous section. Since those varying fluid composition are challenging for WCIG + SSI + NR, the criteria for switching from SSI to NR is set as iteration count larger than 100 or error smaller than 10^{-5}. For CSIG + SSI + NR, the criteria for switching from SSI to NR is still the iteration count larger than 2 or error smaller than 10^{-2} with the ultimate convergence criteria for all flash approaches as error smaller than 10^{-9}. Since some cases using WCIG + SSI + NR fail to converge, the iteration count of NR and SSI are both reported and their summation are the total number of iterations of flash calculation.

Fig. 5.18 shows the performance for flash calculation based on Wilson's correlation. Based on initial guess of K-values from Wilson's correlation, at low pressure scenarios (Case 1 to 5) it works well with the average flash iteration 10.8 (7.8 SSI iterations plus 3 NR iterations). In Case 6 to 8, NR fails because the VLE Jacobian system becomes very singular and cannot be solved with physical solutions. Thus after the first NR iteration flash is forced back to SSI. The total flash iterations after SSI convergence for those three cases are 319.7 on average. For the last four cases (Case 9 to 12), the initial guesses from Wilson's correlation are not reliable at all, since it is determined as single phase after the first iteration of SSI.

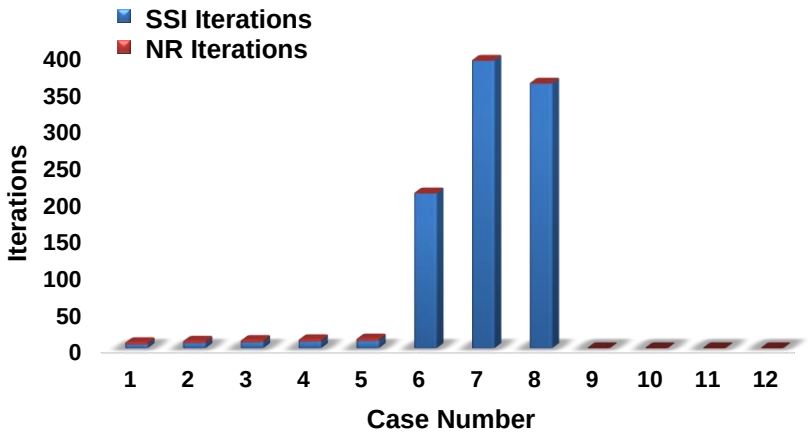

Fig. 5.18—Flash performance for 12 cases in Table 5.9 using WCIG + SSI + NR

The initial guess interpolated from the 3D compositional space is expected to reduce the number of flash iterations significantly. **Fig. 5.19** presents the number of iterations for flash calculation (SSI + NR) based on initial guess from 3D compositional space. All of the 12 cases by this approach are converged very efficiently. Among those cases, the average total flash iterations are 6.67 including 1.67 SSI iterations and 5.0 NR iterations. Especially for challenging Cases 6 to 12, the flash performance based on this method is much more superior to that based on WCIG + SSI + NR. As a result, this 3D compositional space with pseudo key component definition is very helpful to provide excellent initial guesses for K-values and vapor mole fraction towards sharply varying fluid composition scenario.

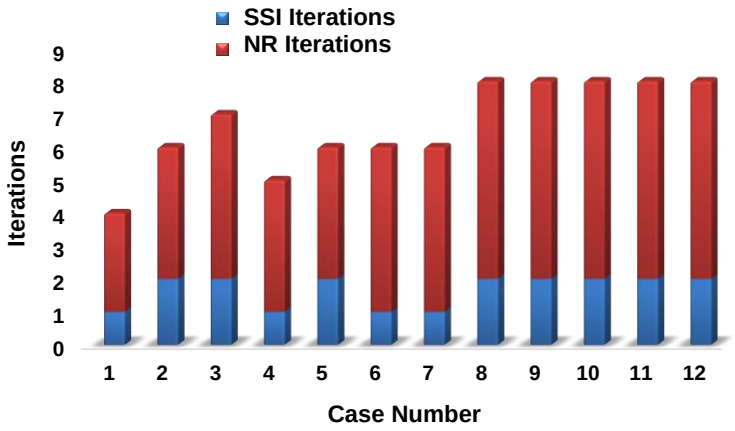

Fig. 5.19—Flash performance for 12 cases in Table 5.9 using CSIG + SSI + NR, with 6.67 flash iterations and 5 NR iterations on average

Finally, the Rachford-Rice preconditioning procedure is applied to skip SSI with results shown in **Fig. 5.20** for the 12 cases. Since only NR is performed, the number of flash iterations is in fact equal to the number of NR iterations. The CPU time ratios of CSIG +SSI + NR and CSIG + RRP + NR for the 12 cases are plotted in **Fig. 5.21**. On average, 1.5 times of speedup is achieved using CSIG + RRP +NR in comparison with CSIG + SSI + NR. In **Fig. 5.22**, the CPU times for the 3 methods are further compared. Clearly, compared with WCIG + SSI + NR, the improvement is significant. Even though the PKC mole fraction varies, the 3D compositional space defines a highly converged nonlinear space for multivariable interpolation to provide initial guess of K-values and vapor mole fraction. Further, a Rachford-Rice evaluation is used to synchronize vapor mole fraction with K-values, moving the phase equilibrium residuals even closer to zero.

As a result, NR is generally sufficient by itself to efficiently complete the flash calculation, even for challenging fluid systems.

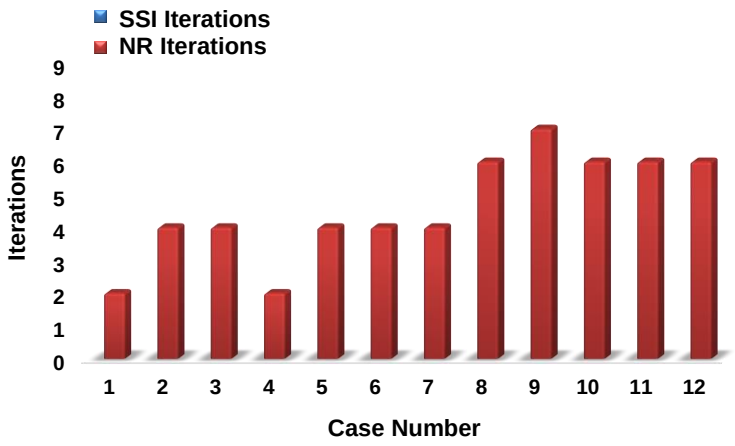

Fig. 5.20—Flash performance for 12 different cases in Table 5.9 based on CSIG + RRP + NR, with 4.58 NR iterations on average

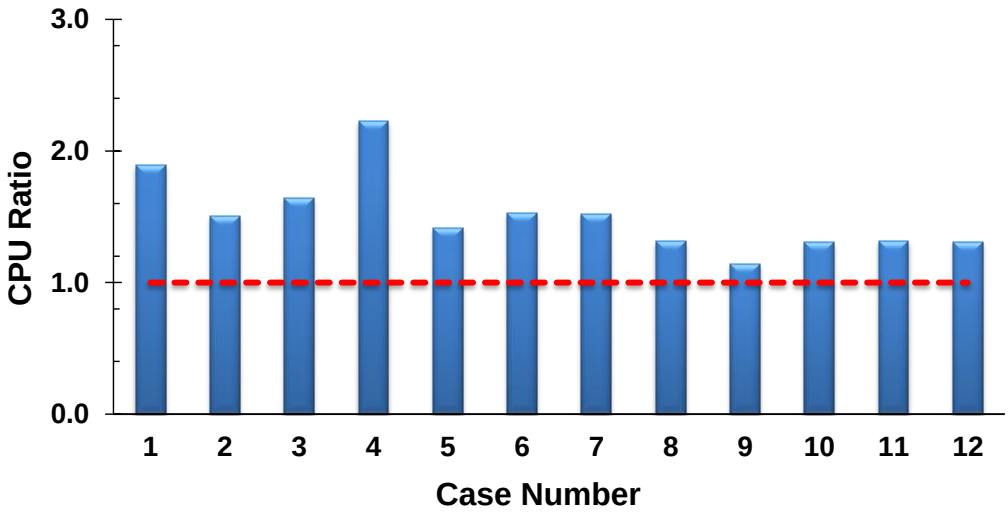

Fig. 5.21—CPU time ratio of CSIG + SSI + NR to CSIG + RRP + NR (red dash line: base line for no speedup)

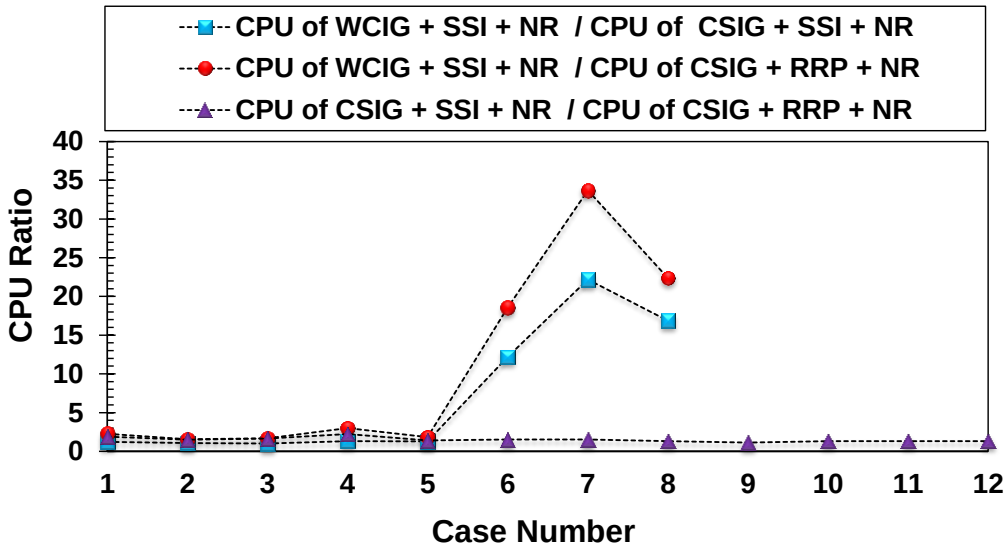

Fig. 5.22—CPU time ratios for the 3 methods. WCIG + SSI + NR fails in Case 9 to 12

5.4 Summary

In this chapter, GURU is firstly validated with Eclipse 300 by a 3D inverted five-spot model with a water injector and an oil producer. It is demonstrated that GURU provides very well-matched results with Eclipse 300. Besides, phase segregation because of gravity in the 3D model are accurately captured in GURU as well.

Secondly, different unstructured fracture models including EDFN and EDFM are run through GURU to simulate multiphase flow in a reservoir with non-orthogonal fractures. It shows that EDFN has superiority in terms of Jacobian dimension. Those two models provide very consistent results with or without considering capillary pressure in the matrix. On the other hand, the difference of their results is caused by different model

configurations. Specifically, EDFN is a theoretically Dual-Porosity Single-Permeability Model, but EDFM is a Dual-Porosity Dual-Permeability Model. Besides, in those two models the matrix refinement method is different.

Finally, the proposed VLE workflows based on compositional space in the previous chapter are validated by different fluid samples. The compositional spaces constructed are actually discrete spaces of converged phase equilibria. Initial guesses of K_i and f_v values for flash calculations in other conditions can be interpolated from those spaces. It is found that the compositional space provides excellent initial guess for flash calculation. Specifically for the challenging CO_2 injection reservoir system, the initial guess for flash calculation interpolated from the 3D compositional space provide excellent convergence. In addition, an evaluation of Rachford-Rice equation after interpolation helps to synchronize f_v with K_i of the initial guess values. This remediation improves the performance significantly such that SSI can be bypassed, reducing the total flash iterations in further.

CHAPTER VI

MODELING SHALE GAS STORAGE AND TRANSPORT

In the previous chapters, a general Multi-Porosity Model has been proposed to simulate reservoirs with multiple porosity systems, and an unstructured reservoir simulator GURU has been developed for compositional simulation. In this chapter, through leveraging those two tools, the connectivity and mechanisms in shale gas reservoirs are investigated. Besides, through upscaling from an Enhanced Discrete Fracture Network (EDFN) Model, the heterogeneous secondary fracture network inside the Stimulated Reservoir Volume (SRV) is characterized and its impact on shale gas production is also evaluated.

6.1 Workflow from EDFN to Multi-Porosity Modeling

After hydraulic fracturing, a complex fracture network is generated by the interaction of hydraulic fractures and secondary fractures (CuiYang et al. 2016; CuiZhu et al. 2016; McLennan and Potocki 2013). The reservoir volume associated with the fracture network corresponds to the Stimulated Reservoir Volume (SRV), and beyond this region shale matrix is basically undamaged(Vera and Shadravan 2015). The micro-seismic fracture mapping data shows that the micro-seismic fracturing events in SRV were mostly located near the center of hydraulic fracture and wellbore (Fisher et al. 2004; Mayerhofer et al. 2010). Suliman et al. (2013) estimated SRV as a collective system of fractures and shattered matrix blocks. They classified the SRV into Flush, Conductive and Hydraulic

SRV depending on the micro-seismic density and the connectivity of every grid block in the reservoir model. Therefore, the fracture distribution at the vicinity of horizontal wellbore and perforated stages tends to be non-uniform such that the reservoir-scale impact of the fracture network on gas production is not likely to be homogeneous.

Discrete fractures approaches bring the flexibility to handle the fracture geometric details. Discrete Fracture Model (DFM), based on unstructured grid discretization, can explicitly describe the effect of fracture geometric details (Mi et al. 2014; Sun et al. 2012; Sun et al. 2014a; Sun and Schechter 2014b; Yu et al. 2011), and naturally captures the complex flow phenomena occurring in the vicinities of those sparse fractures. However, it is still not practical for field-scale studies, since unstructured gridding becomes challenging and computationally expensive when a large number of fractures in complex distribution are present (Li et al. 2015). Further, a simplified model of Enhanced Discrete Fracture Network (EDFN) Model was developed, which can decrease the number of grid blocks (Mi, L. et al. 2016) and computational time (Basquet et al. 2005; Sarda et al. 2001), while it still keeps the advantages of the DFM. Therefore, in this work the EDFN approach developed by Mi, L. et al. (2016) is used to capture the fracture geometric details in terms of sector models inside SRV. Further, the heterogeneous impact of secondary fracture distribution on matrix-to-fracture fluid transfer is revealed by shape factor distribution upscaled from EDFN sector models.

The developed compositional reservoir simulator, GURU, enables to consider flexible unstructured grid geometry. Therefore, the EDFN Model and the general Multi-Porosity Model can be preprocessors for grid discretization, and be connected with GURU

for reservoir simulation. Besides, with the occurrence of nano-pores in shale matrix, GURU comprehensively considers the interaction between pore-wall and gas molecules via gas slippage and Knudsen diffusion, and gas adsorption/desorption on the pore-wall of organic matrix is modeled by extended Langmuir adsorption isotherm.

Therefore, a workflow can be established based on GURU, EDFN, and Multi-Porosity Model, as shown in **Fig. 6.1**. EDFN Sector Models with detailed fracture geometry are run through GURU. Therefore, the heterogeneous impact of fracture network is upscaled from EDFN sector models depending on the fracture intensity in different regions, and it is numerically represented by heterogeneous shape factor distribution. Further, in Multi-Porosity Model those different porosity systems in shale are fully characterized with no assumption of flow mode since arbitrary connection topology is allowed, and it is connected with GURU for flow simulation. Besides, within GURU the non-Darcy flow physics is captured in those tight matrix porous media.

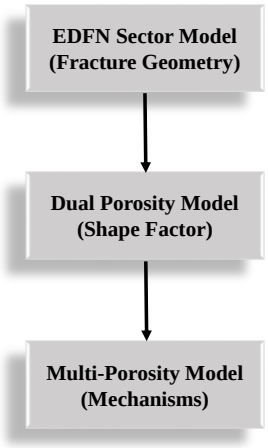

Fig. 6.1—Workflow from EDFN to Multi-Porosity Model

6.2 Enhanced Discrete Fracture Network (EDFN) Model Upscaling

In shale reservoirs, secondary fractures near each hydraulic fracture stage is not evenly distributed. A uniform characterization of the secondary fracture zone is thus not physically reasonable. We further subdivide those zones into different small sector models, in each of which the fracture distribution is assumed to be approximately even. The original characterization of fracture network now becomes subtasks to characterize those sector models with different fracture distribution. We first present the process to upscale a sector model with EDFN (Mi, L. et al. 2016) into a Dual-Porosity Single-Permeability Model. Based on water imbibition experiments, Kazemi et al. (1992) proposed a general formula to calculate shape factor (Equation (6.1)),

$$\sigma = \frac{1}{V_m}\sum_{i=1}^{I}\frac{A_i}{d_i} \tag{6.1}$$

where σ is shape factor; V_m is bulk volume for matrix block, A_i represents the exposed fracture surface area i to matrix block, d_i equals to the length from the matrix block center to fracture surface i, and I is the total number of exposed fracture surfaces.

As stated by Gilman (2003), this formula is capable of upscaling from complex fracture network (DFN model) to equivalent Dual-Porosity Models. In this work, the EDFN approach naturally includes a matrix partition based on local fracture segments and iso-pressure surfaces (Mi, Lidong et al. 2016; Mi, L. et al. 2016). Based on this optimized matrix partition, the parameters in Equation (6.1) can be easily calculated, and thus a shape factor for an EDFN sector model can be extracted.

6.2.1 Upscale Dual-Porosity Model from EDFN Model

As shown in **Fig. 6.2(a)**, a sector model is presented with 40 evenly distributed fractures. A producer is located at lower right corner. The matrix is partitioned based on iso-pressure surfaces and fracture segments (**Fig. 6.2(b)**). This partition method is optimized such that it can be directly applied to calculate shape factor for the sector model based on Equation (6.1), which is calculated to be 5.345 ft^{-2}. The upscaled Dual-Porosity Single-Porosity Model is shown in **Fig. 6.3**, with two domains representing matrix and fracture systems, respectively. Detailed parameters are shown in **Table 6.1**.

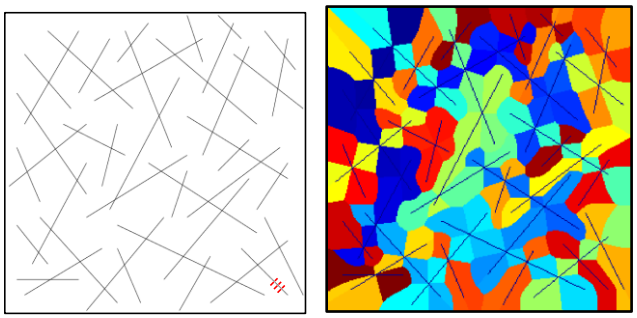

(a) (b)

Fig. 6.2—(a) 40 fractures distributed in a sector model (red lines: well); (b) EDFN model

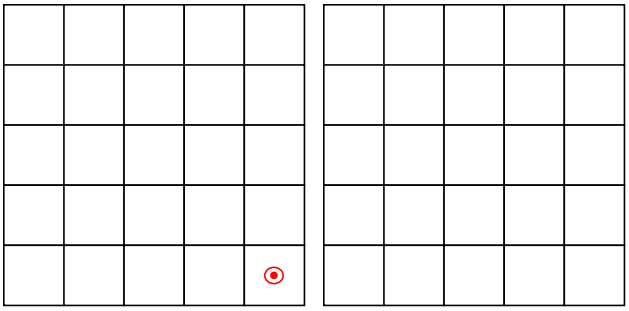

(a) (b)

Fig. 6.3—Dual-Porosity Single-Permeability Model: (a) fracture domain, red circle represents well perforation; (b) matrix domain.

Table 6.1—Basic parameters to EDFN and upscaled DPSP models

Sector dimension (ft^3)	$20 \times 20 \times 100$
EDFN Model	
Number of fractures	40
Matrix porosity	0.044
Matrix permeability (nD)	50
Matrix water saturation	0.16 (irreducible)
Fracture porosity	1.0
Fracture conductivity ($mD-ft$)	5.0
Fracture water saturation	0.0
DPSP Model	
Grid dimensions	$5 \times 5 \times 1$
Grid spacing (ft)	$\Delta x = \Delta y = 4, \Delta z = 100$
Matrix porosity	0.044
Matrix permeability (nD)	50
Matrix water saturation	0.16 (irreducible)
Fracture porosity	0.00606185
Fracture conductivity ($mD-ft$)	5.0
Fracture water saturation (v/v)	0.0
Shape factor from upscaling (ft^{-2})	5.345
Reservoir conditions for all models	
Initial pressure ($psia$)	5400
Producer pressure ($psia$)	500 for $t > 0$
Initial temperature (°F)	200 for $t > 0$
Fluid in the reservoir	Gas and irreducible water
Gas composition	5.0 $mol\%$ CO_2 and 95.0 $mol\%$ CH_4

Both the EDFN and DPSP Models are run through GURU, and then the gas rate and average reservoir pressure for those two different models are compared. As shown in **Fig. 6.4**, both models provide very well-matched results. Their gas rate difference is 1.96% and average reservoir pressure difference is 0.76%. Therefore, with non-orthogonal fracture distribution in this sector model, the upscaled Dual-Porosity Model is equivalent to detailed EDFN model honoring fracture geometries.

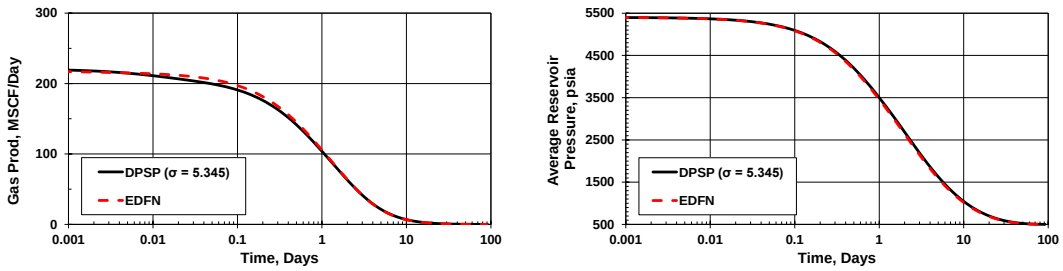

(a) (b)

Fig. 6.4—Result comparison between EDFN and DPSP. (a) gas rate, difference between the two models: 1.96%; (b) average reservoir pressure, difference between the two models: 0.76%.

6.2.2 Upscaling Sector Models with Different Fracture Distribution

Sector models with different fracture configuration are established to upscale the shape factors for Dual-Porosity or Multi-Porosity models. The size for all sector models is $20ft \times 20ft \times 100\ ft$ in this chapter. Those sectors represent different regions near hydraulic fracture stages. Within each sector model, the fracture distribution is assumed to be even. Cases with different discrete fracture numbers are investigated, shown in **Fig. 6.5(a)** to **(f)**, with 5, 10, 20, 30, and 40 fractures, respectively.

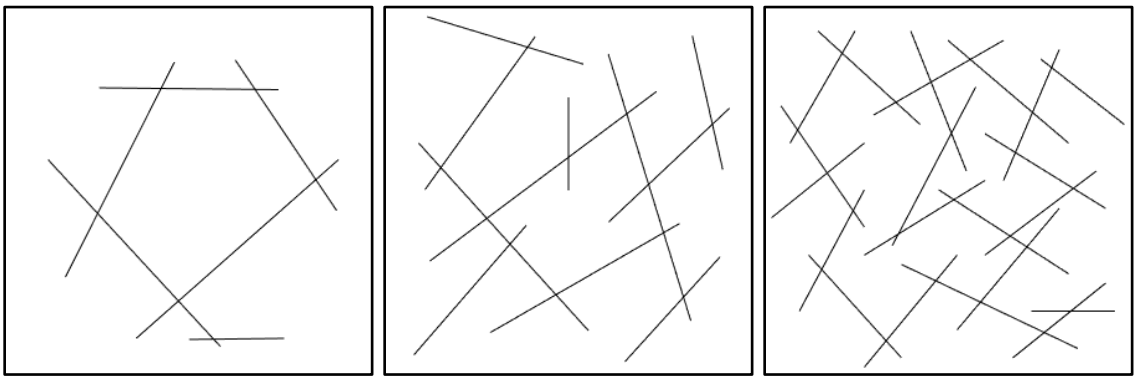

(a) 5 fractures (b) 10 fractures (c) 20 fractures

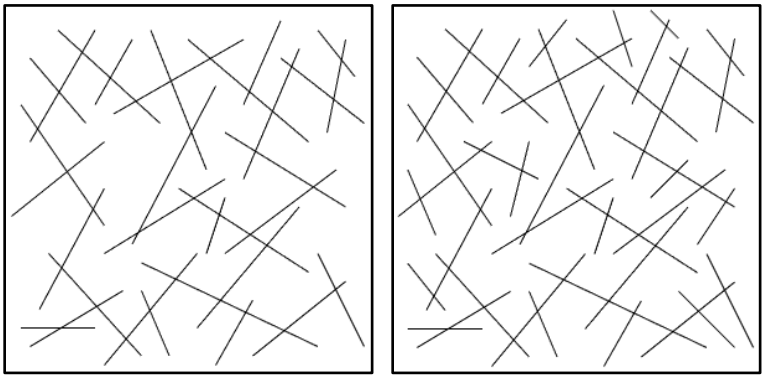

(e) 30 fractures (f) 40 fractures

Fig. 6.5—Five regional sector models with different number of fractures and fracture configuration, and basically fractures are evenly distributed.

The shape factors are then calculated for those cases and results are plotted in **Fig. 6.6**. **Fig. 6.6** indicates that within a sector model the denser the fracture, the larger the shape factor. Since the secondary fracture distribution at the vicinity of hydraulic fracture stages is not even and those outside of SRV are especially poorly developed, a uniform

shape factor distribution of Dual-Porosity or Multi-Porosity Models doesn't physically make sense.

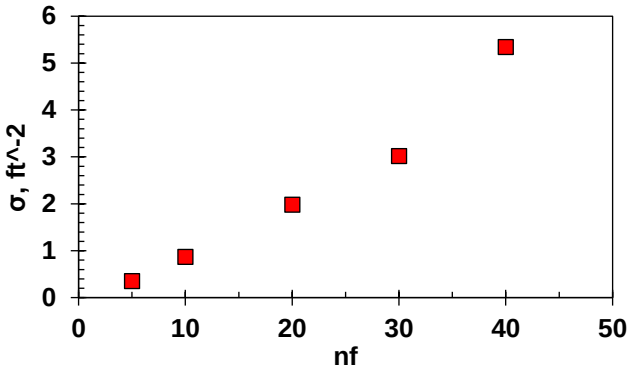

Fig. 6.6—Shape factors for the five different sector models in Fig. 6.5

Those shape factors of different sectors in **Fig. 6.6** are spatially sampled into the vicinity of hydraulic fracture stages such that shape factor decreases as distance from hydraulic fractures increases. As shown in **Fig. 6.7**, shape factors of sector models with 5, 20, and 40 fractures are embedded to different regions near hydraulic fractures. The shape factor in zones closest to hydraulic fractures is highest (red color). Correspondingly the secondary fracture distribution near the center hydraulic fracture is shown at the bottom. It is considered that there are very few secondary fractures in regions far away from hydraulic fractures, and thus assume the shape factor in those regions is $0.01\ ft^{-2}$. Based on shape factor of Kazemi et al. (1976), matrix block size for $\sigma = 0.01\ ft^{-2}$ is $L = 34.64\ ft$. This makes good sense since regions outside of SRV slowly contribute to gas production at the late period.

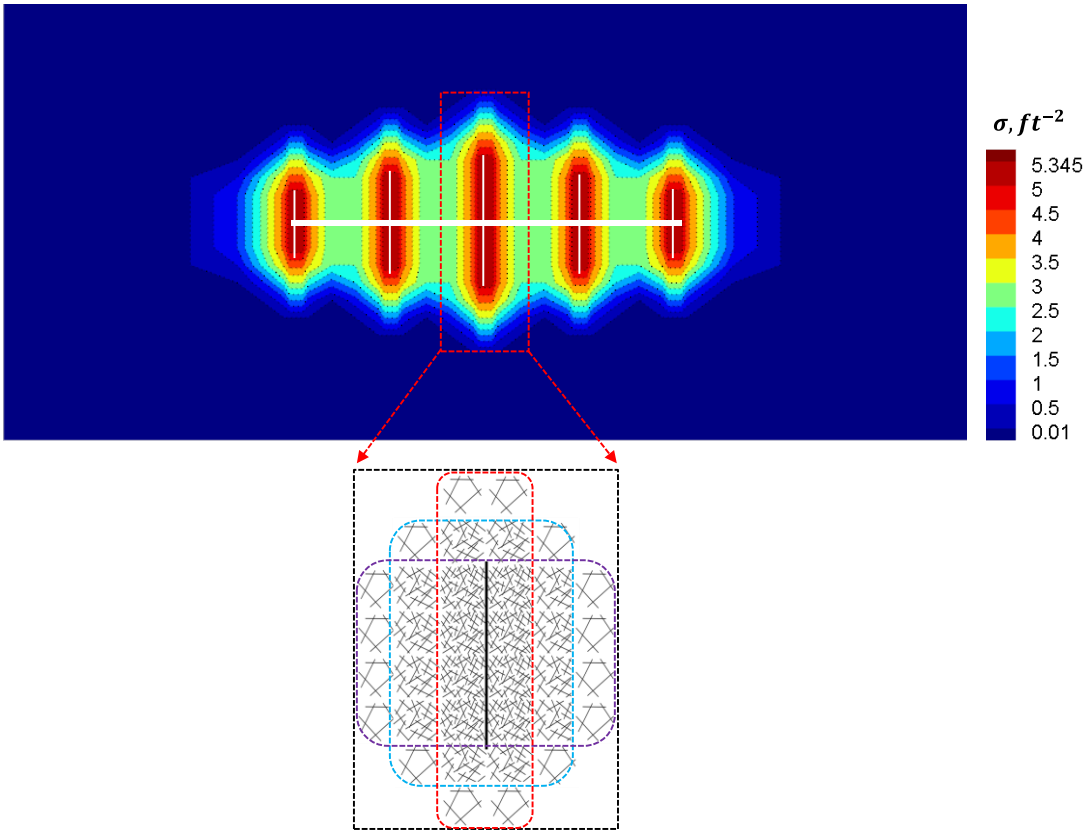

Fig. 6.7—Shape factor distribution based on sector models with different fracture configuration. Upper: shape factor map in field scale; lower: sector model with different fracture distribution.

6.3 Triple-Porosity Triple-Permeability Model

As discussed in Chapter II, there are two types of connections in Multi-Porosity Model (MPM). The first type of connection is intra-porosity connection or neighbor connection (NC), and the second one is inter-porosity connection or non-neighbor connection (NNC). The inter-porosity transport represents the mass transport between different porosity systems, and intra-porosity transport designates the mass transport

within the same porosity system. To be compatible with GURU, those two types of connection are all defined under the connection class in GURU, and their difference lies in how to calculate the transmissibility, as shown in Equation (6.2) and (6.3),

$$T = \frac{T_i T_{i+1}}{T_i + T_{i+1}} \tag{6.2}$$

$$T_i = \begin{cases} \frac{k_i A_i}{L_i}, & (connction \in NC) \\ \sigma V k_i, & (connction \in NNC\ in\ MPM) \end{cases} \tag{6.3}$$

A Triple-Porosity Triple-Permeability Model for shale gas reservoirs is used in this chapter. “Triple-Porosity” specifically considers fracture system (FS), inorganic matrix (IM) and organic matrix (OM) in gas shale. The fracture system includes orthogonal hydraulic fractures by explicit gridding and secondary fractures by multi-porosity representation. Before investigating the importance of connectivity topology, all possible inter-porosity and intra-porosity connections are assumed to be effective. Therefore, Triple-Porosity Triple-Permeability Model allows fluid to transport in each individual porosity system and between different porosity systems. In the fracture domain, logarithmic grid size is used in the direction orthogonal to hydraulic fracture surface such that transient fluid transfer can be well captured (Rubin 2010). Shape factor distribution in **Fig. 6.7** is used to characterize the inter-porosity connections. Based on Equation (6.1), the shape factor is not related to permeability of matrix or secondary fractures, but varies with the secondary fractures distribution and geometries. Therefore, in this model the inorganic and organic matrix permeability is changed to a realistic low value compatible with matrix porosity. In this work two-phase (gas-water) Darcy flow is considered to

investigate the impact of shape factor distribution. Water is mobile in FS since a certain amount of water is resided there after hydraulic fracturing. Water saturation in the IM is at the irreducible level and that in OM is zero. **Table 6.2** provides the associated basic parameters.

Table 6.2—Basic parameters for each porosity system

Reservoir dimension (ft^3)	$800 \times 500 \times 100$
Hydraulic Fracture	
Fracture number	5
Half length (ft)	40, 60, 80, 60, 40
Fracture spacing (ft)	80
Porosity (v/v)	0.001
Fracture conductivity ($mD-ft$)	20
Water saturation (v/v)	0.2 (mobile)
Natural Fracture	
Porosity (v/v)	0.001
Permeability (mD)	5
Water saturation (v/v)	0.2
Inorganic Matrix	
Porosity (v/v)	0.05
Permeability (nD)	100
Matrix water saturation	0.16 (irreducible)
Organic Matrix	
Porosity (v/v)	0.10
Permeability (nD)	10
Matrix water saturation	0.0
Reservoir conditions for all models	
Initial pressure ($psia$)	3000
Minimum BHP ($psia$)	500 for $t > 0$
Maximum gas rate ($MScf/day$)	5000 for $t > 0$
Initial temperature (°F)	200 for $t > 0$
Fluid in the reservoir	Gas and water
Gas composition	5.0 $mol\%$ CO_2 and 95.0 $mol\%$ CH_4

The base case considers the shape factor distribution in **Fig. 6.7**. **Fig. 6.8** illustrates the pressure evolution in three porosity systems at different periods. Specifically the pressure changes follows a sequential order of fracture–inorganics–organics, which is very consistent with the hierarchical permeability distribution in each porosity system. Besides, at early period (**Fig. 6.8(a)**) the transient flow nearby hydraulic fractures is very well captured. In **Fig. 6.8(b)** pressure in the FS decreases to the bottom-hole pressure, while it propagates outside of SRV in IM and OM, causing pseudo radial flow. Finally at the late period pressure in IM and OM decreases to the bottom-hole pressure as well.

In addition, it shows at early period the pressure decreases significantly at the vicinity of hydraulic fractures, which matches well with the shape factor distribution in **Fig. 6.7**. After hydraulic fracturing, secondary fractures nearby perforated stages are generated or reopened from the original sealed status, so the newly generated fractures further subdivide tight shale matrix into smaller block sizes and significantly contribute to fluid flow from tight matrix to the wellbore.

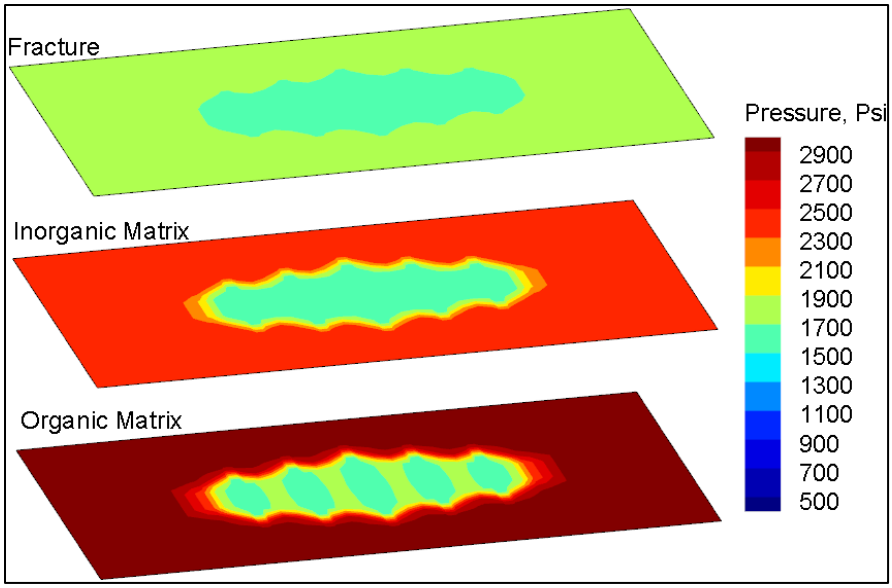

(a) Early period (1 month)

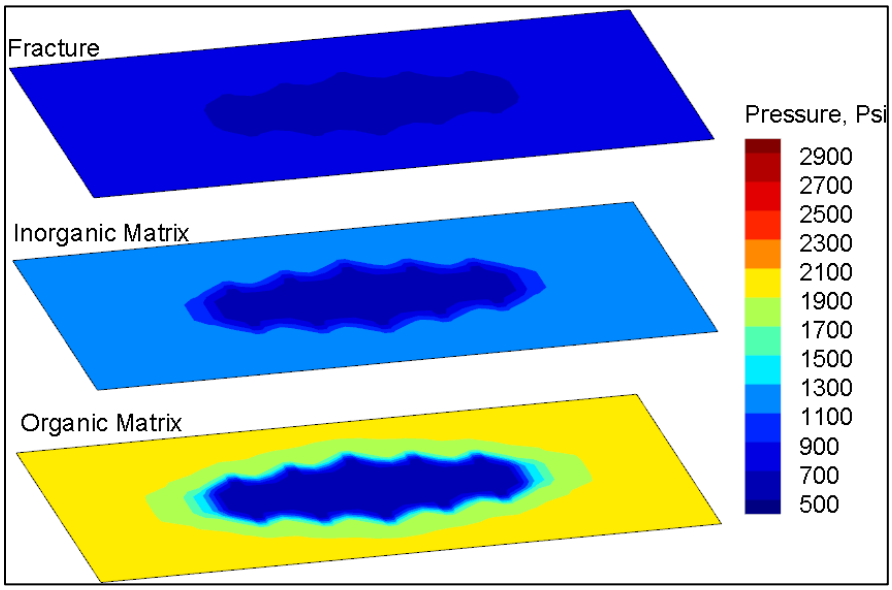

(b) Middle stage (1 year)

Fig. 6.8—Pressure profile in Triple-Porosity Triple-Permeability Model at different stages

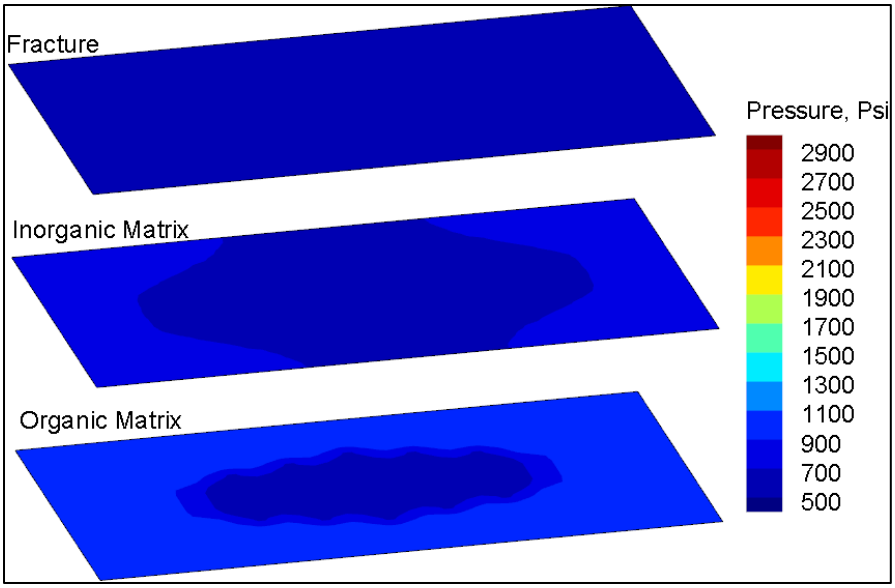

(c) Late period (4.7 years)

Fig. 6.8—Continued.

We further compare with Triple-Porosity Triple-Permeability Models with uniform shape factor distribution in **Fig. 6.9 (a)** to **(c)**. Two different values of shape factor are used, which are the upper limit ($5.345\ ft^{-2}$) and the lower limit ($0.01\ ft^{-2}$) in the upscaled shape factor distribution in **Fig. 6.7**. Other parameters for those two models are exactly the same as the base model.

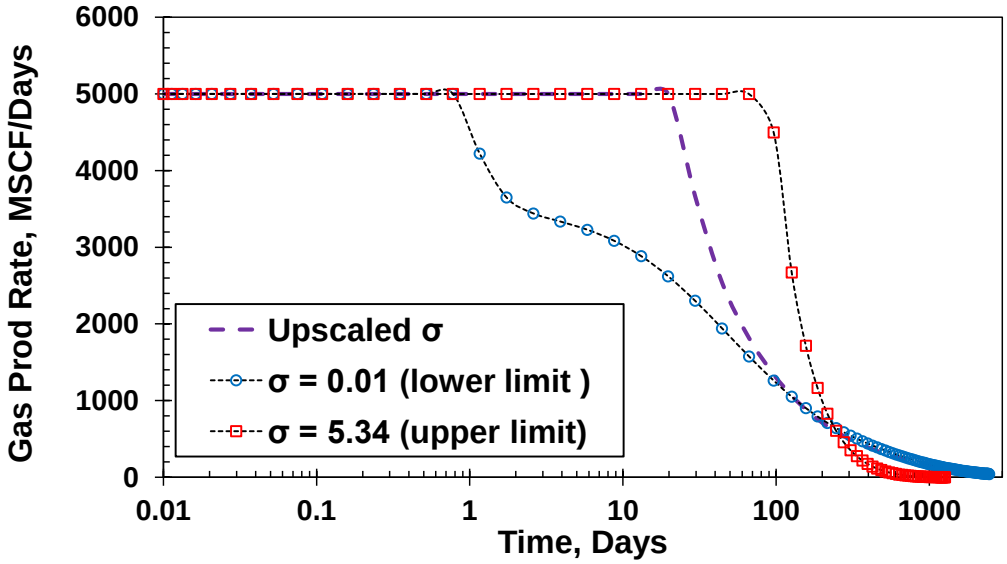

(a)

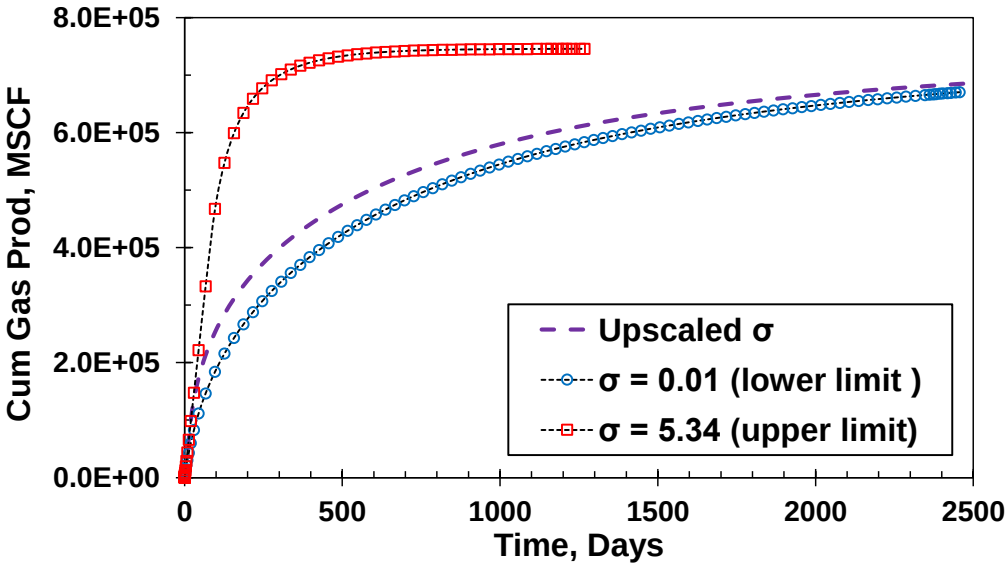

(b)

Fig. 6.9—Comparison of reservoir performance of cases with homogeneous shape factor and case with upscaled shape factor: (a) gas production rate; (b) cumulative gas production; (c) average reservoir pressure.

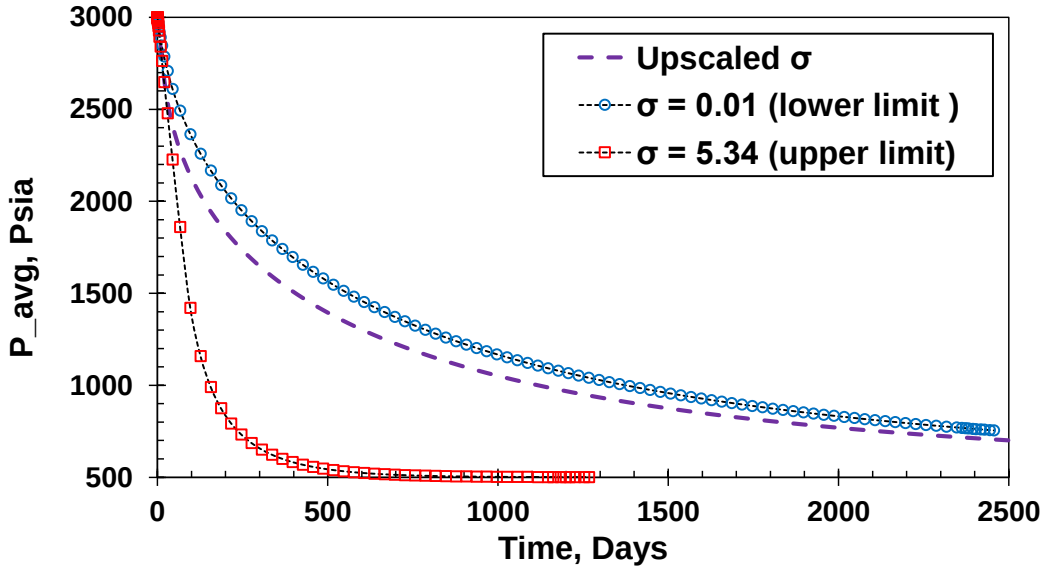

(c)

Fig. 6.9—Continued.

In **Fig. 6.9(a)**, it shows that at the early period all models produces with the maximum allowable gas rate, $5000\ MScf/day$, but different models maintain this rate for different length of time. The model with the lower limit of shape factor ($\sigma = 0.01\ ft^{-2}$) decreases the rate first, while the model with upper limit shape factor ($\sigma = 5.34\ ft^{-2}$) maintains the maximum rate for the longest time. The model with upscaled shape factor falls exactly in between other two models with static shape factor as expected. Besides, the gas rate in the model with upscaled shape factor ultimately converges to the rate of the model with the lower limit shape factor, because in both models the shape factors of matrix in the region outside of SRV are equal to $0.01\ ft^{-2}$. **Fig. 6.9(b)** exhibits that model with upper limit shape factor reaches to maximum cumulative gas rate for the shortest time, and the other two models produces much more slowly because the average

shape factor there is much lower. Correspondingly in **Fig. 6.9(c)** the average reservoir pressure in the model with upper limit of shape factor decreases in the highest speed, followed by the upscaled model, and the model with lower limit of shape factor has the lowest speed to decrease average reservoir pressure. Thus, the comparison tells us that low uniform shape factor assumption tends to underestimate earlier gas production but high uniform shape factor assumption is likely to neglect the slow gas production from matrix outside of SRV.

6.4 Connectivity Topology in Shale Reservoirs

In this section, the connectivity of different porosity systems in shale is evaluated. Different kinds of Triple-Porosity Models have been assumed to be applicable for simulating fluid flow in shale gas reservoirs (Jiang and Younis 2015; Sun et al. 2015). The developed Multi-Porosity preprocessor in Chapter II enables generation of arbitrary connectivity topology with regards to inter-porosity and intra-porosity transport. Six different connectivity topologies in shale reservoirs are presented in **Fig. 6.10 (a)** to **(f)**. It is assumed in all models that hydraulic fractures in fracture porosity are ultimately connected with wellbore at perforated locations. In **Fig. 6.10(a)** all inter-porosity and intra-porosity flux in the Triple-Porosity Model are taken into account as a calibrated model. In **Fig. 6.10(b)**, intra-porosity flux in OM is neglected due to the low permeability, making it is a Triple-Porosity Dual-Permeability Model. In **Fig. 6.10(c)**, intra-porosity flux in IM is further omitted, resulting a Triple-Porosity Single-Permeability Model. For models in **Fig. 6.10 (a)-(c)**, inter-porosity transport in between three different porosity

systems are all considered. Based on Triple-Porosity Model in **Fig. 6.10(c)**, the inter-porosity transport connections are further simplified to for model reduction. Specifically in **Fig. 6.10(d)** inter-porosity flux between IM and OM is ignored such that those two matrix porosity systems are connected to fracture system in a parallel fashion. In **Fig. 6.10(e)**, inter-porosity flux between OM and FS is not considered, so flow occurs in a serial mode of OM–IM–FS–wellbore. Similarly, in **Fig. 6.10(f)** inter-porosity flux between IM and FS is not considered, so flow is in a serial model of IM–OM–FS–wellbore.

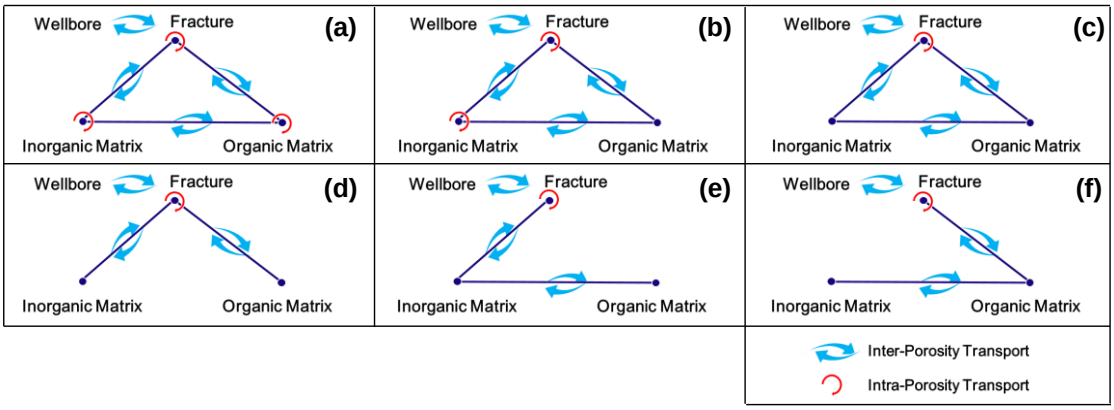

Fig. 6.10—Six different Triple-Porosity Models to simulate shale gas reservoirs: (a) Triple-Porosity Triple-Permeability(TPTP) Model; (b) Triple-Porosity Dual-Permeability(TPDP) Model without intra-porosity flux in OM; (c) Triple-Porosity Single-Permeability(TPSP) Model without intra-porosity flux in OM and IM; (d) TPSP Model with IM and OM tied to FS in parallel; (e) TPSP Model with IM and OM tied to FS in serial as OM-IM-FS-Wellbore; (f) TPSP Model with IM and OM tied to FS in serial as IM-OM-FS-Wellbore.

The connectivity topology in reservoir simulation is numerically represented by transmissibility. Each porosity system is discretized by equal number of grid blocks. Grid

blocks are globally labeled in the sequence of FS, IM and OM grid blocks. Therefore, the transmissibility matrices for the six different Triple-Porosity Models in **Fig. 6.10 (a)** to **(f)** are presented in **Fig. 6.11 (a)** to **(f)**. In this figure the red dots represent the sparse nonzero transmissibilities connecting two grid blocks and here $T_{m,n}$ is a block submatrix of transmissibility between porosity system m and n, $(m, n = F, O, I)$. Therefore, among those matrices, the nonzero blocks in the diagonal are transmissibilities for intra-porosity connection, and those in the off-diagonals are transmissibilites for inter-porosity connection. In **Fig. 6.11 (a)** to **(c)** there are respectively 3, 2 and 1 nonzero block submatrices on the diagonal, because they correspond to the consideration of 3, 2, and 1 intra-porosity connections in Triple-Porosity Models, as shown in **Fig. 6.10 (a)** to **(c)**. Block submatrices of transmissibility in off-diagonal are further nullified in **Fig. 6.11 (d)** to **(f)** since inter-porosity connections are optionally ignored in **Fig. 6.10 (d)** to **(f)**. Therefore, Triple-Porosity models in **Fig. 6.10 (d)** to **(f)** are reduced significantly when compared to Triple-Porosity models in **Fig. 6.10 (a)** to **(c)**. Here the rationale about how much the Triple-Porosity Model can be reduced to simulate a shale gas reservoir is provided, and this is done by comparison of all other models in **Fig. 6.10** with Triple-Porosity Triple-Permeability Model in **Fig. 6.10 (a)**.

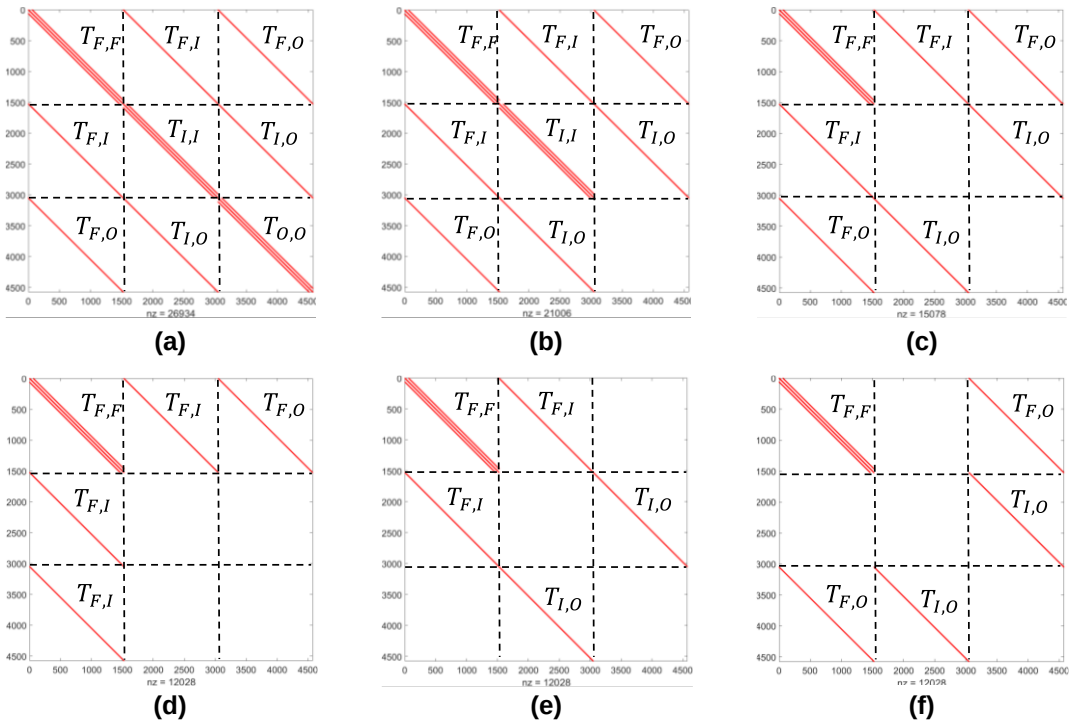

Fig. 6.11—Transmissibility matrices for the Triple-Porosity Models in Fig. 6.10. Red dot represents a non-zero transmissibility connecting two grid blocks, and black dashed rectangular boxes designate subdomains of inter-porosity or intra-porosity connections.

The comparison results are presented in **Fig. 6.12**. Note that the shape factor distribution in **Fig. 6.7** is applied to calculate inter-porosity flux.

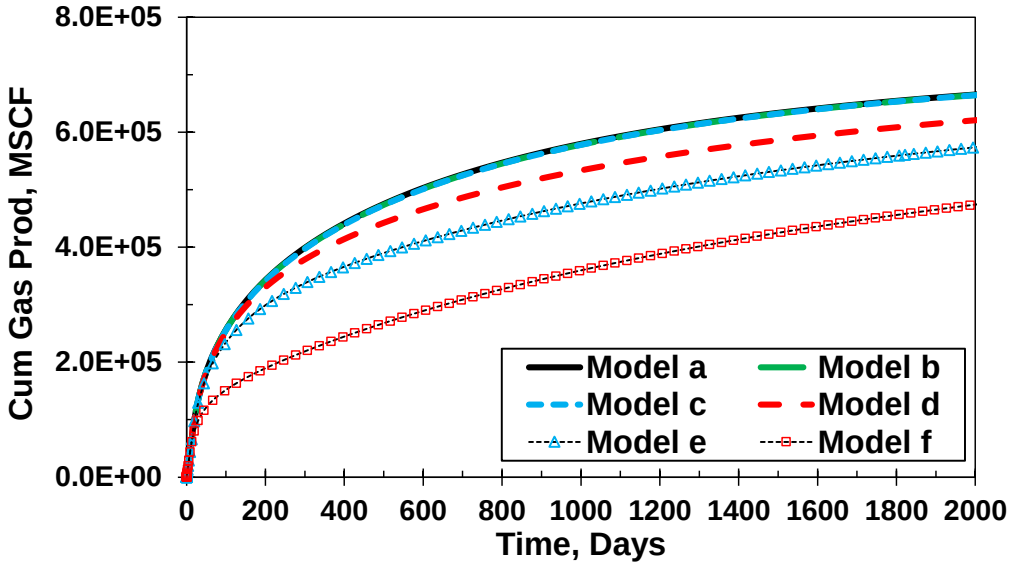

(a)

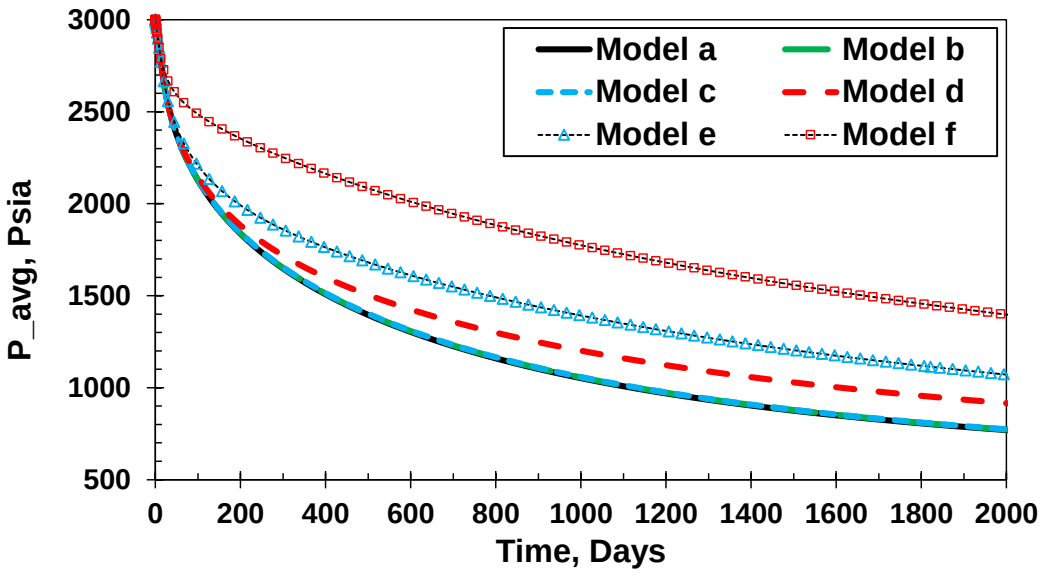

(b)

Fig. 6.12—Cumulative gas producing rate (a) and average reservoir pressure (b) of six different models in Fig. 6.10 (a) to (f).

In **Fig. 6.12**, it shows that model (a), (b), and (c) have equivalent results in cumulative gas production and average reservoir pressure, even though model (a) to (c) have different consideration in matrix intra-porosity connections. This indicates that the matrix intra-porosity connections have negligible impact on fluid flow in gas shale, since the shale matrix permeability is extremely low. Therefore, a Triple-Porosity Single-Permeability Model (**Fig. 6.10 (c)**) is sufficiently accurate modeling shale gas reservoirs.

On the other hand, in **Fig. 6.10** and **Fig. 6.12** model (d) to (f) have different level of consideration in inter-porosity connections through removing edges in the triangular of model (c) in **Fig. 6.10(c)**. With OM to IM connection neglected in model (d), the cumulative gas production after 2000 days decreases about 6.36 % compared to model (c). Alternatively, with OM to FS connection neglected in mode (e), the cumulative gas production after 2000 days decreases about 13.51 % compared to model (c). Finally, with IM to FS connection ignored in model (f), the ultimate cumulative gas production decreases about 28.49 %. Thus, the inter-porosity connection is very important to conduct fluid from matrix flowing into well via fracture system. Specifically the IM to FS connection has the strongest fluid conductivity, the OM to FS connection has the medium conductivity, and the OM to IM connection has the weakest conductivity. This is very important to develop a Triple-Porosity Model with certain reduction such as model (d) to (f), since an assumption without considering one of those inter-porosity connection results in significant impact on hydrocarbon recovery in gas shale.

6.5 Flow Mechanism Analysis

In this section, the effects of non-Darcy flow mechanisms in shale matrix are evaluated. The pore size in shale matrix is in nanoscales. The interaction of molecular with pore walls causes Knudsen diffusion and gas slippage flow. This can be taken into account using apparent permeability for different molecular species. Besides, gas adsorption/desorption is considered through multi-component Langmuir adsorption/desorption model. We considered that gas adsorption is remarkable in OM, while pores in IM are easily blocked by water such that gas adsorption/desorption process is retarded.

Based on Equation (4.63) and the values of matrix porosity and permeability in **Table 6.2**, the average pore radius in different matrix medium is calculated and shown in **Table 6.3**. Further, the apparent permeability is calculated for each component in different media instead of a group pseudo gas component. The ratios of apparent matrix permeability to intrinsic matrix permeability for each component in different media are plotted in **Fig. 6.13**. Those ratio curves in **Fig. 6.13** serve as matrix permeability multiplier to adjust matrix permeability under different thermodynamic conditions. Thus they impact fluxes related to IM and OM.

Table 6.3—Parameters for different matrix type

Matrix Type	k_0, nd	ϕ, fraction	Pore radii, (nm)
Inorganic matrix	100	0.05	20.47
Organic matrix	10	0.1	5.32

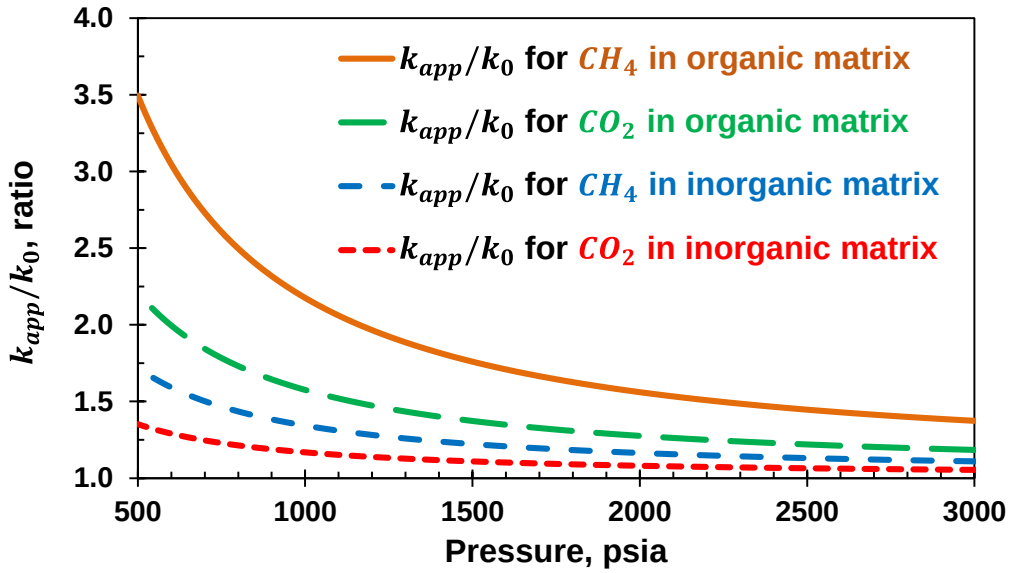

Fig. 6.13—The ratio of apparent permeability (k_{app}) to matrix intrinsic permeability (k_0) for CO_2 and CH_4 at reservoir pressure range

The Langmuir adsorption parameters for CO_2 and CH_4 in organic matrix are based on data from Ambrose et al. (2011) and are presented in **Table 6.4**. The corresponding Langmuir isotherms for those two components are plotted in **Fig. 6.14**. The adsorption storage capacity of CO_2 is around 2.6 times of that for CH_4.

Table 6.4—Adsorption parameters for different gas component

Component	CO_2	CH_4
$p_{L,i}, psia$	832	1562
$V_{L,i}, scf/ton$	145	56

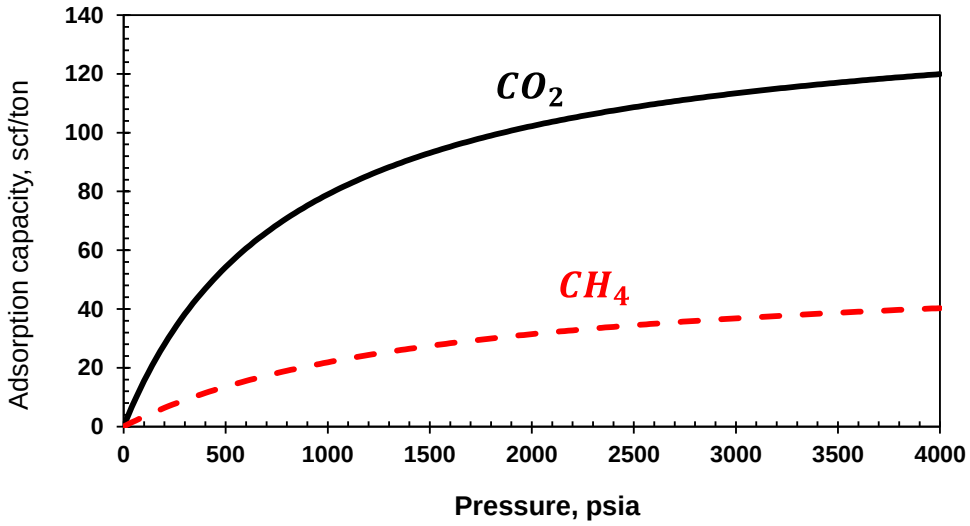

Fig. 6.14—Adsorption isotherms for CO_2 and CH_4

The original gas in place (OGIP) in the unit of $mol\%$ is presented in **Fig. 6.15**. **Fig. 6.15(a)** considers both absorbed gas and free gas. The OGIP in terms of absorbed gas in OM is around $12.19\ mol\%$. The OGIP in terms of free gas stored in FS, IM and OM is respectively $0.55\ mol\%$, $29.08\ mol\%$ and $58.17\ mol\%$. Therefore, the total OGIP stored in OM is $70.36\ mol\%$. In comparison, **Fig. 6.15(b)** considers only free gas stored in gas shale. The OGIP distribution is $0.63\ mol\%$ in FS, $33.12\ mol\%$ in IM and $66.25\ mol\%$ in OM. In both **Fig. 6.15 (a)** and **(b)**, less than $1.0\ mol\%$ of OGIP is stored in FS due to its low pore volume, while around $30\ mol\%$ of OGIP is stored in IM.

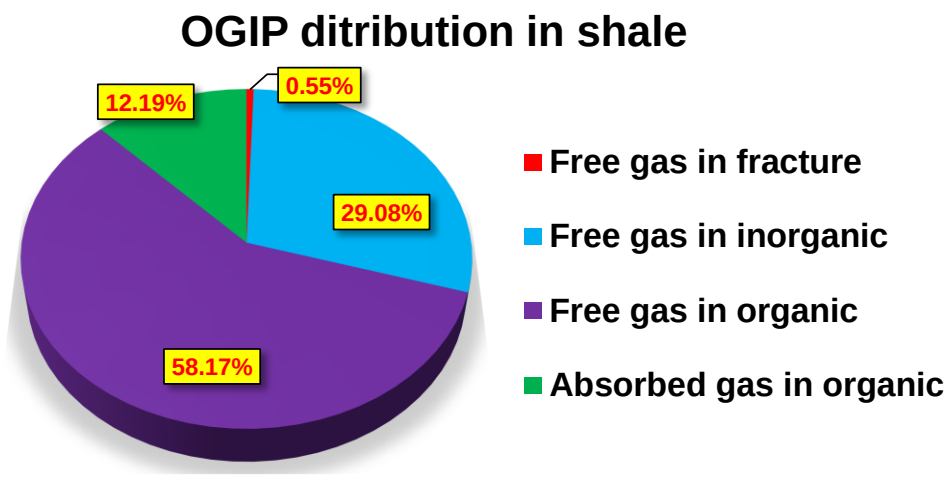

(a)

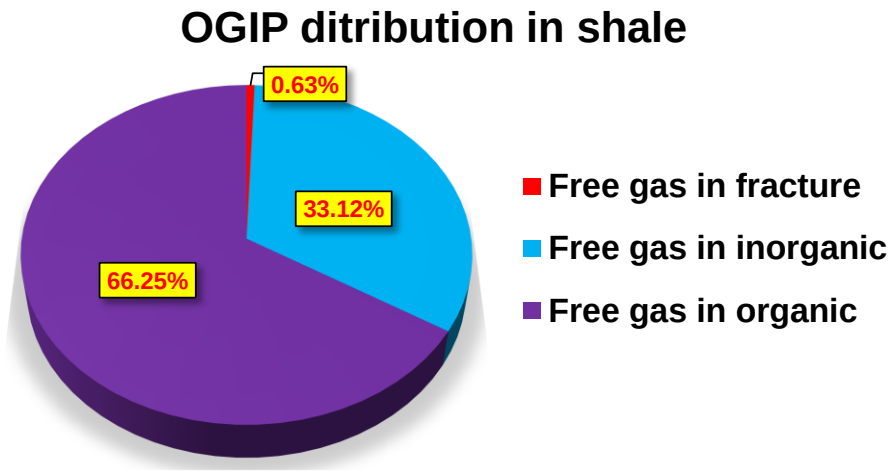

(b)

Fig. 6.15—Fluid in place distribution (unit: *mol*%) in different shale porosity systems: (a) OGIP considering gas adsorption in organic matrix; (b) OGIP with only free gas considered.

Fig. 6.16 provides the comparison for investigating the impact of different mechanisms on gas production in shale. The upscaled shape factor distribution in **Fig. 6.7**

is applied in the transfer function for all inter-porosity connections. The base case, labeled as “Darcy”, considers Darcy flow only in all porosity systems. For comparison the other three cases are setup with different considerations of non-Darcy mechanisms in shale matrix. In the second case, labeled as “Darcy + Desorption”, the Langmuir isotherms in **Fig. 6.14** are taken into account for gas storage mechanism in OM. In the third case, labeled as “Darcy + Perm Multiplier”, the gas apparent permeability considering gas slippage and Knudsen diffusion is considered in both IM and OM. Finally in the fourth case, labeled as “Darcy + Desorption + Perm Multiplier”, gas desorption in OM, gas slippage and Knudsen diffusion in both IM and OM are considered.

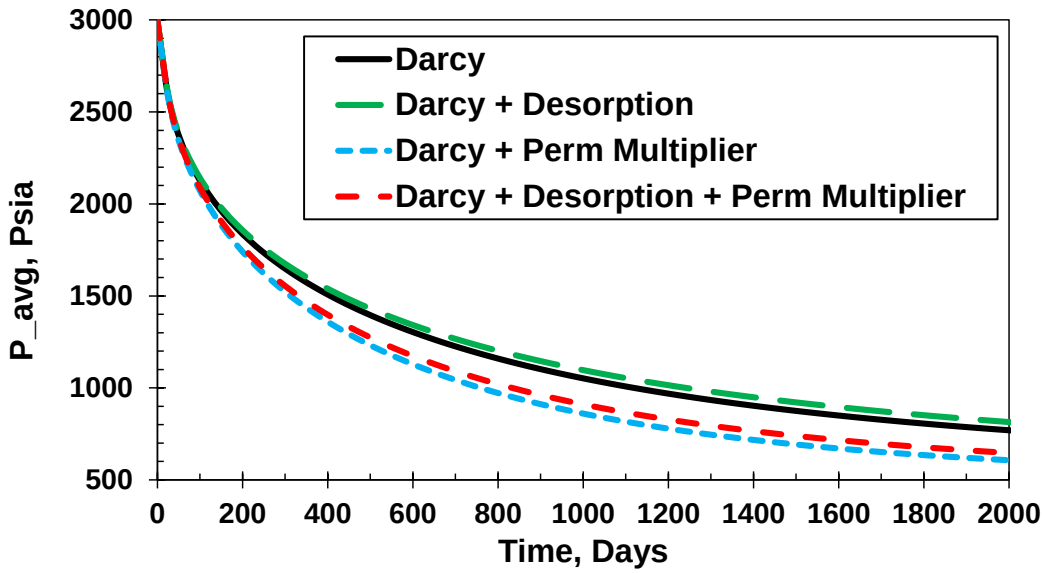

(a)

Fig. 6.16—Reservoir performance comparison for the consideration of different mechanisms: (a) average reservoir pressure; (b) cumulative gas production.

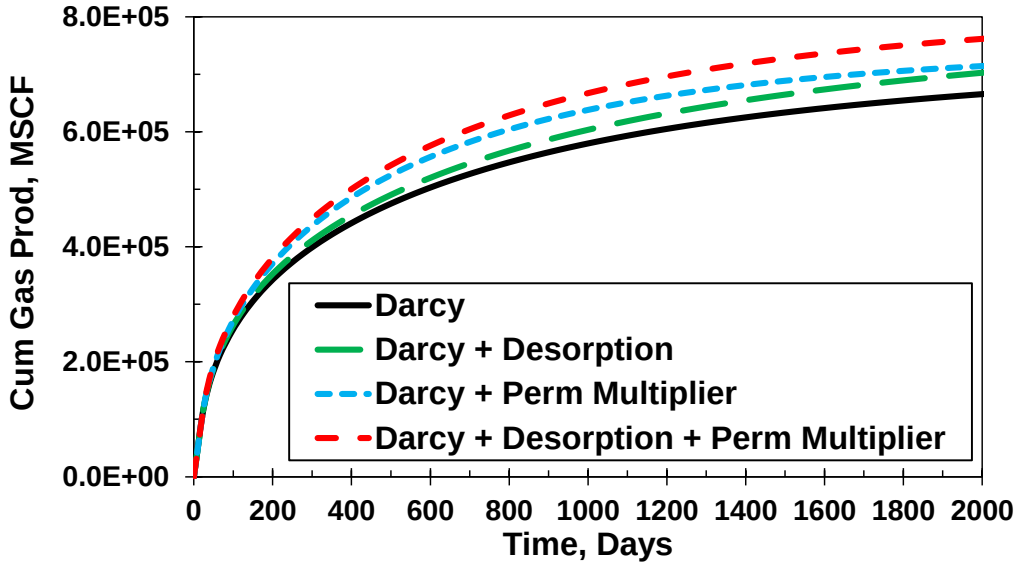

(b)

Fig. 6.16—Continued.

As shown in **Fig. 6.16**, the case "Darcy" produces the least amount of gas in the reservoir after 2000 days. The other three combinations of flow mechanisms present different impacts on gas recovery and average reservoir pressure decrease. The consideration of gas desorption in the OM maintains the average reservoir pressure because of its higher OGIP from gas adsorption. Besides, in this case the ultimate cumulative gas production after 2000 days is increased by 5.59 % compared to case "Darcy". With gas slippage and Knudsen diffusion in shale matrix considered ("Darcy + Perm Multiplier"), the average reservoir pressure decreases with the highest speed, and it produces 7.30 % more gas compared to case "Darcy". The enhancement is caused by the improvement of higher matrix permeability at matrix grid blocks with lower pressure.

Further, in case “Darcy + Desorption + Perm Multiplier”, with matrix permeability enhancement and more OGIP, this model increases 14.43 % of cumulative gas production compared to case “Darcy”. Besides, it has very significant decrease in average reservoir pressure but the pressure decreasing speed is slightly lower than that of “Darcy + Perm Multiplier”, since gas released from desorption in OM helps to maintain the reservoir pressure.

6.6 Summary

In this chapter, GURU is bridged with Multi-Porosity Model and Enhanced Discrete Fracture Network (EDFN) model, and it enables a fully implicit multi-physics compositional simulation with a general Multi-Porosity modeling capability for investigating gas storage and transport mechanisms in gas shales. The influences of discretization and flow physics on shale gas recovery are provided with thorough analysis.

The Enhanced Discrete Fracture Network (EDFN) approach is used to upscale the secondary fracture distribution and provides a shape factor distribution for the Multi-Porosity Model. It is demonstrated that compared to an upscaled shape factor distribution, the low uniform shape factor assumption tends to underestimate earlier gas production but the high uniform shape factor assumption is likely to neglect the slow gas production from matrix outside of SRV.

In a Triple-Porosity Model for gas shale, different configurations of inter-porosity and intra-porosity connection topology are evaluated. It is concluded that intra-porosity connections in the inorganic/organic matrix have negligible contribution to shale gas

recovery, while the inter-porosity connections have different levels of importance. Among the three inter-porosity connection types, the inorganic matrix to fracture connection has the highest contribution to shale gas production, followed by the organic matrix to fracture connection, and the organic matrix to inorganic matrix connection. As a result, a Triple-Porosity Single-Permeability model with all inter-porosity connections considered is sufficient for shale gas reservoir modeling.

Finally, different non-Darcy flow mechanisms are considered in shale matrix. The results show that gas adsorption not only increases the OGIP in shale gas reservoirs, but also improves the ultimate cumulative gas production. The occurrence of gas slippage and Knudsen diffusion in shale matrix porosity system accelerates the pressure drawdown and gas production in the reservoir. The consideration of gas adsorption/desorption, gas slippage and Knudsen diffusion significantly increases ultimate gas recovery in shale.

CHAPTER VII

CONCLUSIONS AND RECOMMENDATIONS

This research work mainly focuses on the development of a general Multi-Porosity Model for fractured reservoirs modeling and an unstructured compositional simulator GURU, and it brings a better reservoir prediction in fractured reservoirs. This chapter illustrates the major conclusions/contributions from the study and also discusses some recommendations for future work.

7.1 Conclusions

1. A general Multi-Porosity Model has been developed. It generalizes conventional Multi-Porosity Models to simulate arbitrary number of porosity types in heterogeneous reservoirs, and also optionally allows porosity subdivision in any porosity system to capture the transient flow effect.
2. Through a binary connection table, the general Multi-Porosity Model is featured to allow arbitrary connection in each individual porosity system or in between any two porosity systems. This design breaks the limitation of fixed connection topology in the conventional Dual-Porosity Models, and allows a convenient transformation between Multi-Porosity Models and Multi-Permeability Models.

3. In addition, a new shape factor considering porosity subdivision is derived and validated. If no porosity subdivision is considered, the formulation is reduced to shape factor from Kazemi et al. (1976).
4. When porosity is not subdivided, Multi-Porosity Models with the shape factor of Lim and Aziz (1995) perform better than Multi-Porosity Models with shape factor of Kazemi et al. (1976), but none of them accurately captures early transient flow induced by the high permeability contrast of the fracture and matrix.
5. When the porosity subdivision and new shape factor is applied to calculate the inter-porosity mass transfer, the accuracy of Multi-Porosity Models increases significantly as the level of the porosity subdivision increases. This can be explained by that the transient inter-porosity transfer is nonlinear and is better approximated with a higher level subdivision.
6. Quad-Porosity Models are successfully applied to simulate gas and water flow in the shale reservoir. With considering capillary pressure, Quad-Porosity Models with and without matrix subdivision provide excellently consistent results.
7. A fully implicit unstructured compositional simulator GURU has been developed. It serves as a basic flow solver to investigate fractured reservoir modeling and shale reservoir modeling in this work.
8. GURU is successfully interfaced with different discrete fracture modeling approaches and the general Multi-Porosity Model, since its framework is

based on Control-Volume Finite-Difference method. Therefore, it works as a convenient platform to evaluate different grid discretization methods.

9. A novel class of compositional space preconditioned VLE methods have been designed to improve the compositional simulation by faster flash convergence. It covers a wide spectrum of reservoir fluids. The performance improvement comes from a decent initial estimate in the flash calculation.
10. GURU is robust for compositional simulation in conventional reservoirs. It is applied to three phase Cartesian model considering permeability heterogeneity, gravity segregation and capillary pressure, and it provides well-matched results with a mature commercial compositional simulator.
11. EDFN (Mi, Lidong et al. 2016) and EDFM (Chai et al. 2016b) are compared by GURU platform, and those two models provide consistent results for multiphase flow through the highly fractured reservoir. However, their difference mainly lies in that EDFN is a Dual-Porosity Single-Permeability Model, but EDFM is a Dual-Porosity Dual-Permeability Model.
12. GURU provides functionality to model production from unconventional reservoirs. It explicitly takes into account the flow physics in those nano-pores in the shale matrix, including multi-component gas adsorption/desorption, gas slippage and Knudsen diffusion in composition space.

13. A unique physics-based shale reservoir modeling workflow is established. Heterogeneity of the fracture system in the SRV is characterized by shape factor distribution upscaled from EDFN sector model, and fracture system, inorganic and organic matrix are included in the Triple-Porosity Model, and non-Darcy flow regimes are taken in account in the GURU engine.
14. Shape factor upscaled from EDFN sector model is more reasonable than uniform distribution of shape factor. A low uniform distribution of shape factor tends to underestimate early gas production in the SRV but a high uniform distribution is likely to overestimate gas production from regions outside of the SRV.
15. In Triple-Porosity Shale Model, intra-porosity connections in the inorganic and organic matrix have negligible impacts on gas recovery. However, the inter-porosity connections are important for gas recovery. The inorganic-to-fracture connection has the highest contribution, followed by the organic-to-fracture connection, and the organic-to-inorganic connection has the minimum impact.
16. Gas adsorption in the organic matrix helps to improve the ultimate cumulative gas production, and the consideration of gas slippage and Knudsen diffusion in both inorganic and organic matrix accelerates the gas production in the reservoir.

7.2 Recommendations

1. Implement modules of wellbore and surface network and further apply GURU in production optimization, surface facility design etc.
2. Implement modules to couple reservoir geo-mechanics with GURU, and thus evaluate the impact of rock compaction on depletion or injection processes in unconventional reservoirs.
3. To further improve the performance of GURU, the numerical Jacobian construction can be replaced by automatic differentiation or analytical Jacobian construction.
4. Implement an Additive Schwartz domain decomposition preconditioner for fractured reservoir modeling in GURU, since during fractured reservoir simulation the convergence speed of the matrix and fracture domains are different.
5. Implement the compositional space preconditioned VLE for sharply varying fluid composition in GURU. So far only the compositional space preconditioned VLE for slightly varied fluid composition has been implemented in GURU.
6. The effect of capillary pressure on VLE in the shale nano-pores can be considered for the simulation of the liquid-rich shale.

REFERENCES

Acs, G., Doleschall, S., and Farkas, E. 1985. General Purpose Compositional Model. SPE Journal. DOI: 10.2118/10515-PA

Aguilera, R. 2010. Flow Units: From Conventional to Tight Gas to Shale Gas Reservoirs. Society of Petroleum Engineers. DOI: 10.2118/132845-MS.

Alfi, M., Yan, B., Cao, Y. et al. 2015. Microscale Porosity Models as Powerful Tools to Analyze Hydrocarbon Production Mechanisms in Liquid Shale. Journal of Natural Gas Science and Engineering 26: 1495-1505. DOI: http://dx.doi.org/10.1016/j.jngse.2015.08.002

Alfi, M., Yan, B., Cao, Y. et al. 2014a. How to Improve Our Understanding of Gas and Oil Production Mechanisms in Liquid-Rich Shale. Society of Petroleum Engineers. DOI: 10.2118/170959-MS.

Ambrose, R.J., Hartman, R.C., and Akkutlu, I.Y. 2011. Multi-Component Sorbed Phase Considerations for Shale Gas-in-Place Calculations. Society of Petroleum Engineers. DOI: 10.2118/141416-MS.

Ambrose, R.J., Hartman, R.C., Diaz-Campos, M. et al. 2012. Shale Gas-in-Place Calculations Part I: New Pore-Scale Considerations. SPE Journal DOI: 10.2118/131772-PA

Barenblatt, G.E. and Zheltov, I.P. 1960. Basic Concepts in the Theory of Seepage of Homogeneous Liquids in Fissured Rocks. J. Appl. Math 24 (5): 1286-1303.

Basquet, R., Bourbiaux, B.J., and Cohen, C.E. 2005. Fracture Flow Property Identification: An Optimized Implementation of Discrete Fracture Network Models. Society of Petroleum Engineers. DOI: 10.2118/93748-MS.

Bowen, G. and Crumpton, P. 2003. A New Formulation for the Implicit Compositional Simulation of Miscible Gas Injection Processes. Society of Petroleum Engineers. DOI: 10.2118/79692-MS.

Cao, H. 2002. Development of Techniques for General Purpose Simulators. PhD Dissertation, Stanford University.

Cao, Y., Yan, B., Alfi, M. et al. 2015. A Novel Compositional Model of Simulating Fluid Flow in Shale Resrvoirs - Some Priliminary Tests and Results. Society of Petroleum Engineers. DOI: 10.2118/175589-MS.

Chai, Z., Yan, B., Killough, J. et al. 2016a. Dynamic Embedded Discrete Fracture Multi-Continuum Model for the Simulation of Fractured Shale Reservoirs. Paper

presented at the SPE Interational Petroleum Technology Conference, Bangkok, Thailand.

Chai, Z., Yan, B., Killough, J. et al. 2016b. An Efficient Method for Fractured Shale Reservoir History Matching: The Embedded Discrete Fracture Multi-Continuum Approach. Paper presented at the SPE Annual Technical Conference & Exhibition, Dubai, UAE.

Chapman, S.J. 2007. Fortran 95/2003 for Scientists & Engineers: McGraw-Hill Primis. Original edition. ISBN 0-390-91197-6.

Chien, M.C.H., Lee, S.T., and Chen, W.H. 1985. A New Fully Implicit Compositional Simulator. Society of Petroleum Engineers. DOI: 10.2118/13385-MS.

Civan, F. 2010. Effective Correlation of Apparent Gas Permeability in Tight Porous Media. Transport in Porous Media 82 (2): 375-384. DOI: 10.1007/s11242-009-9432-z

Coats, K.H. 1980. An Equation of State Compositional Model. SPE Journal. DOI: 10.2118/8284-PA

Coats, K.H. 1989. Implicit Compositional Simulation of Single-Porosity and Dual-Porosity Reservoirs. Paper presented at the SPE Symposium on Reservoir Simulation, Houston, Texas. Society of Petroleum Engineers 00018427. DOI: 10.2118/18427-ms.

Collins, D.A., Nghiem, L.X., Li, Y.K. et al. 1992. An Efficient Approach to Adaptive-Implicit Compositional Simulation with an Equation of State. SPE Reservoir Engineering. DOI: 10.2118/15133-PA

Cui, J., Yang, C., Zhu, D. et al. 2016. Fracture Diagnosis in Multiple-Stage-Stimulated Horizontal Well by Temperature Measurements with Fast Marching Method. SPE Journal. DOI: 10.2118/174880-PA

Cui, J., Zhu, D., and Jin, M. 2016. Diagnosis of Production Performance after Multistage Fracture Stimulation in Horizontal Wells by Downhole Temperature Measurements. SPE Production & Operation. DOI: 10.2118/170874-PA

Dake, L.P. 1978. Fundamentals of Reservoir Engineering. Ed Ed, T. Amsterdam, The Netherlands: Elsevier. Original edition. ISBN 9780444418302.

Dennis, J.E.J. and Schnabel, R.B. 1983. Numerical Methods for Unconstrained Optimization and Nonlinear Equations,. N.J.: Prentice Hall. Original edition. ISBN 978-0-89871-364-0.

Fathi, E. and Akkutlu, I.Y. 2012. Lattice Boltzmann Method for Simulation of Shale Gas Transport in Kerogen. SPE Journal. DOI: 10.2118/146821-PA

Firoozabadi, A. 1999. Thermodynamic of Hydrocarbon Reservoirs. New York: McGraw-Hill. Original edition.

Fisher, M.K., Heinze, J.R., Harris, C.D. et al. 2004. Optimizing Horizontal Completion Techniques in the Barnett Shale Using Microseismic Fracture Mapping. Society of Petroleum Engineers. DOI: 10.2118/90051-MS.

Fung, L.S.K. 1991. Simulation of Block-to-Block Processes in Naturally Fractured Reservoirs. SPE Reservoir Engineering 6 (4): 477-484. DOI: 10.2118/20019-pa

Fung, L.S.K., Su, H., Tan, C.T. et al. 2005. A Fully-Implicit Fully-Coupled Well Model for Parallel Mega-Cell Reservoir Simulation. Society of Petroleum Engineers. DOI: 10.2118/106331-MS.

Fussell, D.D. and Yanosik, J.L. 1979. An Iterative Sequence for Phase-Equilibria Calculations Incorporating the Redlich-Kwong Equation of State. SPE Journal. DOI: 10.2118/6050-PA

Gilman, J.R. 1986. An Efficient Finite-Difference Method for Simulating Phase Segregation in the Matrix Blocks in Double-Porosity Reservoirs. SPE Reservoir Engineering 1 (4): 403-413. DOI: 10.2118/12271-pa

Gilman, J.R. 2003. Practical Aspects of Simulation of Fractured Reservoirs. In International Forum on Reservoir Simulation. Buhl, Germany.

Gilman, J.R. and Kazemi, H. 1988. Improved Calculations for Viscous and Gravity Displacement in Matrix Blocks in Dual-Porosity Simulators (Includes Associated Papers 17851, 17921, 18017, 18018, 18939, 19038, 19361 and 20174). Journal of Petroleum Technology 40 (1): 60-70. DOI: 10.2118/16010-pa

He, J., Killough, J.E., Fadlelmula F, M.M. et al. 2015. A Unified Finite Difference Model for the Simulation of Transient Flow in Naturally Fractured Carbonate Karst Reservoirs. Society of Petroleum Engineers. DOI: 10.2118/173262-MS.

Hinkley, R., Gu, Z., Wong, T. et al. 2013. Multi-Porosity Simulation of Unconventional Reservoirs. Paper presented at the SPE Unconventional Resources Conference - Canada, Calgary, Alberta, Canada. 2013, Society of Petroleum Engineers SPE-167146-MS. DOI: 10.2118/167146-ms.

Hinkley, R., Wang, Q., Wang, K. et al. 2013. Flexible and Efficient N-Porosity, Full-Featured Simulator Design, and Application. Paper presented at the 2013 SPE

Reservoir Simulation Symposium, The Woodlands, TX, USA. Society of Petroleum Engineers SPE-163619-MS. DOI: 10.2118/163619-ms.

Javadpour, F. 2009. Nanopores and Apparent Permeability of Gas Flow in Mudrocks (Shales and Siltstone). Journal of Canadian Petroleum Technology 48 (08): 16-21.

Jiang, J. and Younis, R.M. 2015. A Generic Physics-Based Numerical Platform with Hybrid Fracture Modelling Techniques for Simulating Unconventional Gas Reservoirs. Society of Petroleum Engineers. DOI: 10.2118/173318-MS.

Jiang, J. and Younis, R.M. 2016. Compositional Modeling of Enhanced Hydrocarbons Recovery for Fractured Shale Gas-Condensate Reservoirs with the Effects of Capillary Pressure and Multicomponent Mechanisms. Society of Petroleum Engineers. DOI: 10.2118/179704-MS.

Ju, L. and Burkardt, J. MGMRES. https://People.Sc.Fsu.Edu/~Jburkardt/Cpp_Src/Mgmres/Mgmres.Html.

Karimi-Fard, M., Durlofsky, L.J., and Aziz, K. 2004. An Efficient Discrete-Fracture Model Applicable for General-Purpose Reservoir Simulators. SPE Journal 9(02). DOI: 10.2118/88812-PA

Kazemi, H., Gilman, J.R., and Elsharkawy, A.M. 1992. Analytical and Numerical Solution of Oil Recovery from Fractured Reservoirs with Empirical Transfer Functions (Includes Associated Papers 25528 and 25818). DOI: 10.2118/19849-PA

Kazemi, H., Merrill Jr., L.S., Porterfield, K.L. et al. 1976. Numerical Simulation of Water-Oil Flow in Naturally Fractured Reservoirs. Society of Petroleum Engineers Journal 16 (6): 317-326. DOI: 10.2118/5719-pa

Lee, S.H., Lough, M.F., and Jensen, C.L. 2001. Hierarchical Modeling of Flow in Naturally Fractured Formations with Multiple Length Scales. Water Resources Research 37 (3): 443-455. DOI: 10.1029/2000WR900340

Li, J., Lei, Z., Qin, G. et al. 2015. Effective Local-Global Upscaling of Fractured Reservoirs under Discrete Fractured Discretization. Energies 8 (9): 10178.

Li, Z. and Firoozabadi, A. 2012. General Strategy for Stability Testing and Phase-Split Calculation in Two and Three Phases. DOI: 10.2118/129844-PA

Lim, K.-T., Schiozer, D.J., and Aziz, K. 1995. A New Approach for Residual and Jacobian Arrays Construction in Reservoir Simulators. SPE Computer Applications. DOI: 10.2118/28248-PA

Lim, K.T. and Aziz, K. 1995. Matrix-Fracture Transfer Shape Factors for Dual-Porosity Simulators. Journal of Petroleum Science and Engineering 13 (3–4): 169-178. DOI: http://dx.doi.org/10.1016/0920-4105(95)00010-F

Lohrenz, J., Bray, B.G., and Clark, C.R. 1964. Calculating Viscosities of Reservoir Fluids from Their Compositions. Journal of Petroleum Technology 16 (10): 1,171 - 171,176. DOI: 10.2118/915-PA

Mathworks. 2015. Matlab R2015b. MathWorks Inc.

Mayerhofer, M.J., Lolon, E., Warpinski, N.R. et al. 2010. What Is Stimulated Reservoir Volume? SPE Production & Operations. DOI: 10.2118/119890-PA

McLennan, J. and Potocki, D. 2013. Hydraulic Fracturing Complexity: Interaction between Hydraulic and Natural Fractures. In AAPG Workshop : Geomechanics and Reservoir Characterization of Shales and Carbonates. Baltimore. Baltimore, USA.

Mi, L., Jiang, H., Li, J. et al. 2014. The Investigation of Fracture Aperture Effect on Shale Gas Transport Using Discrete Fracture Model. Journal of Natural Gas Science and Engineering 21: 631-635. DOI: http://dx.doi.org/10.1016/j.jngse.2014.09.029

Mi, L., Jiang, H., Mou, S. et al. 2016. Numerical Simulation Study of Shale Gas Reservoir with Stress-Dependent Fracture Conductivity Using Multiscale Discrete Fracture Network Model. Particulate Science and Technology: null-null. DOI: 10.1080/02726351.2016.1241844

Mi, L., Jiang, H., Tang, L. et al. 2016. A Utility Discrete Fracture Network Model for Field-Scale Simulation of Naturally Fractured Shale Reservoirs. Society of Petroleum Engineers. DOI: 10.2118/180968-MS.

Moinfar, A., Varavei, A., Sepehrnoori, K. et al. 2014. Development of an Efficient Embedded Discrete Fracture Model for 3d Compositional Reservoir Simulation in Fractured Reservoirs. SPE Journal 19(02). DOI: 10.2118/154246-PA

Odusina, E.O., Sondergeld, C.H., and Rai, C.S. 2011. An Nmr Study of Shale Wettability. Paper presented at the Canadian Unconventional Resources Conference, Alberta, Canada. Society of Petroleum Engineers SPE-147371-MS. DOI: 10.2118/147371-ms.

Passey, Q.R., Bohacs, K., Esch, W.L. et al. 2010. From Oil-Prone Source Rock to Gas-Producing Shale Reservoir Geologic and Petrophysical Characterization of Unconventional Shale-Gas Reservoirs. Paper presented at the International Oil and Gas Conference and Exhibition in China, Beijing, China. Society of Petroleum Engineers SPE-131350-MS. DOI: 10.2118/131350-ms.

Peaceman, D.W. 1990. Interpretation of Wellblock Pressures in Numerical Reservoir Simulation: Part 3 -- Off-Center and Multiple Wells within a Wellblock. DOI: 10.2118/16976-PA

Péneloux, A., Rauzy, E., and Fréze, R. 1982. A Consistent Correction for Redlich-Kwong-Soave Volumes. Fluid Phase Equilibria 8 (1): 7-23. DOI: http://dx.doi.org/10.1016/0378-3812(82)80002-2

Peng, D.-Y. and Robinson, D.B. 1976. A New Two-Constant Equation of State. Industrial & Engineering Chemistry Fundamentals 15 (1): 59-64. DOI: 10.1021/i160057a011

Pruess, K. 1982. GMINC – a Mesh Generator for Flow Simulations in Fractured Reservoirs.

Pruess, K. 1985. A Practical Method for Modeling Fluid and Heat Flow in Fractured Porous Media. Society of Petroleum Engineers Journal 25 (1): 14-26. DOI: 10.2118/10509-pa

Rachford, H.H. and Rice, J.D. 1952. Procedure for Use of Electrical Digital Computers in Calculating Flash Vaporization Hydrocarbon Equilibrium. Journal of Petroleum Technology 4 (10): 19 - 13. DOI: http://dx.doi.org/10.2118/952327-G

Rubin, B. 2010. Accurate Simulation of Non Darcy Flow in Stimulated Fractured Shale Reservoirs. Society of Petroleum Engineers. DOI: 10.2118/132093-MS.

Sarda, S., Jeannin, L., and Bourbiaux, B. 2001. Hydraulic Characterization of Fractured Reservoirs: Simulation on Discrete Fracture Models. Society of Petroleum Engineers. DOI: 10.2118/66398-MS.

Sarma, P. and Aziz, K. 2006. New Transfer Functions for Simulation of Naturally Fractured Reservoirs with Dual-Porosity Models. SPE Journal 11 (3): pp. 328-340. DOI: 10.2118/90231-pa

Schlumberger. 2012. Eclipse Technical Description: Schlumberger.

Stone, H.L. 1973. Estimation of Three-Phase Relative Permeability and Residual Oil Data. Journal of Canadian Petroleum Technology. DOI: 10.2118/73-04-06

Suliman, B., Meek, R., Hull, R. et al. 2013. Variable Stimulated Reservoir Volume (Srv) Simulation: Eagle Ford Shale Case Study. Society of Petroleum Engineers. DOI: 10.1190/URTEC2013-057.

Sun, D., Xu, Y., Chen, H. et al. 2012. A Mean Flow Acoustic Engine Capable of Wind Energy Harvesting. Energy Conversion and Management 63: 101-105. DOI: http://dx.doi.org/10.1016/j.enconman.2011.12.035

Sun, H., Chawathe, A., Hoteit, H. et al. 2015. Understanding Shale Gas Flow Behavior Using Numerical Simulation. SPEJ. DOI: 10.2118/167753-PA

Sun, J., Hu, K., Wong, J. et al. 2014a. Investigating the Effect of Improved Fracture Conductivity on Production Performance of Hydraulic Fractured Wells through Field Case Studies and Numerical Simulations. Society of Petroleum Engineers. DOI: 10.2118/169866-MS.

Sun, J. and Schechter, D.S. 2014b. Optimization-Based Unstructured Meshing Algorithms for Simulation of Hydraulically and Naturally Fractured Reservoirs with Variable Distribution of Fracture Aperture, Spacing, Length and Strike. Society of Petroleum Engineers. DOI: 10.2118/170703-MS.

Thomas, L.K., Dixon, T.N., and Pierson, R.G. 1983. Fractured Reservoir Simulation. Society of Petroleum Engineers Journal 23 (1): 42-54. DOI: 10.2118/9305-pa

Tuminaro, R.S., Heroux, M., Hutchinson, S.A. et al. 1999. Official Aztec User's Guide: Version 2.1. Albuquerque, New Mexico: Sandia National Laboratories.

Ueda, Y., Murata, S., Watanabe, Y. et al. 1989. Investigation of the Shape Factor Used in the Dual-Porosity Reservoir Simulator. Paper presented at the SPE Asia-Pacific Conference, Sydney, Australia. DOI: 10.2118/19469-ms.

Valbuena, E. 2015. Production Performance Modeling through Integration of Reservoir and Production Network with Asphaltene Deposition. PhD Dissertation, Texas A&M University, College Station.

Vera, F. and Shadravan, A. 2015. Stimulated Reservoir Volume 101: Srv in a Nutshell. International Petroleum Technology Conference. DOI: 10.2523/IPTC-18413-MS.

Wang, F.P. and Reed, R.M. 2009. Pore Networks and Fluid Flow in Gas Shales. Paper presented at the SPE Annual Technical Conference and Exhibition, New Orleans, Louisiana. Society of Petroleum Engineers. DOI: 10.2118/124253-MS.

Wang, Y., Yan, B., and Killough, J.E. 2013f. Compositional Modeling of Tight Oil Using Dynamic Nanopore Properties. Paper presented at the 2013 SPE Annual Technical Conference and Exhibition, New Orleans, Louisiana. Society of Petroleum Engineers SPE 166267.

Warren, J.E. and Root, P.J. 1962. The Behavior of Naturally Fractured Reservoirs. SPE Journal. DOI: 10.2118/426-pa

Whitson, C.H. and Brule, M.R. 2000. Phase Behavior. Ed SPE. Henry L. Doherty Memorial Fund of Aime. Richardson Texas Original edition.

Wilson, G.M. 1968. A Modified Redlich-Kwong Equation of State, Application to General Physical Data Calculations. In 65th National AIChE Meeting. Cleveland, Ohio.

Wong, T.W., Firoozabadi, A., and Aziz, K. 1990. Relationship of the Volume-Balance Method of Compositional Simulation to the Newton-Raphson Method. SPE Reservoir Engineering 5 (03): 415 - 422. DOI: 10.2118/18424-PA

Wu, K., Chen, Z., and Li, X. 2015. Real Gas Transport through Nanopores of Varying Cross-Section Type and Shape in Shale Gas Reservoirs. Chemical Engineering Journal 281: 813-825. DOI: http://dx.doi.org/10.1016/j.cej.2015.07.012

Wu, K., Chen, Z., Li, X. et al. 2016. A Model for Multiple Transport Mechanisms through Nanopores of Shale Gas Reservoirs with Real Gas Effect–Adsorption-Mechanic Coupling. International Journal of Heat and Mass Transfer 93: 408-426. DOI: http://dx.doi.org/10.1016/j.ijheatmasstransfer.2015.10.003

Wu, K., Li, X., Wang, C. et al. 2015. Model for Surface Diffusion of Adsorbed Gas in Nanopores of Shale Gas Reservoirs. Industrial & Engineering Chemistry Research 54 (12): 3225-3236. DOI: 10.1021/ie504030v

Wu, Y.-S., Li, J., Ding, D. et al. 2014. A Generalized Framework Model for the Simulation of Gas Production in Unconventional Gas Reservoirs. DOI: 10.2118/163609-PA

Yan, B., Alfi, M., Wang, Y. et al. 2013b. A New Approach for the Simulation of Fluid Flow in Unconventional Reservoirs through Multiple Permeability Modeling. Society of Petroleum Engineers. DOI: 10.2118/166173-MS.

Yan, B., Killough, J.E., Wang, Y. et al. 2013a. Novel Approaches for the Simulation of Unconventional Reservoirs. Society of Petroleum Engineers. DOI: 10.1190/URTEC2013-131.

Yan, B., Wang, Y., and Killough, J.E. 2015. Beyond Dual-Porosity Modeling for the Simulation of Complex Flow Mechanisms in Shale Reservoirs. Computational Geosciences: 1-23. DOI: 10.1007/s10596-015-9548-x

Young, L.C. and Stephenson, R.E. 1983. A Generalized Compositional Approach for Reservoir Simulation. SPE Journal. DOI: 10.2118/10516-PA

Yu, Y., Sun, D., Wu, K. et al. 2011. Cfd Study on Mean Flow Engine for Wind Power Exploitation. Energy Conversion and Management 52 (6): 2355-2359. DOI: http://dx.doi.org/10.1016/j.enconman.2010.12.046

Yu, Y.S.W., Graff, M.M., and Hartmann, M.J.Z. 2016. Mechanical Responses of Rat Vibrissae to Airflow. The Journal of Experimental Biology 219 (7): 937-948. DOI: 10.1242/jeb.126896

Zimmerman, R.W., Chen, G., Hadgu, T. et al. 1993. A Numerical Dual-Porosity Model with Semianalytical Treatment of Fracture/Matrix Flow. Water Resources Research 29 (7): 2127-2137. DOI: 10.1029/93wr00749

APPENDIX A

EQUATION OF STATE

This appendix illustrates the basic formulation for Peng-Robinson Equation of State (PR-EOS), shown as Equation (A.1),

$$Z^3 - (1 - B)Z^2 + (A - 3B^2 - 2B)Z - (AB - B^2 - B^3) = 0 \quad \text{(A.1)}$$

Here the parameters are defined as,

$$A = \frac{ap}{(RT)^2} \quad \text{(A.2)}$$

$$B = \frac{bp}{RT} \quad \text{(A.3)}$$

$$a = \sum_{j=1}^{n_h} \sum_{i=1}^{n_h} x_i x_j \left(1 - \kappa_{ij}\right) \sqrt{a_i a_j} \quad \text{(A.4)}$$

$$b = \sum_{i=1}^{n_h} x_i b_i \quad \text{(A.5)}$$

$$a_i = 0.45724 \alpha(T) \frac{(RT_{ci})^2}{p_{ci}} \quad \text{(A.6)}$$

$$b_i = 0.07780 \frac{RT_{ci}}{p_{ci}} \quad \text{(A.7)}$$

$$\alpha(T) = [1 + m_i(1 - \sqrt{T/T_{ci}})]^2 \quad \text{(A.8)}$$

$$m_i = \begin{cases} 0.37464 + 1.54226\omega_i - 0.2699\omega_i^2 & (\omega_i < 0.49) \\ 0.379642 + 1.48503\omega_i - 0.164423\omega_i^2 + 0.01167\omega_i^3 & (Otherwise) \end{cases} \quad \text{(A.9)}$$

Z factors are solved through the equation of state, and then fugacity coefficient can be calculated, as shown in Equation (A.10),

$$ln\varphi_i = -\ln(Z-B) + (Z-1)\frac{b_i}{b} - \frac{A}{2\sqrt{2}B}\left[\frac{1}{a}\left(2\sqrt{a_i}\sum_{j=1}^{n_h} x_j\sqrt{a_j}(1-\kappa_{ij})\right) - \frac{b_i}{b}\right] ln\left(\frac{Z+(1+\sqrt{2})B}{Z+(1-\sqrt{2})B}\right) \quad \text{(A.10)}$$

The derivatives of fugacity coefficients with regards to phase compositions and pressure can be referred to Appendix A in Cao (2002), so here they are discussed for simplicity. Those derivatives are very important to assemble the Jacobian matrix in Vapor-Liquid Equilibrium.

APPENDIX B

VAPOR LIQUID EQUILIBRIUM

This appendix discusses the basic approaches used in Vapor-Liquid Equilibrium (VLE) calculation. VLE can be written in terms of function, as shown in Equation (B.1).

$$[x_i, y_i, f_v] = \boldsymbol{VLE}(p, T, z_i) \tag{B.1}$$

Basically two approaches are used to solve Equation (B.1), including Successive Substitution Iteration (SSI) method and Newton-Raphson (NR) method. Both of them deal with the following two residuals: Equation (B.2) is the phase fugacity equilibrium and Equation (B.3) is phase component material balance.

$$R_{f,i} = lnK_i + ln\varphi_i^v - ln\varphi_i^l = 0, \qquad i = 1, \cdots, n_h \tag{B.2}$$

$$R_r = \sum_{i=1}^{n_h}(y_i - x_i) = \sum_{i=1}^{n_h} \frac{z_i(K_i-1)}{1+f_v(K_i-1)} = 0 \tag{B.3}$$

B.1 Successive Substitution Iteration

(a) Solve vapor mole fraction f_v from Equation (B.3);

(b) Update x_i, y_i based on Equation (B.4) and (B.5);

$$x_i = \frac{z_i}{1+f_v(K_i-1)}, (i = 1, \dots, n_h) \tag{B.4}$$

$$y_i = \frac{K_i z_i}{1+f_v(K_i-1)}, (i = 1, \dots, n_h) \tag{B.5}$$

(c) Calculate fugacities $\hat{f}_i^l, \hat{f}_i^v$ of liquid and vapor phase based on PR-EOS;

(e) Check convergence through the equal-fugacity constraint (Equation (B.6));

$$\sum_{i=1}^{n_h}\left(\frac{\hat{f}_i^l}{\hat{f}_i^v}-1\right)^2 < \varepsilon \tag{B.6}$$

(d) If convergence is not reached in step (e), update K_i with the fugacity ratios, showing as Equation (B.7), and repeat step (a) to (d).

$$K_i^{n+1} = K_i^n \frac{\left(\hat{f}_i^l\right)^n}{\left(\hat{f}_i^v\right)^n} \tag{B.7}$$

The convergence of SSI is guaranteed but its convergence speed is slow. On the other hand, NR converges quickly, and its convergence relies initial guess with good quality. Therefore, SSI can be used to provide initial guess for NR. Specifically if the iteration of SSI is greater than a maximum iteration to switch to NR, or if the error in Equation (B.6) is smaller than a tolerance to switch to NR, SSI loop is terminated and provides initial guesses for NR loop.

B.2 Newton-Raphson Iteration

(a) Based on initial values of f_v, lnK_i, z_i, calculate phase compositions; x_i, y_i based on Equations (B.4) and (B.5), and then through PR-EOS calculate fugacity coefficients and their derivatives to phase compositions $\{ln\varphi_i^l, ln\varphi_i^v, \frac{\partial ln\varphi_i^l}{\partial lnx_j}, \frac{\partial ln\varphi_i^v}{\partial lny_j}\}$;

(b) Construct primary variables and residual vectors, shown as Equations (B.8) and (B.9), and the length of both vectors are $n_h + 1$;

$$\vec{X} = \left[lnK_1, lnK_2, lnK_3, \cdots, lnK_{n_h}, f_v \right]^T_{n_h+1} \tag{B.8}$$

$$\vec{R} = \left[R_{f,1}, R_{f,2}, R_{f,3}, \cdots, R_{f,n_h}, R_r \right]^T_{n_h+1} \tag{B.9}$$

(d) Calculate the error of VLE by the L-2 norm of $\vec{R}$, and check the convergence based on Equation (B.10);

$$Error = \left\| \vec{R} \right\|_2 < \varepsilon \tag{B.10}$$

(e) If convergence is reached in step (d), NR-loop is stopped; otherwise, based on chain rule, construct the analytical Jacobian of VLE, shown as Equation (B.10);

$$J = \frac{\partial \vec{R}}{\partial \vec{X}} = \begin{bmatrix} \frac{\partial R_{f,1}}{\partial lnK_1} & \frac{\partial R_{f,1}}{\partial lnK_2} & \cdots & \frac{\partial R_{f,1}}{\partial lnK_{n_h}} & \frac{\partial R_{f,1}}{\partial f_v} \\ \frac{\partial R_{f,1}}{\partial lnK_1} & \frac{\partial R_{f,2}}{\partial lnK_2} & \cdots & \frac{\partial R_{f,2}}{\partial lnK_{n_h}} & \frac{\partial R_{f,2}}{\partial f_v} \\ \cdots & \cdots & \cdots & \cdots & \cdots \\ \frac{\partial R_{f,n_h}}{\partial lnK_1} & \frac{\partial R_{f,n_h}}{\partial lnK_2} & \cdots & \frac{\partial R_{f,n_h}}{\partial lnK_{n_h}} & \frac{\partial R_{f,n_h}}{\partial f_v} \\ \frac{\partial R_r}{\partial lnK_1} & \frac{\partial R_r}{\partial lnK_2} & \cdots & \frac{\partial R_r}{\partial lnK_{n_h}} & \frac{\partial R_r}{\partial f_v} \end{bmatrix}_{(n_h+1)\times(n_h+1)} \tag{B.11}$$

(f) Update $\vec{X}$ through Equation (B.12). Since the dimension of the linear system is relatively low, here Gaussian Elimination with pivoting method is used to solve $AX = b$.

$$\vec{X}^{n+1} = \vec{X}^n - J^{-1}\vec{R} \tag{B.12}$$

(g) Repeat step (a) to (f).

The derivatives in Equation (B.11) are further discussed. Firstly, the derivatives of Equations (B.2) and (B.3) to lnK_j can be represented by Equation (B.13) and (B.14),

$$\frac{\partial R_{f,i}}{\partial lnK_j} = \delta_{ij} + \frac{\partial ln\varphi_i^v}{\partial y_j} \cdot \frac{\partial y_j}{\partial lnK_j} - \frac{\partial ln\varphi_i^l}{\partial x_j} \cdot \frac{\partial x_j}{\partial lnK_j} \tag{B.13}$$

$$\frac{\partial R_r}{\partial lnK_j} = \frac{K_j z_j}{\left[1+f_v(K_j-1)\right]^2} \tag{B.14}$$

where,

$$\delta_{ij} = \begin{cases} 1 & (i = j) \\ 0 & (i \neq j) \end{cases} \tag{B.15}$$

Based on Equations (B.4) and (B.5), sub terms in Equation (B.13) can be calculated,

$$\frac{\partial x_j}{\partial lnK_j} = \frac{\partial}{\partial lnK_j}\left\{\frac{z_j}{1+f_v(K_j-1)}\right\} = -\frac{z_j K_j f_v}{\left[1+f_v(K_j-1)\right]^2} \tag{B.16}$$

$$\frac{\partial y_j}{\partial lnK_j} = \frac{\partial}{\partial lnK_j}\left\{\frac{z_j K_j}{1+f_v(K_j-1)}\right\} = \frac{z_j K_j (1-f_v)}{\left[1+f_v(K_j-1)\right]^2} \tag{B.17}$$

On the other hand, the derivatives of Equations (B.2) and (B.3) with regards to f_v can be represented by,

$$\frac{\partial R_{f,i}}{\partial f_v} = \frac{\partial ln\varphi_i^v}{\partial f_v} - \frac{\partial ln\varphi_i^l}{\partial f_v} \tag{B.18}$$

$$\frac{\partial R_r}{\partial f_v} = -\sum_{i=1}^{n_h} \frac{z_i (K_i-1)^2}{[1+f_v(K_i-1)]^2} \tag{B.19}$$

where,

$$\frac{\partial ln\varphi_i^l}{\partial f_v} = \sum_{j=1}^{n_h} \frac{\partial ln\varphi_i^l}{\partial x_j} \cdot \frac{\partial x_j}{\partial f_v} \tag{B.20}$$

$$\frac{\partial ln\varphi_i^v}{\partial f_v} = \sum_{j=1}^{n_h} \frac{\partial ln\varphi_i^v}{\partial y_j} \cdot \frac{\partial y_j}{\partial f_v} \tag{B.21}$$

$$\frac{\partial x_j}{\partial f_v} = -\frac{z_j(K_j-1)}{\left[1+f_v(K_j-1)\right]^2} \tag{B.22}$$

$$\frac{\partial y_j}{\partial f_v} = -\frac{K_j z_j(K_j-1)}{\left[1+f_v(K_j-1)\right]^2} \tag{B.23}$$